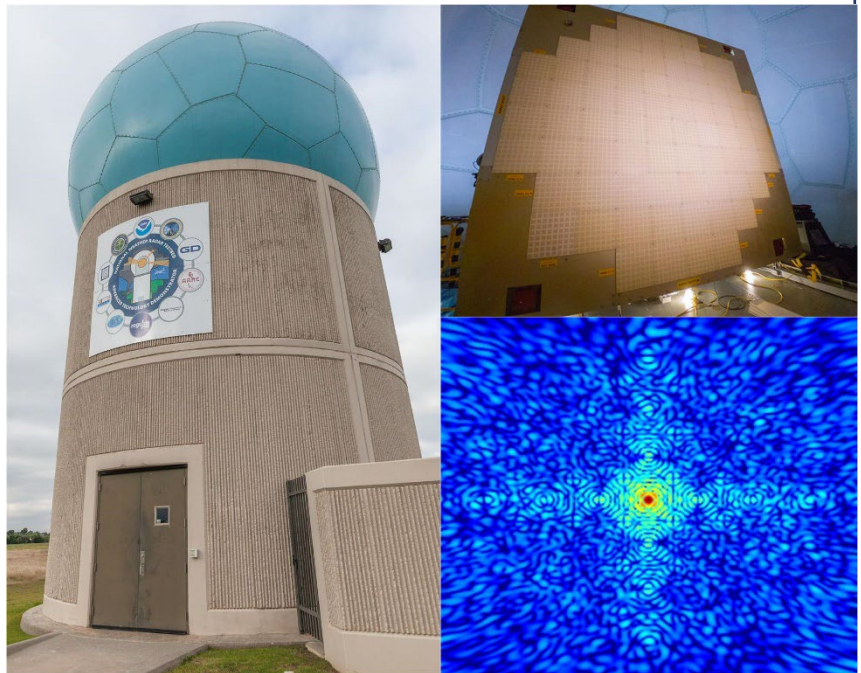# An Update on Polarimetric Calibration for the Advanced Technology Demonstrator

**National Severe Storms Laboratory Report**

*prepared by:* **Igor Ivić, Nai Feng, and Sebastian Torres**

**September 2023**

# Executive summary

Phased array radar (PAR) technology is being considered as one of the candidates for the next generation of weather-surveillance radars in the US. The unique capabilities offered by this technology can potentially increase the quality and timeliness of weather radar products, ultimately improving severe-weather warnings and forecasts. One of the major technical challenges related to the use of PAR technology for weather observations is the integration of dual-polarization technology, which is currently available on the NEXRAD network. In other words, adopting PAR technology for weather observations is contingent to demonstrating that a polarimetric PAR can produce radar data that meet National Weather Service (NWS) mission needs.

Located in Norman, Oklahoma, the Advanced Technology Demonstrator (ATD) is the first full-scale, S-band, dual-polarization, active, electronically scanned PAR for weather observations. The ATD leverages several prior investments to provide a flexible radar system with which to demonstrate some of PAR's unique capabilities. One of the main goals for the ATD is to help answer important questions about the dual-polarization performance of planar phased-array radars, to demonstrate that a polarimetric PAR can be calibrated, and that calibration can be maintained over time to consistently produce good-quality radar data. At a fundamental level, the polarimetric calibration of a weather radar (PAR or otherwise) consists of characterizing hardware and antenna-radiation-pattern imperfections and accounting for them in the processing of the radar signals. For PARs, the radiation patterns change as the beam is steered electronically; hence, the polarimetric calibration requires accurate and robust characterization of all radar beams at electronic steering angles of interest, which could be on the order of thousands.

The polarimetric calibration of the ATD has been a top research priority for the past several years. In the design phase, it was decided that the antenna would be mounted on an elevation pedestal and azimuth turntable, and that a calibration tower would be installed in the line of sight of the radar so that beam patterns could be fully characterized. Our preliminary report on the polarimetric calibration of the ATD (published in November 2020) documented our initial efforts to develop, implement, and test processes for (1) the absolute radar-cross-section (RCS) calibration, (2) the broadside polarimetric calibration, and (3) the beamsteering polarimetric calibration. Additionally, it presented a preliminary end-to-end evaluation of polarimetric calibration performance using a limited number of radar data sets. At that time, two main challenges were identified for the polarimetric calibration of the ATD. One challenge was related to system temperature drifts due to insufficient performance of the thermal-management approach initially used by

the ATD antenna. System temperature drifts changed the performance of analog components in the antenna and ultimately compromised the repeatability and accuracy of some calibration measurements. After recognizing how critical this was to the polarimetric calibration of the ATD, this led to significant engineering efforts to implement the improved thermal-management approach that the ATD facility uses today. Other aspects adversely impacting the repeatability and accuracy of polarimetric calibration measurements involved multipath interference and unexpected hardware imperfections, which caused effects that ranged from temporary glitches to complete failures of one or more subsystems in the measurement path. Fortunately, once understood, these effects were effectively mitigated with a combination of proactive hardware maintenance and additional processing of the measured calibration data. Remaining fundamental questions at the time of our initial report related to our understanding and improvement of the stability and robustness of the different polarimetric calibration processes. In this context, stability relates to how the measurements change over time, which is critical to inform the frequency of execution for the different polarimetric calibration processes. Robustness is related to the repeatability of the results over short timescales, which can be understood as a proxy for the precision of the measurements. Over time, our continuous analysis of stability and robustness led to important modifications of the initial calibration procedures.

This report documents our progress since the writing of the preliminary report. The accomplishments presented here are the result of extensive and continuous testing, analysis, and refinement of calibration processes that encompass how the measurements are collected, processed, and used in the signal processor to produce weather radar data. Important outcomes of this work include significant improvements to the robustness of the measurements, a deeper understanding on the stability of the measurements, and a more accurate use of the measurements in the signal processor to ultimate produce polarimetric radar data with good quality.

Related to this effort, and with the goal of keeping the polarimetric calibration process as simple as possible, we also continued exploring the use of pulse-to-pulse phase coding to reduce cross-coupling contamination. As part of this effort, we developed a more effective code sequence and a greater understanding for the impacts of pulse-to-pulse phase coding on the signal processor's ability to produce good-quality data (e.g., by mitigating ground clutter contamination), which emphasized the importance of developing system requirements that directly address the performance of pulse-to-pulse phase coding.

One of the most significant accomplishments reported in this document is the reformulation of the mathematical framework to fully account for the geometry and imperfections of the measuring system. An accurate mathematical framework is crucial for developing effective calibration processes; it provides insight on what parameters should be measured and a way to properly interpret (and thus use) these measurements. For completeness, this report documents the derivation of this mathematical framework in detail. Given that the initial beam characterization results did not match our expectations, a major takeaway related to this effort is that, by applying the revised mathematical framework, our measurement results became consistent with our expectations for the polarimetric performance of a planar phased-array antenna. This mathematical framework also helps understand how the calibration process may be simplified (this is referred to as "partial correction") when cross-coupling biases are effectively mitigated by using pulse-to-pulse phase coding, as it is the case with the ATD.

The summary of signal processing steps to produce polarimetric data in the initial report is repeated here for convenience. This helps highlight the polarimetric calibration products that are routinely produced, archived, and used in real time by the signal processor (i.e., range calibration, absolute RCS calibration, beamsteering and cross-coupling bias calibration, and broadside calibration products). As another fundamental contribution, the latest version of the techniques used to measure polarimetric calibration parameters are described. These are the result of numerous revisions over the last 3 years, which were mainly aimed at improving the accuracy and robustness of the measurements, but also, and especially in the case of the beamsteering calibration products, to reduce the execution time without sacrificing performance.

Through the collection and analysis of multiple measurement sets, we now have a solid understanding of the stability of the different polarimetric-calibration measurements and have significantly improved the robustness of the measurement processes. In recent tests, the absolute RCS calibration and the beamsteering polarimetric calibration processes were shown to be very stable and repeatable. The broadside polarimetric calibration process was shown to be repeatable but less stable (i.e., it requires more frequent measurements to accurately track any system changes, likely due to minor temperature drifts). This is not a significant hurdle since the broadside polarimetric calibration currently takes just about 2 minutes to collect and process the data.

Recent tests using improved calibration processes have resulted in polarimetric data with high quality; this was confirmed by engineering analyses and routine expert meteorologist data-quality assessments. The

qualitative assessment involved comparisons of ATD data to conceptual models and with data collected by other radars in the vicinity of the ATD. The quantitative assessment entailed detailed analyses of data obtained from self-consistency tests. Comparison of uncalibrated and calibrated dual-polarimetric data fields obtained with the ATD strongly confirmed the need for polarimetric calibration and also qualitatively illustrated the satisfactory performance of the implemented calibration processes.

Overall, our work has been critical in demonstrating that a planar phased-array antenna can be calibrated to produce polarimetric data with good quality and that the calibration can be maintained over time. Moving forward, we will continue to work on improving and upgrading the existing calibration processes to support more advanced scanning modes (e.g., the use of spoiled transmit beams to reduce scan times) and on monitoring the accuracy and stability of calibration results We will also continue using self-consistency tests to periodically evaluate the performance of beamsteering bias corrections, particularly at mid to high elevations, which were not the focus of previous analyses. Future work in polarimetric PAR calibration will involve developing more precise measurement procedures. One potential approach is to utilize Bragg scattering to determine the absolute accuracies of differential reflectivity measurements. This approach could help establish a more comprehensive and precise measurement of the biases, enhancing the overall accuracy of weather observations obtained from the ATD. The collaborative research with the Advance Radar Research Center (ARRC) on using Unmanned Aerial Systems (UAS) to conduct polarimetric calibrations is also expected to continue, as well as the development of alternative polarimetric calibration approaches that may be more suitable for a potential future operational implementation.

# 1. Introduction

Polarimetric phased array radar (PPAR) technology is being considered as a potential candidate for the next generation of weather radars in the United States (Zrnić et al. 2007, Weber 2019). One of the primary technical challenges associated with the use of PPAR technology for weather surveillance is the requirement to produce polarimetric data with acceptable quality (Zrnić et al. 2012).

In major contrast to reflector (dish) antennas, the horizontal (H) and vertical (V) copolar antenna radiation patterns (i.e., the two-way antenna radiation pattern for the same polarization on transmit and receive) of a PPAR antenna change as the beam is electronically steered. This leads to so-called "copolar biases" (or beamsteering biases when measured relative to broadside) in radar estimates of reflectivity, differential reflectivity, differential phase, and correlation coefficient. In addition, PPAR antennas typically have more significant cross-polar antenna patterns (i.e., the two-way antenna radiation pattern for different polarization on transmit and receive). These introduce cross coupling between signals from the horizontally and vertically oriented electromagnetic fields, and ultimately lead to so-called "cross-polar biases" in reflectivity and all polarimetric-variable estimates. Whereas cross-polar biases may be mitigated using a combination of transmission and signal-processing techniques referred to as "pulse-to-pulse phase coding" (Zrnić et al. 2014, Ivić 2017, Ivić 2017a, Ivić 2018a), copolar bias mitigation requires an accurate characterization of the copolar antenna patterns (Ivić, 2018b) at each electronic beamsteering location of interest (Ivić and Schvartzman 2019, Ivić and Schvartzman 2020). Also, if the cross-polar biases cannot be effectively mitigated using the pulse-to-pulse phase coding technique, a correction that considers both the copolar and cross-polar patterns becomes necessary (Ivić 2018). Additionally, the impact of active electronic components in the transmit and receive paths of PAR systems can introduce significant mismatches between the transmit and receive patterns. Therefore, for effective polarimetric calibration of PPARs, it is crucial to accurately characterize the one-way copolar and cross-polar antenna patterns (i.e., the transmit and the receive antenna radiation patterns) (Ivić 2019).

This follow-on report summarizes the evolution of our measurement techniques and of our understanding of the performance and limitations of the polarimetric calibration on the Advanced Technology Demonstrator (ATD, https://www.nssl.noaa.gov/tools/radar/atd/). While some introductory material is repeated, the focus is on progress made since the writing of the first report (https://tinyurl.com/ATD-Cal-Report-1). Compared to the initial report, this update incorporates more comprehensive explanations of the

mathematical framework underpinning the polarimetric calibration and offers a more rigorous quantitative assessment of the calibration performance.

The report is organized as follows. First, we provide an updated in-depth analysis of the effects of PPAR antenna patterns on weather-radar measurements which provide the motivation for PPAR polarimetric calibration and a solid theoretical foundation for corrections that account for these effects. We continue by presenting an update of the polarimetric calibration procedures developed for the ATD and their application on weather data. We end the report with an outlook and summary of proposed future work.

## 2. An analysis of the PPAR antenna patterns effects on weather-radar measurements

To examine the impact of PPAR patterns on weather-radar measurements, we employ a theoretical model that decomposes the radar-scanned space into elemental sub-volumes ($d\Omega$) (Ivić and Doviak 2016). Within this model, the received signals in the horizontal (H) and vertical (V) polarizations are the sums of differential voltages generated by the returns from each sub-volume that contains numerous scatterers. The statistical characteristics of the scatterers within each sub-volume are described using spectral moments and polarimetric variables (Doviak and Zrnić 1993). Additionally, we assume that the hydrometeors present in the system are oblate spheroids with a negligible mean canting angle (Oguchi 1983). However, it is important to note that this assumption may not always hold true (Ryzhkov and Zrnić 2007, Illingworth and Thompson 2011), although it accurately represents the properties of most hydrometeors encountered in observations, such as rain. Furthermore, the following assumptions are made: 1) the amplitudes and phases of the transmitted H and V copolar radiations are not matched, and 2) for most observations at approximately 10-cm wavelengths, the differential attenuation along the propagation path can be disregarded, while the differential phase ($\phi_{DP}$) cannot (Doviak and Zrnić 1993).

The standard model that describes the time series received in the H and V channels from the $m$-th transmission in the Simultaneous-Transmission-Simultaneous-Receive (STSR or SHV) mode and at each beamsteering angle at azimuth, $az_B = \phi_0$, and elevation, $el_B = \theta_0 - 90°$, is

$$\begin{bmatrix} V_h(az_B, el_B, m) \\ V_v(az_B, el_B, m) \end{bmatrix} = C \int_{\Omega} \mathbf{R_{ATD}} \times \mathbf{S} \times \mathbf{T_{ATD}} \times \mathbf{E_{ATD}} d\Omega,$$

$$= C \int_{\Omega} \left\{ \begin{array}{l} \begin{bmatrix} R_h^{co}(az_B, el_B, \phi, \theta) & R_h^{x}(az_B, el_B, \phi, \theta) \\ R_v^{x}(az_B, el_B, \phi, \theta) & R_v^{co}(az_B, el_B, \phi, \theta) \end{bmatrix} \times \\ \begin{bmatrix} s_{hh}(az_B, el_B, \phi, \theta, m) & 0 \\ 0 & s_{vv}(az_B, el_B, \phi, \theta, m) \end{bmatrix} \times \\ \begin{bmatrix} T_h^{co}(az_B, el_B, \phi, \theta) & T_v^{x}(az_B, el_B, \phi, \theta) \\ T_h^{x}(az_B, el_B, \phi, \theta) & T_v^{co}(az_B, el_B, \phi, \theta) \end{bmatrix} \times \begin{bmatrix} e^{j\alpha_h(m)} \\ e^{j\alpha_v(m)} \end{bmatrix} \end{array} \right\} d\Omega,$$

$$= C \int_{\Omega} \left[ \begin{array}{l} \left\{ \begin{array}{l} \left[ T_h^{co}(az_B, el_B, \phi, \theta)e^{j\alpha_h(m)} + T_v^{x}(az_B, el_B, \phi, \theta)e^{j\alpha_v(m)} \right] \times \\ R_h^{co}(az_B, el_B, \phi, \theta)s_{hh}(az_B, el_B, \phi, \theta, m) + \\ \left[ T_h^{x}(az_B, el_B, \phi, \theta)e^{j\alpha_h(m)} + T_v^{co}(az_B, el_B, \phi, \theta)e^{j\alpha_v(m)} \right] \times \\ R_h^{x}(az_B, el_B, \phi, \theta)s_{vv}(az_B, el_B, \phi, \theta, m) \end{array} \right\} \\ \left\{ \begin{array}{l} \left[ T_h^{co}(az_B, el_B, \phi, \theta)e^{j\alpha_h(m)} + T_v^{x}(az_B, el_B, \phi, \theta)e^{j\alpha_v(m)} \right] \times \\ R_v^{x}(az_B, el_B, \phi, \theta)s_{hh}(az_B, el_B, \phi, \theta, m) + \\ \left[ T_h^{x}(az_B, el_B, \phi, \theta)e^{j\alpha_h(m)} + T_v^{co}(az_B, el_B, \phi, \theta)e^{j\alpha_v(m)} \right] \times \\ R_v^{co}(az_B, el_B, \phi, \theta)s_{vv}(az_B, el_B, \phi, \theta, m) \end{array} \right\} \end{array} \right] d\Omega$$

(2.1)

where $d\Omega \equiv \sin(\theta)d\theta d\phi$ (integration along range is omitted as it has no bearing on the results) and the integral is across the entire radar field of view in the $\phi\theta$ spherical coordinate system (Figure 2.1). Note that for simplicity, the expressions in (2.1) do not account for the effects of noise in the H and V channels. Further, the dependency on ($az_B$, $el_B$) and ($\phi,\theta$) is dropped in subsequent discussions for brevity. This yields the following expression

$$\begin{bmatrix} V_h(m) \\ V_v(m) \end{bmatrix} = C \int_{\Omega} \begin{bmatrix} \left[ T_h^{co}e^{j\alpha_h(m)} + T_v^{x}e^{j\alpha_v(m)} \right] R_h^{co}s_{hh}(m) + \left[ T_h^{x}e^{j\alpha_h(m)} + T_v^{co}e^{j\alpha_v(m)} \right] R_h^{x}s_{vv}(m) \\ \left[ T_h^{co}e^{j\alpha_h(m)} + T_v^{x}e^{j\alpha_v(m)} \right] R_v^{x}s_{hh}(m) + \left[ T_h^{x}e^{j\alpha_h(m)} + T_v^{co}e^{j\alpha_v(m)} \right] R_v^{co}s_{vv}(m) \end{bmatrix} d\Omega$$
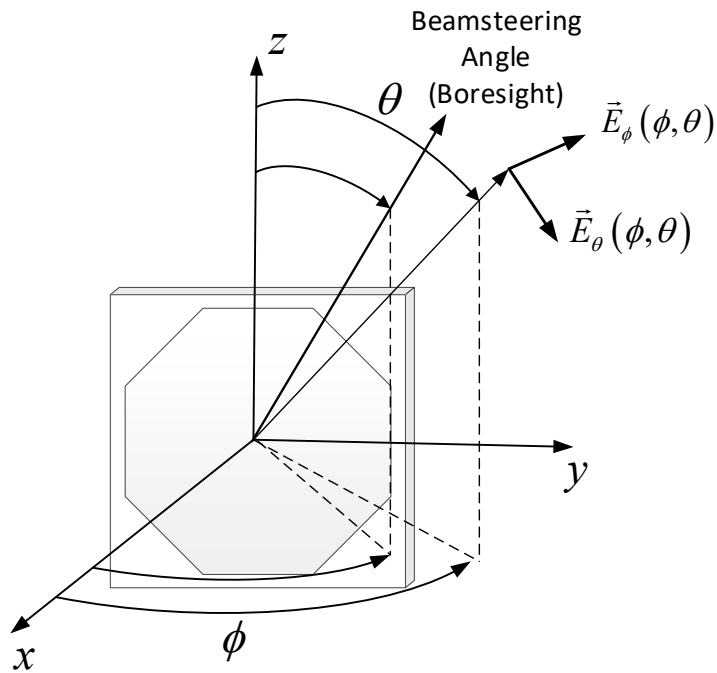
(2.2)

that is easier to interpret.

*Figure 2.1. Depiction of coordinate systems within which the PPAR operates.*

In (2.1), $\mathbf{E_{ATD}}$ is the excitation vector where $\alpha_h(m)$ and $\alpha_v(m)$ denote the phase shifts imposed on transmission in the H and V channels to implement the pulse-to-pulse phase coding (Zrnić et al. 2014, Ivić and Doviak 2016, Ivić 2018, Ivić 2018a, Ivić 2022). The matrices $\mathbf{T_{ATD}}$ and $\mathbf{R_{ATD}}$ describe the transmit and receive ATD antenna patterns in the spherical system tied to the antenna plane (e.g., $\phi\theta$ bound to the *xyz* Cartesian coordinate system in Figure 2.1). Their elements are denoted by symbols $F_p^c$ (where $F$ can be either '*T*' or '*R*', $p$ is either 'h' or 'v', and $c$ is either 'co' or 'x' which stand for copolar and cross-polar, respectively) and describe the one-way electric field patterns that are complex functions of $\phi$ and $\theta$ and are different at each boresight direction ($\theta_0$, $\phi_0$). Hence, $T_h^{co}$ and $R_h^{co}$ denote the copolar H patterns on transmit and receive, respectively (i.e., fields concomitant with $\vec{E}_\phi$ in Figure 2.1). By the same rationale, $T_h^x$ and $R_h^x$ are the cross-polar H patterns (i.e., fields concomitant with $\vec{E}_\theta$ in Figure 2.1). Analogously, $T_v^{co}$, $R_v^{co}$, $T_v^x$, and $R_v^x$ denote the co- and cross-polar V patterns. An example of the transmit and receive patterns for the ATD antenna at $az_B = -45°$, $el_B = 10°$ is given in Figure 2.2 and Figure 2.3 (measured in an anechoic chamber at MIT Lincoln Laboratory during initial antenna testing). These show that the patterns exhibit highest levels at and around boresight, as expected.
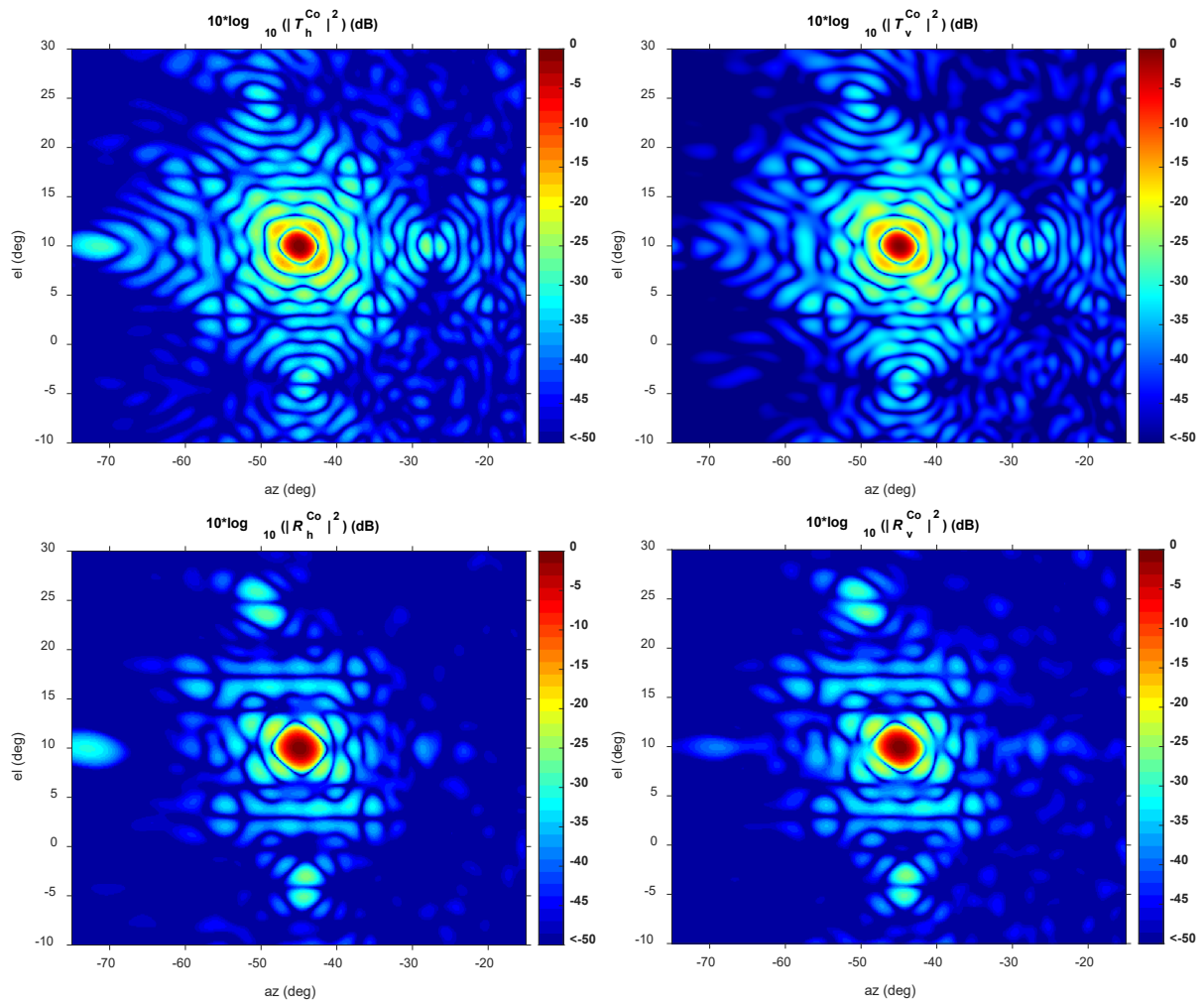
*Figure 2.2. The transmit (top panels) and receive (bottom panels) in H (left column) and V (right column) copolar ATD antenna patterns for $el_B = 10°$ and $az_B = -45°$.*
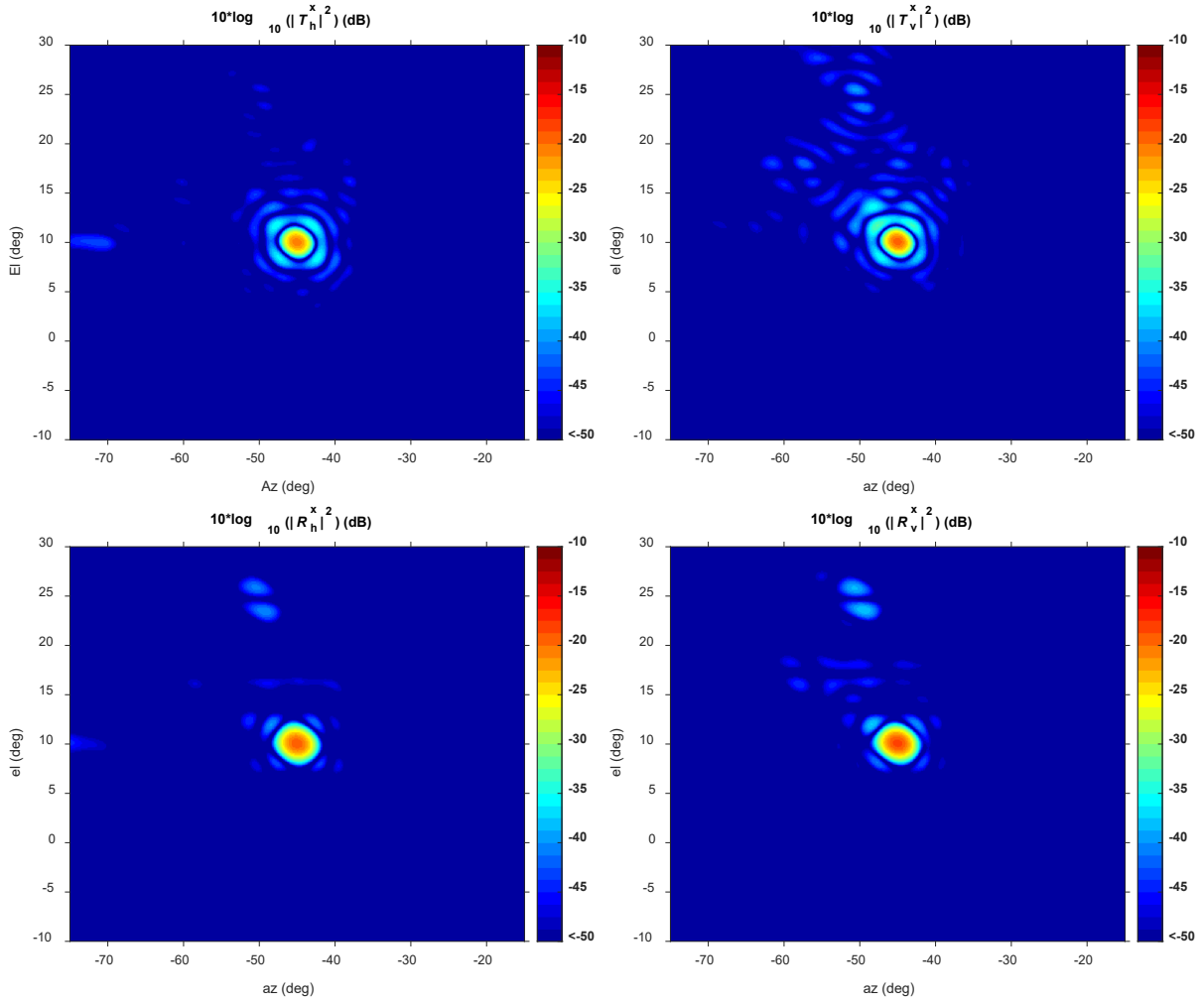
*Figure 2.3. The transmit (top panels) and receive (bottom panels) in H (left column) and V (right column) cross-polar ATD antenna patterns for $el_B = 10°$ and $az_B = -45°$.*

The symbol **S** denotes the backscattering matrix and has zeroes on the off-diagonal due to the assumption of negligible mean canting angle of the observed scatterers. The elements of **S** are sub-volume backscattering coefficients (Ivić and Doviak 2016), $s_{hh}(m)$ and $s_{vv}(m)$, which denote the scaled intrinsic echo voltages from every sub-volume, that would be received in H and V channels, respectively, if $F_p^{co} = 1$ and $F_p^{x} = 0$. Further, the propagation induced difference in phase between H and V (i.e., differential phase or $\phi_{DP}$) is absorbed into the backscattering coefficient for the horizontal polarization so $\langle arg\{s_{hh}^*(m)s_{vv}(m)\}\rangle = \phi_{DP}$ (where $\langle \ \rangle$ denotes mathematical expectation). The properties of the sub-volume backscattering coefficients are described by the Doppler moments (i.e., $S_h$ and $S_v$ that are powers in H and V channels, velocity $v$, and spectrum width $\sigma_v$) and the polarimetric variables (i.e., differential

12

reflectivity $Z_{DR}$, copolar correlation coefficient $|\rho_{hv}|$, and differential phase $\phi_{DP}$) (Doviak and Zrnić 1993).
In terms of $s_{hh}(m)$ and $s_{vv}(m)$, measurables $v$, $\sigma_v$, $Z_{DR}$, $|\rho_{hv}|$, and $\phi_{DP}$ are

$$v = -\frac{v_a}{\pi} arg\{\langle \hat{R}_h(1) \rangle\} = -\frac{v_a}{\pi} arg\{\langle \hat{R}_v(1) \rangle\}$$

$$\sigma_v = \frac{v_a}{\pi\sqrt{2}} \frac{|\langle \hat{R}_h(1) \rangle|}{\langle \hat{S}_h \rangle} = \frac{v_a}{\pi\sqrt{2}} \frac{|\langle \hat{R}_v(1) \rangle|}{\langle \hat{S}_v \rangle}$$

$$Z_{DR} = 10\, log_{10}\left(\frac{\langle \hat{S}_h \rangle}{\langle \hat{S}_v \rangle}\right)$$

$$|\rho_{hv}| = \frac{|\langle \hat{R}_{hv}(0) \rangle|}{\sqrt{\langle \hat{S}_h \rangle \langle \hat{S}_v \rangle}}$$

$$\phi_{DP} = arg\{\langle \hat{R}_{hv}(0) \rangle\} \tag{2.3}$$

where

$$\hat{S}_h = \frac{C^2}{M} \sum_{m=0}^{M-1} \left|\int_\Omega s_{hh}(m)d\Omega\right|^2,$$

$$\hat{S}_v = \frac{C^2}{M} \sum_{m=0}^{M-1} \left|\int_\Omega s_{vv}(m)d\Omega\right|^2,$$

$$\hat{R}_h(1) = \frac{C^2}{M-1} \sum_{m=0}^{M-2} \int_\Omega s_{hh}^*(m)s_{hh}(m+1)d\Omega,$$

$$\hat{R}_v(1) = \frac{C^2}{M-1} \sum_{m=0}^{M-2} \int_\Omega s_{vv}^*(m)s_{vv}(m+1)d\Omega,$$

$$\hat{R}_{hv}(0) = \frac{C^2}{M} \sum_{m=0}^{M-1} \int_\Omega s_{hh}^*(m)s_{vv}(m)d\Omega, \tag{2.4}$$

are second-order estimates, and the integrals are across main beams to encompass the areas at and around boresight. Finally, $C$ is a scalar factor that contains the dependence on range and system parameters on transmit and receive. Expression (2.3) and (2.4) indicate that the radar measurables are functions of $s_{hh}(m)$ and $s_{vv}(m)$, but the bottom formulas in (2.1) show that the signals PPAR receives are also functions of copolar and cross-polar patterns. For this reason, we need to understand the effects of the transmit and receive antenna patterns on the weather measurements; we do this next.

To analyze the transmit pattern effects, we assume no cross coupling on receive by setting $R_h^x$ and $R_v^x$ to zero. This yields

$$\begin{bmatrix} V_h(az_B, el_B, m) \\ V_v(az_B, el_B, m) \end{bmatrix} = C \int_\Omega \begin{bmatrix} s_{hh}(m)\left(T_h^{co} e^{j\alpha_h(m)} + T_v^x e^{j\alpha_v(m)}\right)R_h^{co} \\ s_{vv}(m)\left(T_h^x e^{j\alpha_h(m)} + T_v^{co} e^{j\alpha_v(m)}\right)R_v^{co} \end{bmatrix} d\Omega. \qquad (2.5)$$

The expression (2.5) suggests that if no cross-polar patterns are present on receive, the received signals in H and V reflect the weather signal properties of interest weighted by the copolar and cross-polar transmit patterns as well as the copolar receive patterns. Hence, the transmit patterns do not introduce any cross coupling, where the cross coupling in the H (V) channel is defined as contamination by signals weighted by $s_{vv}$ ($s_{hh}$). Also, because cross-polar patterns exhibit considerably lower levels than copolar ones, their effects are comparatively smaller. Examination of the full expression in (2.1), however, shows that the received signals in the H and V channels are a combination of $s_{hh}(m)$ and $s_{vv}(m)$ weighted by the co- and cross-polar transmit and receive patterns. Thus, the receive cross-polar patterns are the cause of the cross coupling in polarimetric weather radars.

During the ATD calibration procedure, we do not measure the full antenna patterns but rather perform discrete measurements of the main beams, which affect weather signal measurements the most. Thus, the goal of the procedure to measure transmit and receive antenna pattern is to capture amplitude and phase information on the horizontal and vertical transmit and receive copolar main lobe beams as well as the corresponding cross-polar patterns at and around the boresight direction for each beamsteering angle that needs calibration. For this, we use the discretized approximate model derived from (2.1) as

$$\begin{bmatrix} V_h(el_B, az_B, m) \\ V_v(el_B, az_B, m) \end{bmatrix} \approx C \sum_{\theta_n} \sum_{\phi_n} \left\{ \begin{bmatrix} R_h^{co}(\phi_n.\theta_n) & R_h^x(\phi_n.\theta_n) \\ R_v^x(\phi_n.\theta_n) & R_v^{co}(\phi_n.\theta_n) \end{bmatrix} \begin{bmatrix} s_{hh}(\phi_n.\theta_n, m) & 0 \\ 0 & s_{vv}(\phi_n.\theta_n, m) \end{bmatrix} \times \begin{bmatrix} T_h^{co}(\phi_n.\theta_n) & T_v^x(\phi_n.\theta_n) \\ T_h^x(\phi_n.\theta_n) & T_v^{co}(\phi_n.\theta_n) \end{bmatrix} \begin{bmatrix} e^{j\alpha_h(m)} \\ e^{j\alpha_v(m)} \end{bmatrix} \Omega_n \right\}, (2.6)$$

where $\Omega_n = \sin(\theta_n)\Delta\theta\Delta\phi$. In (2.6), $\Delta\theta$ and $\Delta\phi$ determine the measurement resolution in elevation and azimuth and

$$\theta_n = 90° - el_B + n \times \Delta\theta,$$
$$\phi_n = az_B + n \times \Delta\phi, \qquad\qquad\qquad (2.7)$$

where the range of $n$ determines the extent (or portion) of the of the pattern that is measured. For the ATD beam measurements, $\Delta\theta = \Delta\phi = 0.1°$ and $n = $ -10, -9, …, 9, 10.

Recall that second-order quantities are computed from the received radar signals $V_h$ and $V_v$ as

$$\hat{S}_h(el_B, az_B) = \frac{1}{M} \sum_{m=0}^{M-1} |V_h(el_B, az_B, m)|^2,$$

$$\hat{S}_v(el_B, az_B) = \frac{1}{M} \sum_{m=0}^{M-1} |V_v(el_B, az_B, m)|^2$$

$$\hat{R}_h(el_B, az_B, 1) = \frac{1}{M} \sum_{m=0}^{M-1} V_h^*(el_B, az_B, m) V_h(el_B, az_B, m+1) e^{j[\alpha_h(m)-\alpha_h(m+1)]}$$

$$\hat{R}_v(el_B, az_B, 1) = \frac{1}{M} \sum_{m=0}^{M-1} V_v^*(el_B, az_B, m) V_v(el_B, az_B, m+1) e^{j[\alpha_v(m)-\alpha_v(m+1)]}$$

$$\hat{R}_{hv}(el_B, az_B, 0) = \frac{1}{M} \sum_{m=0}^{M-1} V_h^*(el_B, az_B, m) V_v(el_B, az_B, m) e^{j[\alpha_h(m)-\alpha_v(m)]} \qquad (2.8)$$

The fact that $v$ and $\sigma_v$ may be computed from second-order estimates derived from either $s_{hh}(m)$ or $s_{vv}(m)$ indicates that the cross-coupling has no significant adverse effect on these products. Also, because $v$ is computed from the phase difference between radar signals from the same channel on two subsequent transmissions, this measurement is unaffected by the copolar biases. In the case of $\sigma_v$, it is computed from the ratio of autocorrelation magnitude and signal power from the same channel so it is also unaffected by the copolar biases. Thus, using the fact that

$$\langle s_c^*(\phi_n, \theta_n, m) s_p(\phi_{n'}, \theta_{n'}, m) \rangle = \begin{cases} \langle s_c^*(\theta_n, \phi_n, m) s_p(\theta_{n'}, \phi_{n'}, m) \rangle & if \ \phi_n = \phi_{n'}, \theta_n = \theta_{n'} \\ 0 & otherwise \end{cases} \qquad (2.9)$$

where $c$ and $p$ are either 'hh' or 'vv', and substituting in (2.6), we can get an expression that relates the second-order estimates that are affected by cross coupling to $s_{hh}(m)$ and $s_{vv}(m)$ as

$$\begin{bmatrix} \langle \hat{S}_h(az_B, el_B) \rangle \\ \langle \hat{S}_v(az_B, el_B) \rangle \\ \langle \hat{R}_{hv}(az_B, el_B, 0) \rangle \\ \langle \hat{R}_{hv}^*(az_B, el_B, 0) \rangle \end{bmatrix} = C^2 \boldsymbol{TR} \begin{bmatrix} \langle |s_{hh}(\phi_n, \theta_n, m)|^2 \rangle \\ \langle |s_{vv}(\phi_n, \theta_n, m)|^2 \rangle \\ \langle s_{hh}^*(\phi_n, \theta_n, m) s_{vv}(\phi_n, \theta_n, m) \rangle \\ \langle s_{hh}(\phi_n, \theta_n, m) s_{vv}^*(\phi_n, \theta_n, m) \rangle \end{bmatrix}, \qquad (2.10)$$

where $\boldsymbol{TR}$ is 4×4 matrix with elements

$$TR_{11} = \frac{1}{M} \sum_{m=0}^{M-1} \sum_{\theta_n} \sum_{\phi_n} \left[ |T_h^{co} R_h^{co}|^2 + |T_v^x R_h^{co}|^2 + 2 \, Re\{(T_h^{co} R_h^{co})^* T_v^x R_h^{co} e^{j[\alpha_v(m)-\alpha_h(m)]}\} \right] \Delta\Omega_n,$$

15

$$TR_{12} = \frac{1}{M} \sum_{m=0}^{M-1} \sum_{\theta_n} \sum_{\phi_n} \left[ |T_h^x R_h^x|^2 + |T_v^{co} R_h^x|^2 + 2\,Re\left\{ (T_h^x R_h^x)^* T_v^{co} R_h^x e^{j[\alpha_v(m) - \alpha_h(m)]} \right\} \right] \Delta\Omega_n,$$

$$TR_{13} = TR_{14}^* = \frac{1}{M} \sum_{m=0}^{M-1} \sum_{\theta_n} \sum_{\phi_n} \left[ \begin{array}{l} (T_h^{co} R_h^{co})^* T_h^x R_h^x + (T_h^{co} R_h^{co})^* T_v^{co} R_h^x e^{j[\alpha_v(m) - \alpha_h(m)]} + \\ (T_v^x R_h^{co})^* T_h^x R_h^x e^{-j[\alpha_v(m) - \alpha_h(m)]} + (T_v^x R_h^{co})^* T_v^{co} R_h^x \end{array} \right] \Delta\Omega_n,$$

$$TR_{21} = \frac{1}{M} \sum_{m=0}^{M-1} \sum_{\theta_n} \sum_{\phi_n} \left[ |T_v^x R_v^x|^2 + |T_h^{co} R_v^x|^2 + 2\,Re\left\{ (T_v^x R_v^x)^* T_h^{co} R_v^x e^{-j[\alpha_v(m) - \alpha_h(m)]} \right\} \right] \Delta\Omega_n,$$

$$TR_{22} = \frac{1}{M} \sum_{m=0}^{M-1} \sum_{\theta_n} \sum_{\phi_n} \left[ |T_v^{co} R_v^{co}|^2 + |T_h^x R_v^{co}|^2 + 2\,Re\left\{ (T_v^{co} R_v^{co})^* T_h^x R_v^{co} e^{-j[\alpha_v(m) - \alpha_h(m)]} \right\} \right] \Delta\Omega_n,$$

$$TR_{23} = TR_{24}^* = \frac{1}{M} \sum_{m=0}^{M-1} \sum_{\theta_n} \sum_{\phi_n} \left[ \begin{array}{l} (T_v^x R_v^x)^* T_v^{co} R_v^{co} + (T_v^x R_v^x)^* T_h^x R_v^{co} e^{-j[\alpha_v(m) - \alpha_h(m)]} + \\ (T_h^{co} R_v^x)^* T_v^{co} R_v^{co} e^{j[\alpha_v(m) - \alpha_h(m)]} + (T_h^{co} R_v^x)^* T_h^x R_v^{co} \end{array} \right] \Delta\Omega_n,$$

$$TR_{31} = TR_{41}^* = \frac{1}{M} \sum_{m=0}^{M-1} \sum_{\theta_n} \sum_{\phi_n} \left[ \begin{array}{l} (T_h^{co} R_h^{co})^* T_v^x R_v^x + (T_h^{co} R_h^{co})^* T_h^{co} R_v^x e^{j[\alpha_h(m) - \alpha_v(m)]} + \\ (T_v^x R_h^{co})^* T_v^x R_v^x e^{j[\alpha_h(m) - \alpha_v(m)]} + (T_v^x R_h^{co})^* T_h^{co} R_v^x e^{j2[\alpha_h(m) - \alpha_v(m)]} \end{array} \right] \Delta\Omega_n,$$

$$TR_{32} = TR_{42}^* = \frac{1}{M} \sum_{m=0}^{M-1} \sum_{\theta_n} \sum_{\phi_n} \left[ \begin{array}{l} (T_h^x R_h^x)^* T_v^{co} R_v^{co} + (T_h^x R_h^x)^* T_h^x R_v^{co} e^{j[\alpha_h(m) - \alpha_v(m)]} + \\ (T_v^{co} R_h^x)^* T_v^{co} R_v^{co} e^{j[\alpha_h(m) - \alpha_v(m)]} + (T_v^{co} R_h^x)^* T_h^x R_v^{co} e^{j2[\alpha_h(m) - \alpha_v(m)]} \end{array} \right] \Delta\Omega_n.$$

$$TR_{33} = TR_{44}^* = \frac{1}{M} \sum_{m=0}^{M-1} \sum_{\theta_n} \sum_{\phi_n} \left[ \begin{array}{l} (T_h^{co} R_h^{co})^* T_v^{co} R_v^{co} + (T_h^{co} R_h^{co})^* T_h^x R_v^{co} e^{j[\alpha_h(m) - \alpha_v(m)]} + \\ (T_v^x R_h^{co})^* T_v^{co} R_v^{co} e^{j[\alpha_h(m) - \alpha_v(m)]} + (T_v^x R_h^{co})^* T_h^x R_v^{co} e^{j2[\alpha_h(m) - \alpha_v(m)]} \end{array} \right] \Delta\Omega_n,$$

$$TR_{34} = TR_{43}^* =$$

$$\frac{1}{M} \sum_{m=0}^{M-1} \sum_{\theta_n} \sum_{\phi_n} \left[ \begin{array}{l} (T_h^x R_h^x)^* T_v^x R_v^x + (T_h^x R_h^x)^* T_h^{co} R_v^x e^{j[\alpha_h(m) - \alpha_v(m)]} + \\ (T_v^{co} R_h^x)^* T_v^x R_v^x e^{j[\alpha_h(m) - \alpha_v(m)]} + (T_v^{co} R_h^x)^* T_h^{co} R_v^x e^{j2[\alpha_h(m) - \alpha_v(m)]} \end{array} \right] \Delta\Omega_n. \qquad (2.11)$$

Further, assuming that the H and V main beams are filled with scatterers with approximately homogeneous statistical properties so that

$$\langle |s_{hh}(\theta_n, \phi_n, m)|^2 \rangle \approx \langle |s_{hh}(el_B, az_B, m)|^2 \rangle,$$
$$\langle |s_{vv}(\theta_n, \phi_n, m)|^2 \rangle \approx \langle |s_{vv}(el_B, az_B, m)|^2 \rangle,$$
$$\langle s_{hh}^*(\theta_n, \phi_n, m) s_{vv}(\theta_n, \phi_n, m) \rangle \approx \langle s_{hh}^*(el_B, az_B, m) s_{vv}(el_B, az_B, m) \rangle. \qquad (2.12)$$

yields

$$\begin{bmatrix} \langle \hat{S}_h(el_B, az_B) \rangle \\ \langle \hat{S}_v(el_B, az_B) \rangle \\ \langle \hat{R}_{\text{hv}}(el_B, az_B, 0) \rangle \\ \langle \hat{R}^*_{\text{hv}}(el_B, az_B, 0) \rangle \end{bmatrix} \approx C^2 \boldsymbol{TR} \begin{bmatrix} \langle |s_{\text{hh}}(el_B, az_B)|^2 \rangle \\ \langle |s_{\text{vv}}(el_B, az_B)|^2 \rangle \\ \langle s^*_{\text{hh}}(el_B, az_B) s_{\text{vv}}(el_B, az_B) \rangle \\ \langle s_{\text{hh}}(el_B, az_B) s^*_{\text{vv}}(el_B, az_B) \rangle \end{bmatrix}. \tag{2.13}$$

The expression (2.13) suggests that if H and V copolar and cross-polar patterns (i.e., all elements of **TR**) are precisely known at all boresight directions of interest, the corrected second-order estimates of $s_{\text{hh}}(az_B, el_B)$ and $s_{\text{vv}}(az_B, el_B)$ may be obtained as

$$\begin{bmatrix} \tilde{S}_h(el_B, az_B) \\ \tilde{S}_v(el_B, az_B) \\ \tilde{R}_{\text{hv}}(el_B, az_B, 0) \\ \tilde{R}^*_{\text{hv}}(el_B, az_B, 0) \end{bmatrix} \approx \left( \boldsymbol{TR} \times \frac{1}{TR_{11}} \right)^{-1} \begin{bmatrix} \hat{S}_h(el_B, az_B) \\ \hat{S}_v(el_B, az_B) \\ \hat{R}_{\text{hv}}(el_B, az_B, 0) \\ \hat{R}^*_{\text{hv}}(el_B, az_B, 0) \end{bmatrix}, \tag{2.14}$$

where the scaling by $TR_{11}$ ensures that levels of corrected second-order estimates remain within reasonable proximity to those of non-corrected ones. Hence, the first step in designing the correction matrix **CM** to correct for beamsteering and cross-coupling biases at each beamsteering angle is to define it as

$$\boldsymbol{CM} = \left( \boldsymbol{TR} \times \frac{1}{TR_{11}} \right)^{-1}. \tag{2.15}$$

Next, the bottom row of **CM** is discarded as it is not needed since the bottom element in the leftmost vector in (2.13) is the complex conjugate of the element above it. Finally, the **CM** matrix elements are scaled relative to broadside as

$$\boldsymbol{CM}(2,:) = \boldsymbol{CM}(2,:) \times \frac{1}{CM^B_{22}}$$

$$\boldsymbol{CM}(3,:) = \boldsymbol{CM}(3,:) \times \frac{exp(-j \, arg\{CM^B_{33}\})}{\sqrt{CM^B_{22}}} \tag{2.16}$$

where $CM^B_{22}$ and $CM^B_{33}$ are the elements of **CM** matrix at broadside. Corrected second order estimates may then be computed as

$$\begin{bmatrix} \tilde{S}_h(el_B, az_B) \\ \tilde{S}_v(el_B, az_B) \\ \tilde{R}_{\text{hv}}(el_B, az_B, 0) \end{bmatrix} \approx \boldsymbol{CM} \begin{bmatrix} \hat{S}_h(el_B, az_B) \\ \hat{S}_v(el_B, az_B) \\ \hat{R}_{\text{hv}}(el_B, az_B, 0) \\ \hat{R}^*_{\text{hv}}(el_B, az_B, 0) \end{bmatrix}, \tag{2.17}$$

and used for estimation of polarimetric variables as

17

$$\hat{Z}_{\text{DR}}(az_B, el_B) = 10 \, log_{10} \left[ \frac{\tilde{S}_h(az_B, el_B)}{\tilde{S}_v(az_B, el_B)} \right] - BS\_BIAS(Z_{\text{DR}}),$$

$$|\hat{\rho}_{\text{hv}}(az_B, el_B, 0)| = \frac{|\tilde{R}_{\text{hv}}(az_B, el_B, 0)|}{\sqrt{\tilde{S}_h(az_B, el_B)\tilde{S}_v(az_B, el_B)}},$$

$$\hat{\phi}_{\text{DP}}(az_B, el_B) = arg\{\tilde{R}_{\text{hv}}(az_B, el_B, 0)\} - BS\_BIAS(\phi_{\text{DP}}), \tag{2.18}$$

where $BS\_BIAS(Z_{\text{DR}})$ and $BS\_BIAS(\phi_{\text{DP}})$ are biases of $Z_{\text{DR}}$ and $\phi_{\text{DP}}$ at broadside, respectively. Note that the correlation coefficient estimates are impervious to variations of copolar patterns in gains and phases and therefore do not need to be corrected using broadside bias. This product, however, may be adversely affected if H and V copolar beams exhibit appreciable discrepancies in boresight and/or main beam shapes, which could result in disparate volumes of space sampled by the H and V main beams. This effect, if significant, would introduce noteworthy biases in the correlation coefficient estimates. We have not yet detected such effect in the ATD data. The results obtained with simulated time series, however, suggest that correlation coefficient estimates are affected by cross-coupling biases.

The approach to polarimetric variable computation presented in (2.18) is convenient because it allows for separation of copolar and cross-polar beam measurement procedures and the broadside bias measurement procedure. This is important because the former procedure is lengthy and it would not be practical to execute it on a daily basis. The broadside bias measurement procedure, however, takes much shorter to execute and measurements may be taken on daily basis. Hence, this procedure may capture system bias variations in relatively short timescales.

The use of full correction matrices that require precise knowledge of both the antenna copolar and cross-polar patterns (at and around beam peaks) was assessed by Ivić (2018) using simulated time series. This analysis suggests that the full correction is extremely sensitive to errors in cross-polar beam measurements when no cross-coupling mitigation is applied [i.e., $\alpha_h(m) = \alpha_v(m) = 0$]. If pulse-to-pulse phase coding is applied, then the main requirement for the applied phase codes is that

$$\sum_{m=0}^{M-1} exp\{\pm j[\alpha_v(m) - \alpha_h(m)]\} = 0, \tag{2.19}$$

which means that the complexity of elements in **TR** is reduced because products in (2.11) weighted by (2.19) ideally reduce to zero. In reality, the efficacy of this effect is dependent on the accuracy of the phases realized in the antenna hardware. Assuming perfect accuracy of the phase codes applied on transmission,

the analysis in Ivić (2018) suggests that the **CM** derived from phase coded time series is more robust and less sensitive to errors in cross-polar beam measurements.

Another approach is to focus on correcting only the effects of copolar patterns whereby the mitigation of cross-coupling biases is limited by the efficacy of pulse-to-pulse phase coding. This approach is dubbed "partial correction" in which case the elements of **TR** are computed using only measurements of copolar beams while setting the values of cross-polar beams to zero (i.e., $F_p^x = 0$ in **TR**). In such a case, the **CM** reduces to

$$CM = \begin{bmatrix} 1 & 0 & 0 & 0 \\ 0 & C_{22}(az_B, el_B) & 0 & 0 \\ 0 & 0 & C_{33}(az_B, el_B) & 0 \end{bmatrix},$$ (2.20)

where

$$C_{22}(az_B, el_B) = \frac{\sum_{\theta_n} \sum_{\phi_n} |T_h^{co}(az_B, el_B, \phi_n, \theta_n) R_h^{co}(az_B, el_B, \phi_n, \theta_n)|^2}{\sum_{\theta_n} \sum_{\phi_n} |T_v^{co}(az_B, el_B, \phi_n, \theta_n) R_v^{co}(az_B, el_B, \phi_n, \theta_n)|^2} \times$$

$$\frac{\sum_{\theta_n} \sum_{\phi_n} |T_v^{co}(0°, 0°, \phi_n, \theta_n) R_v^{co}(0°, 0°, \phi_n, \theta_n)|^2}{\sum_{\theta_n} \sum_{\phi_n} |T_h^{co}(0°, 0°, \phi_n, \theta_n) R_h^{co}(0°, 0°, \phi_n, \theta_n)|^2},$$

$$C_{33}(az_B, el_B) = \frac{\sum_{\theta_n} \sum_{\phi_n} |T_h^{co}(az_B, el_B, \phi_n, \theta_n) R_h^{co}(az_B, el_B, \phi_n, \theta_n)|^2}{\sum_{\theta_n} \sum_{\phi_n} \begin{Bmatrix} [T_h^{co}(az_B, el_B, \phi_n, \theta_n) R_h^{co}(az_B, el_B, \phi_n, \theta_n)]^* \times \\ T_v^{co}(az_B, el_B, \phi_n, \theta_n) R_v^{co}(az_B, el_B, \phi_n, \theta_n) \end{Bmatrix}} \times$$

$$exp\left[-j\, arg\left\{\sum_{\theta_n} \sum_{\phi_n} \begin{Bmatrix} [T_h^{co}(0°, 0°, \phi_n, \theta_n) R_h^{co}(0°, 0°, \phi_n, \theta_n)]^* \times \\ T_v^{co}(0°, 0°, \phi_n, \theta_n) R_v^{co}(0°, 0°, \phi_n, \theta_n) \end{Bmatrix}\right\}\right] \times$$

$$\sqrt{\frac{\sum_{\theta_n} \sum_{\phi_n} |T_v^{co}(0°, 0°, \phi_n, \theta_n) R_v^{co}(0°, 0°, \phi_n, \theta_n)|^2}{\sum_{\theta_n} \sum_{\phi_n} |T_h^{co}(0°, 0°, \phi_n, \theta_n) R_h^{co}(0°, 0°, \phi_n, \theta_n)|^2}}.$$ (2.21)

The partial correction approach is currently used by ATD signal processor. The reason for this is that at this stage of research we are focusing on the accurate measurements of copolar beams to correct the beamsteering biases as well as ways to maintain the accuracy of these corrections over time. In light of the latter, the broadside calibration is important due to its short duration which allows for capturing the varying system biases in a timely manner. Further, the research conducted so far indicates the pulse-to-pulse phase coding to be effective at mitigating the cross-coupling biases at lower elevations.

# 3. Signal processing to produce polarimetric radar data

The meteorological data acquired through the ATD undergoes the following checks and calibrations:

- Waveform verification: This verification process ensures that the transmit/receive waveforms adhere to the designated specifications and do not pose any harm to the antenna. Waveforms that fail to meet the requirements are excluded from loading into the exciter and are ineligible for data collection purposes.

- Range calibration: This calibration procedure establishes the necessary parameters for accurately placing radar returns at their correct range positions. It takes into consideration all system delays and processing factors that could impact the perceived range of targets. The range calibration value is a function of the waveform.

- Absolute RCS calibration: This process involves determining the calibration constant conventionally known as the "SYSCAL" (system reflectivity calibration constant). It enables the production of calibrated radar reflectivity values. This calibration value is also a function of the waveform.

- Beamsteering and cross-coupling bias calibration: This calibration process determines the "scan-loss" corrections for measured powers in the horizontal (H) and vertical (V) polarizations. It also calculates the differential power and phase offsets between the copolar H and V polarizations as a function of the electronic beamsteering angle relative to the broadside position. It is important to note that these bias corrections are relative to the broadside position and must be combined with the broadside calibration constants to generate accurately calibrated polarimetric data.

- Broadside calibration: This calibration procedure calculates the differential power and phase offsets between the horizontal (H) and vertical (V) polarizations at the broadside position. In radar using parabolic antennas, these offsets are commonly known as the " $Z_{DR}$ system bias" and "initial system $\phi_{DP}$ bias," respectively.

The following outlines the fundamental processing steps employed to produce calibrated reflectivity and polarimetric variables on the ATD.

- Reflectivity:

1. Estimate the mean signal power, $\hat{S}_h$, in the H channel by computing the total mean power, $\hat{P}_h$, and subtracting the noise power obtained with the Radial-by-Radial Noise (RBRN, Ivić et al. 2014) estimator, $N_h$. That is,

$$\hat{S}_h = \hat{P}_h - N_h. \tag{3.1}$$

2. Compute a raw reflectivity estimate (in dBZ units) using the range, $R$ (in km), as adjusted by the waveform-dependent range-calibration constant, and compensating for atmospheric attenuation (*ATMOS,* typically 0.01 dB/km). That is,

$$\hat{Z}_{\text{raw}} = 10 log_{10}\hat{S}_h + 20\, log_{10}R + ATMOS * R. \tag{3.2}$$

3. Compute the final reflectivity estimate by adding the broadside reflectivity calibration constant (*SYSCAL*) and compensating for the scan loss (*SL*), which is a function of beamsteering azimuth ($az_B$) and elevation ($el_B$) angles (where $\phi$ and $\theta$ are spherical coordinates relative to the antenna face). That is,

$$\hat{Z} = \hat{Z}_{\text{raw}} + SYSCAL + SL(az_B, el_B), \tag{3.3}$$

where

$$SL(az_B, el_B) = -10\, log_{10}\left[\frac{\sum_{\theta_n}\sum_{\phi_n}\left|T_h^{\text{co}}(az_B,el_B,\phi_n,\theta_n)R_h^{\text{co}}(az_B,el_B,\phi_n,\theta_n)\right|^2}{\sum_{\theta_n}\sum_{\phi_n}\left|T_h^{\text{co}}(0°,0°,\phi_n,\theta_n)R_h^{\text{co}}(0°,0°,\phi_n,\theta_n)\right|^2}\right]. \tag{3.4}$$

Note that this calibration is conducted under the assumption that the cross-coupling effects are not appreciable in the estimates of signal powers in the H and V channels.

- Polarimetric Variables:

1. Estimate the mean signal powers in the H and V channels, $\hat{S}_h$ and $\hat{S}_v$, by computing the total mean powers and subtracting the channel-specific noise powers.

2. Estimate the cross-correlation at lag-0 [i.e., $\hat{R}_{hv}(0)$] between the H and V channels.

3. Compute the corrected power and cross-correlation estimates using the beamsteering and cross-coupling bias correction matrices, which are a function of radar variable ($x$) as well as beamsteering azimuth ($\phi$) and elevation ($90° - \theta$) angles.

$$
\begin{bmatrix} \tilde{S}_h^{(x)} \\ \tilde{S}_v^{(x)} \\ \tilde{R}_{hv}^{(x)}(0) \end{bmatrix} = \begin{bmatrix} C_{11}(x,\phi,\theta) & 0 & 0 \\ 0 & C_{22}(x,\phi,\theta) & 0 \\ 0 & 0 & C_{33}(x,\phi,\theta) \end{bmatrix} \begin{bmatrix} \hat{S}_h \\ \hat{S}_h \\ \hat{R}_{hv}(0) \end{bmatrix}. \tag{3.5}
$$

Note that the three polarimetric variables exhibit different cross-coupling bias levels which are functions of beamsteering direction (typically, cross-coupling biases increase as beam is steered away from principal planes).

4. Compute the polarimetric variables from the variable-specific corrected covariances using the conventional estimators. That is,

$$
\hat{Z}_{DR,raw} = 10\,log_{10}\left(\frac{\tilde{S}_h^{(Z_{DR})}}{\tilde{S}_v^{(Z_{DR})}}\right),
$$

$$
\hat{\phi}_{DP,raw} = arg\left[\tilde{R}_{hv}^{(\phi_{DP})}(0)\right],
$$

$$
|\hat{\rho}_{hv}| = \frac{\left|\tilde{R}_{hv}^{(|\rho_{hv}|)}(0)\right|}{\sqrt{\tilde{S}_h^{(|\rho_{hv}|)}\tilde{S}_v^{(|\rho_{hv}|)}}}. \tag{3.6}
$$

5. For differential reflectivity and differential phase, subtract the corresponding biases computed via broadside calibration (denoted as "*SYS_ZDR*" for "$Z_{DR}$ system bias" and "*SYS_PHIDP*" for the "initial system $\Phi_{DP}$ bias"). That is,

$$
\hat{Z}_{DR} = \hat{Z}_{DR,raw} - SYS\_ZDR,
$$

$$
\hat{\phi}_{DP} = \hat{\phi}_{DP,raw} - SYS\_PHIDP. \tag{3.7}
$$

To derive elements of the correction matrices, an accurate characterization of the copolar and cross-polar antenna pattern main beams is needed. Detailed procedures for measurements of such beams are described in the subsequent section.

# 4. Techniques to Measure Polarimetric Calibration Parameters

This section describes the polarimetric calibration processes implemented for the ATD in more detail.

## 4.1  Range and Absolute RCS Calibration (Cal 05)

Range and RCS calibration are essential for a weather radar to estimate reflectivity from received signal power. Moreover, accurate range calibration is also essential for placing the returns in range with respect to the radar. For the ATD, a calibration "recipe" (Cal 05) was developed to compute the range calibration constant and SYSCAL values for the waveforms that are used during operations.

To collect the required data for range and RCS calibration, the ATD antenna is first mechanically positioned in azimuth and elevation so that the broadside beam points to the far field (FF) probe located on the calibration tower. After properly positioning the ATD antenna, the calibration data are collected through the following steps: 1) the ATD transmits a series of pulses that are received by the FF probe; 2) these received pulses at the FF probe pass through an optical delay line (ODL); 3) the delayed signals are retransmitted by the FF probe towards the ATD antenna; and 4) the ATD processes the received signals through the digital signal processing (DSP) chain that are used to process weather data. This system set up is illustrated in Figure 4.1. These steps are repeated for each waveform to be calibrated, and the output for each waveform is a radial of reflectivity data. Since the signal goes through the transmit chain, the receive chain, and the DSP, all system effects that could impact range or RCS are accounted for in this procedure. The ODL length is set to 100 µs for the pulse-compression long pulse and 30 µs for the fill pulse, which adds 15 km and 4.5 km to the apparent range of the FF probe signal, respectively.



*Figure 4.1. Depiction of system set up for range and RCS calibration.*

For each waveform, the range calibration constant is computed as the difference between expected range and the apparent range of the FF probe signal. Figure 4.2 shows an example of the received signal power (blue curve) corresponding to a 40 µs pulse-compression pulse from the FF probe. The range for each received sample is computed by multiplying the range sampling interval (225 m for the ATD weather data)

with its range bin index, where the first range bin has an index of 0. The peak of the received power and its immediate neighboring samples (indicated by the black X markers) are used to construct a parabolic fit (red curve) around the peak, and the maximum of the parabolic fit (indicated by the green dot) is the apparent range of the FF probe signal. When the true peak of the FF probe signal falls near the center of a resolution volume, the range of the maximum of the parabolic fit (green dot) should be close to the range of the received sample with peak power, as shown in the example in Figure 4.2. On the other hand, when the true peak of the FF probe signal falls near the edge of a resolution volume, the range of the maximum of the parabolic fit would be located between the range of two receive samples with approximately equal power. In this case, using the range of the maximum of the parabolic fit as the apparent range of the FF probe signal improves the accuracy of the range calibration. Once the apparent range is determined, the range calibration constant is computed as the difference between the expected range and the apparent range. In the example shown in Figure 4.2 resulted in a range calibration constant of 0.715 km.
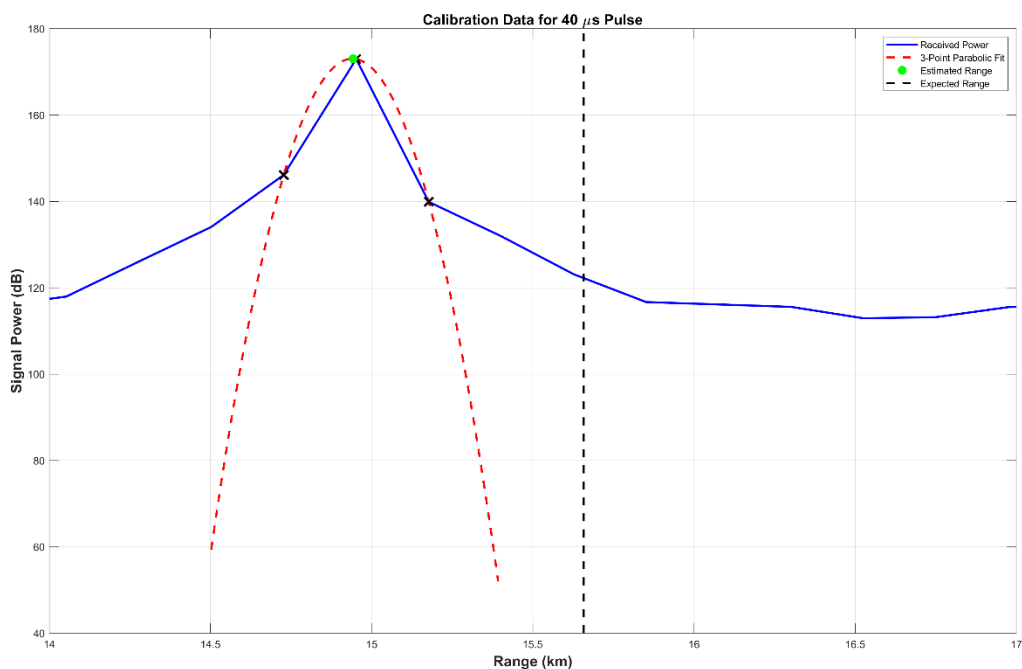


*Figure 4.2. Received signal power (blue curve) and associated parabolic fit (red curve). The difference between the expected range (black dashed line) and the apparent range (green dot) is the range calibration constant.*

After computing the range calibration constant, a new SYSCAL is computed in three steps. First, the received signal power is computed from reflectivity by reversing (3.2) and (3.3). Since the data are all collected at broadside, the scan loss term in (3.3) is constant between different calibration runs and can be ignored. In this step, the range calibration constant and SYSCAL are the values used by the weather DSP. After computing the received signal power, (3.2) is used to compute the raw reflectivity estimate. In this step, $R$ is computed using the new range calibration constant. The final step is to compute the new SYSCAL value by subtract the raw reflectivity estimate corresponding to the FF probe signal from a known constant. The value of this known constant was determined empirically by minimizing the difference in reflectivity between the ATD and KTLX, which was assumed to be well calibrated. Currently, the value of this constant is 69.6737 for the pulse-compression long pulse and 52.2937 for the fill pulse. Future comparisons between ATD data and KTLX data might result in updates to these values.

During the 2023 spring season, this calibration was executed successfully 55 times between April 4th and June 15th. Figure 4.3 shows the range calibration constants for pulse-compression long pulses computed from these 55 runs. The x-axis is the pulse length ranging from 30 µs to 79 µs; the y-axis is the date of the measurement; and the color of each bin indicates the range calibration constant in km. First, note that the range calibration constant increases as the pulse length increases. This is because the range of the first received sample ($R_0$) is a component of the range calibration constant and it is proportional to the pulse length divided by 2. Moreover, for each pulse length, the range calibration constant is consistent between the 55 runs. Figure 4.4 shows the standard deviation of the range adjustment constant in m for the different pulse lengths. The standard deviation varies between 0 and 30 m for the different pulse lengths with a periodic pattern repeating every 3 µs. Since these standard deviations are much smaller than the range sampling interval for the ATD (225 m), the variability in the range calibration constants for pulse-compression long pulses has almost no effect on the ability to accurately estimate reflectivity and place returns in range with respect to the radar.
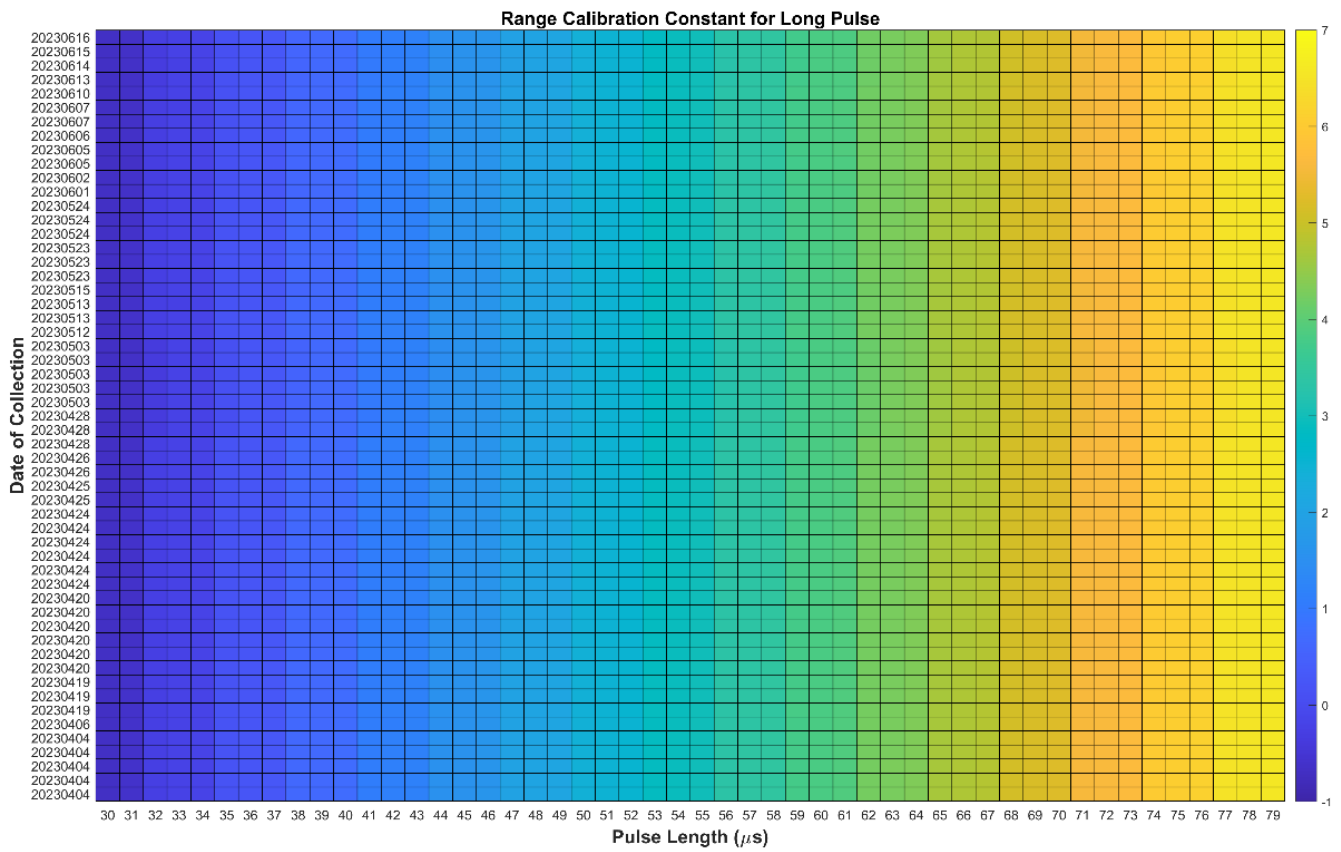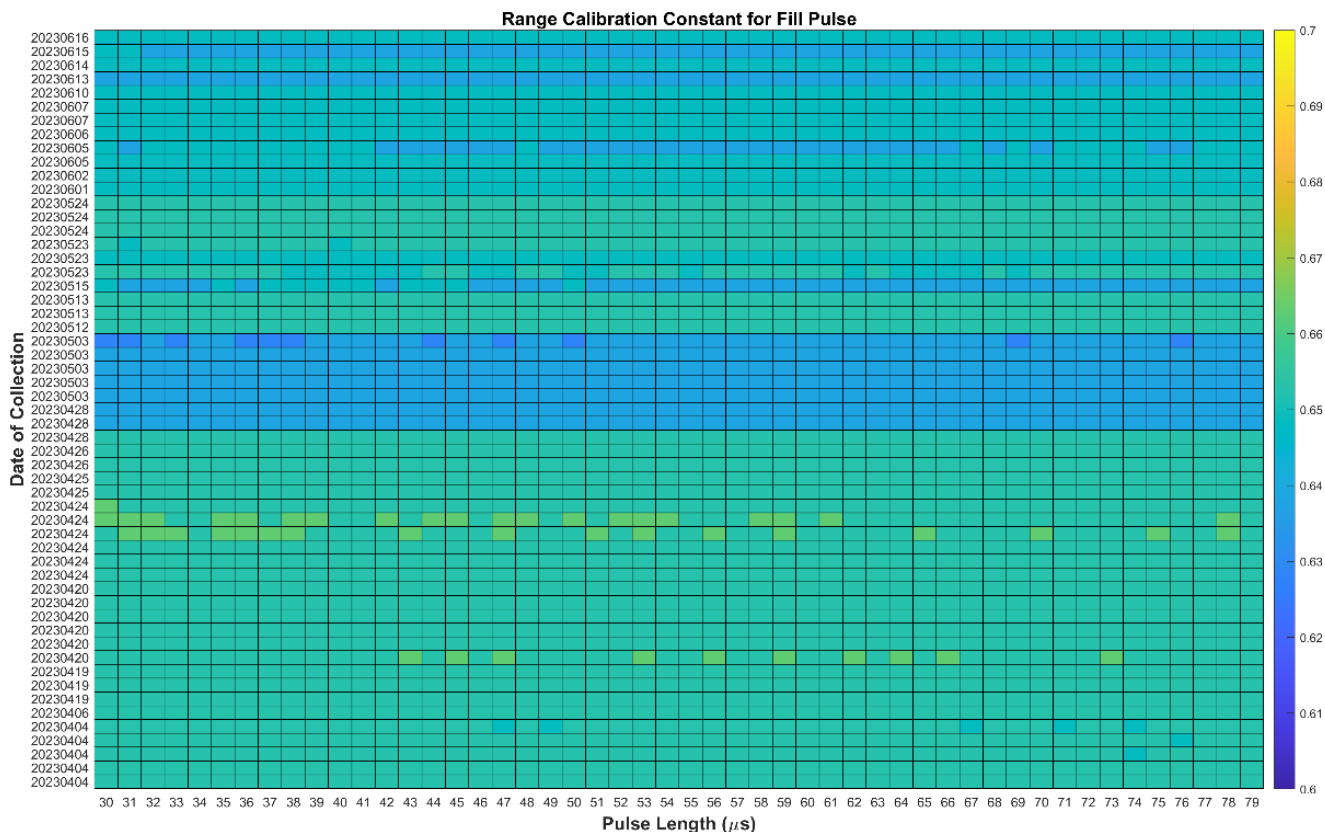
*Figure 4.3. Range calibration constant for pulse-compression long pulses.*
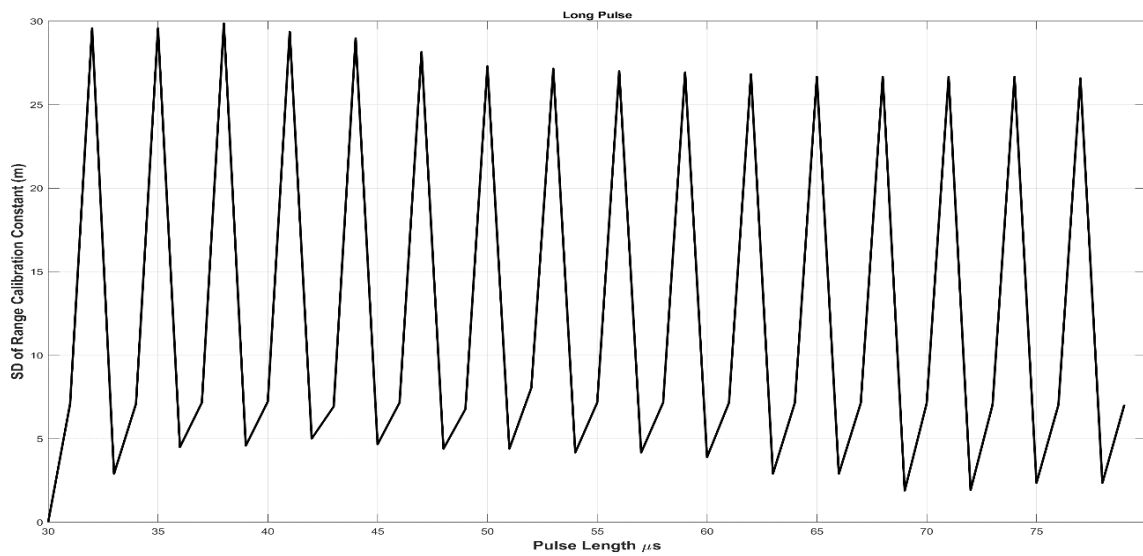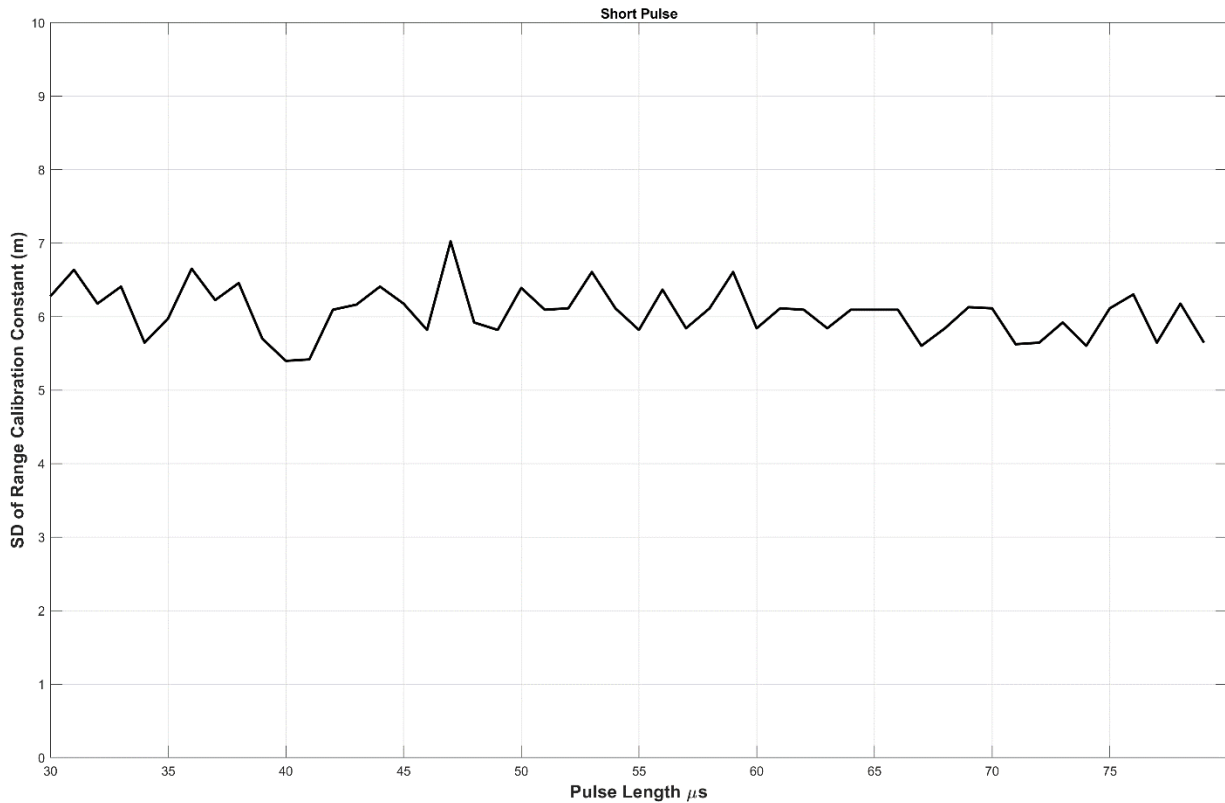


*Figure 4.4. Standard deviation of the range calibration constants for the pulse-compression long pulses.*

26

Figure 4.5 shows the range calibration constants for the fill pulses computed from the successful runs. Here, the x-axis is the pulse length of the pulse-compression long pulse that preceded the fill pulse in the transmit waveform. Since the pulse length of the fill pulse is constant for the varying pulse compression long pulses, the range calibration constant for the fill pulses is constant as well. Note the range of the color scale for Figure 4.5 is 0.1 km, so the variations among different runs are comparable to the variations seen for the long pulse. Figure 4.6 shows the standard deviation of the range adjustment constant in m for the fill pulses is between 5 to 7 m for all pulse lengths. Similar to the results for the pulse-compression long pulses, these variabilities will have almost no effect on the ability to accurately estimate reflectivity and place returns in range with respect to the radar for the fill pulses.



*Figure 4.5. Range calibration constant for fill pulses.*

*Figure 4.6. Standard deviation of the range calibration constants for the fill pulses.*

Figure 4.7 shows the SYSCAL values for pulse-compression long pulses computed from the successful runs. The x-axis is the pulse length ranging from 30 μs to 79 μs; the y-axis is the date of the measurement; and the color of each bin indicates the SYSCAL value in dB units. Similar to the range calibration constant, SYSCAL values for the pulse-compression long pulses also changed as the pulse length changed. In general, it dropped from approximately -100 dB for a 30-μs pulse to -110 dB for a 79-μs pulse. This is due to longer pulses having higher pulse-compression gain compared to shorter pulses. Among the successful runs, SYSCAL values show some variations. For example, the second run from April 28th resulted in noticeably smaller SYSCAL values across all pulse lengths while the last run from May13[th] resulted in noticeably larger SYSCAL values. Figure 4.8 shows the standard deviation of the SYSCAL values for the pulse-compression long pulses. For pulses with length between 30 and 58 μs, the standard deviation is about 0.8 dB. It increases to about 0.9 dB for the 59-μs pulse and slowly decreases to 0.8 dB as the pulse length increase from 59 to 79 μs. The variations for SYSCAL values could be caused by system temperature changes or the presence of interference signals in the direction of the calibration tower. Because the FF

probe signal is delayed by the ODL, any external signal (e.g., weather) at the expected range of the FF probe signal could bias the SYSCAL computations.
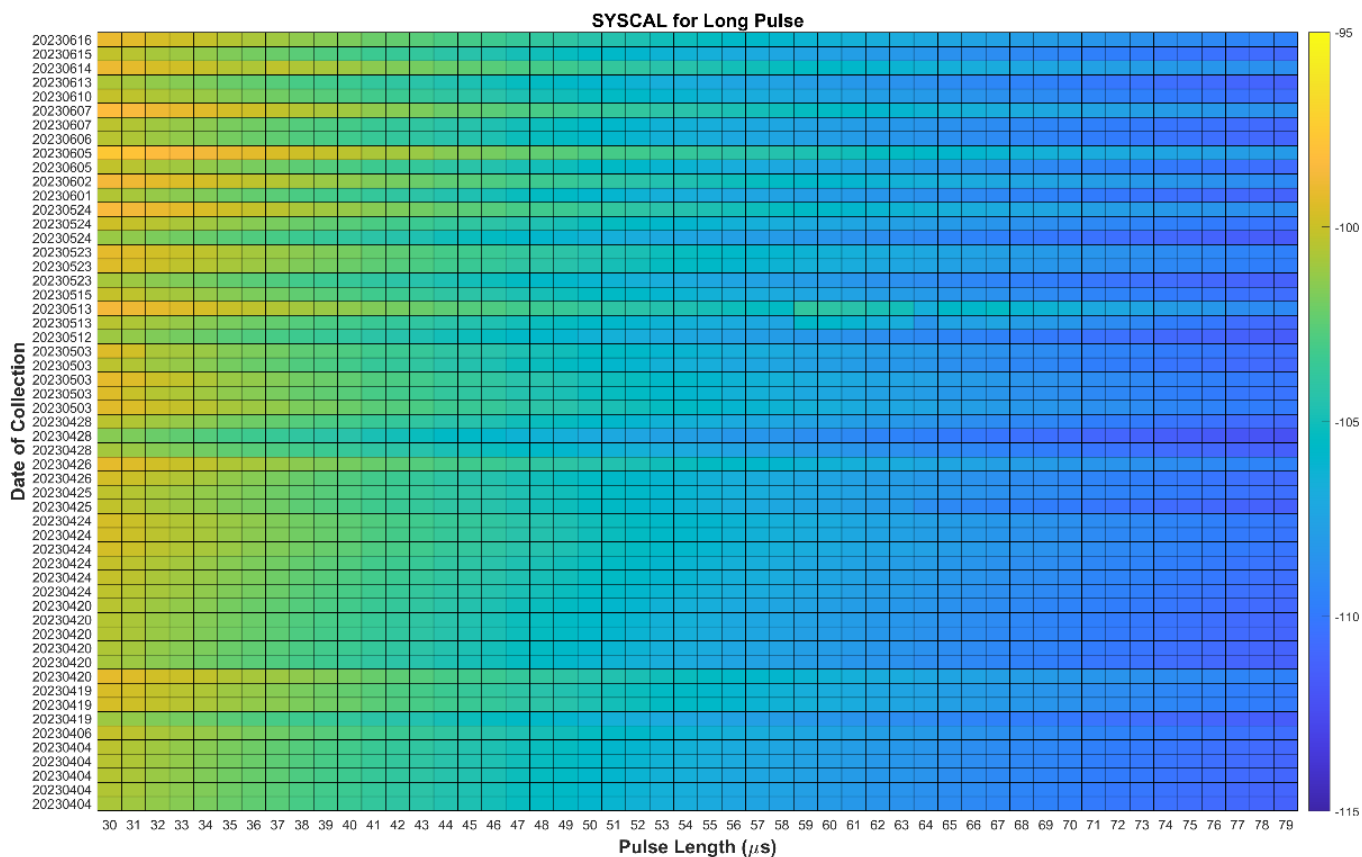


*Figure 4.7. SYSCAL values for pulse compression long pulses.*
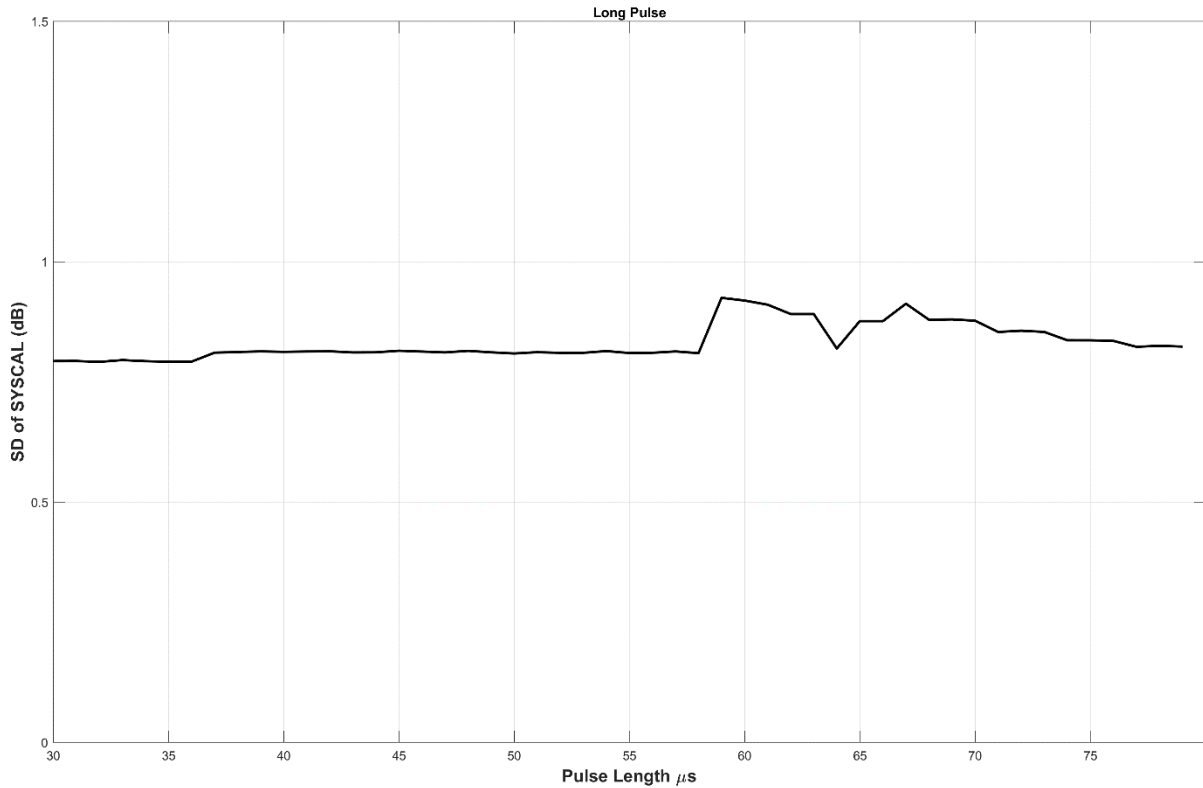
*Figure 4.8. Standard deviation of the SYSCAL values for the pulse-compression long pulses.*

Figure 4.9. shows the SYSCAL values for fill pulses computed from the successful runs. Here, the x-axis is the pulse length of the pulse-compression long pulse preceded the fill pulse in the transmit waveform. Similar to the range calibration constant, since the fill pulse length did not change, the SYSCAL value also stayed constant for the varying long-pulse length. Despite the smaller range of the color scale, the SYSCAL values for the fill pulse appear to have more variability compared to SYSCAL values for the long pulse. Figure 4.10 shows that the standard deviation of the SYSCAL values for the fill pulses is about 1 dB for all pulse lengths. Results in Figures 4.3 to 4.10 show that the range and RCS calibration results for the ATD are quite stable (repeatable) over an 11-week period. This implies that it is not necessary to execute this calibration before every weather collection.
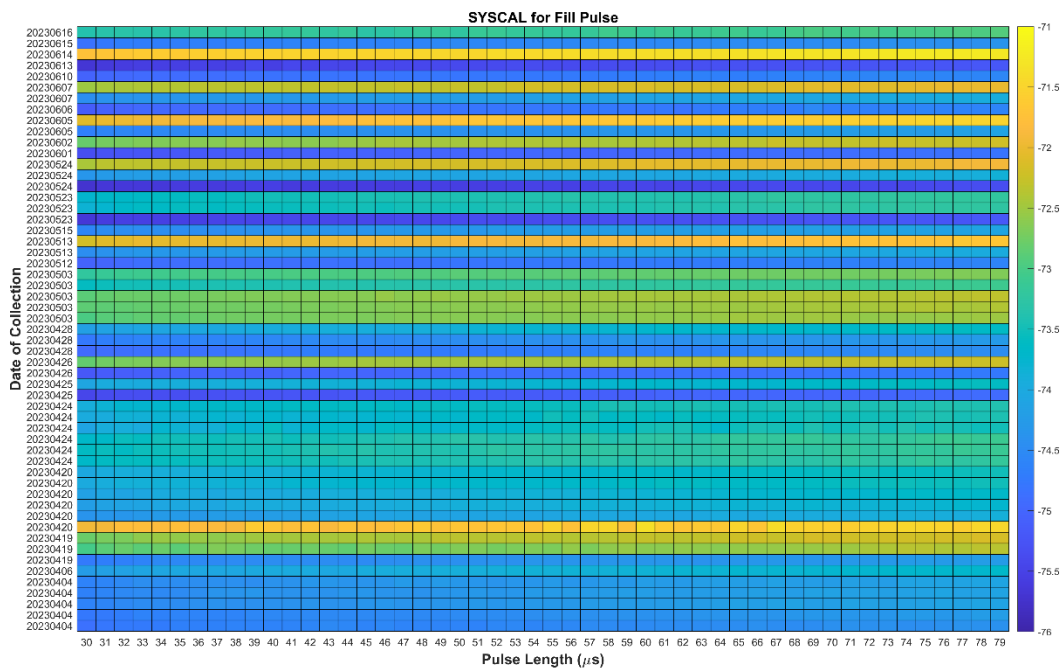
*Figure 4.9. SYSCAL values for the fill pulses.*
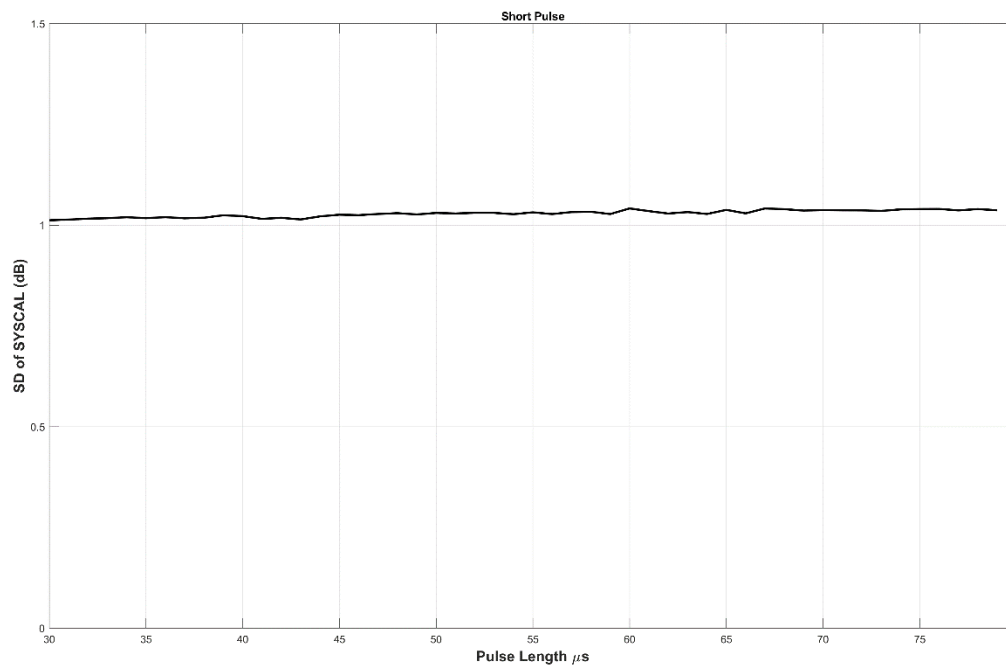


*Figure 4.10. Standard deviation of the SYSCAL values for the fill pulses.*

31

## 4.2 Beamsteering and Cross-Coupling Bias Calibration (Cal 07)

To conduct these measurements, the array must be mechanically positioned in azimuth and elevation so that the beam points to the far-field (FF) probe when electronically steered in the direction to be calibrated; thus, a mathematical framework was developed to compute the antenna mechanical position for each calibrated beamsteering angle. Data are collected at multiple beam steering positions covering an area of size $1° \times 1°$ in $0.1°$ steps around the calibrated beamsteering angle to create a quasi-pattern of the main beam. Data must be taken with the array elements transmitting and receiving, and with the calibration-tower probe commanded to vertical and horizontal polarization. Both co- and cross- polarization results are significant.

A measurement for each calibrated beamsteering angle is conducted with the ATD antenna having a yaw ($\gamma$), and pitch ($\beta$) relative to the FF probe location since the ATD antenna broadside points away from the FF probe location for calibrated electronic steering angles that do not coincide with broadside. The yaw and pitch are determined relative to the reference $xyz$ Cartesian coordinate system shown in Figure 4.11 and are related to the pedestal azimuth and elevation commands as

$$\gamma = az_P - az_H,$$
$$\beta = el_P. \tag{4.1}$$

In (4.1), $az_P$ and $el_P$ are the antenna mechanical positions while $az_H$ is the FF probe azimuth location relative to north. During the installation, the FF probe was tilted towards the ground and positioned in azimuth so that the broadside of the horn antenna approximately points towards the ATD antenna. Also, it is mounted on a motorized platform that allows it to rotate into horizontal, vertical or any other intermediate position.
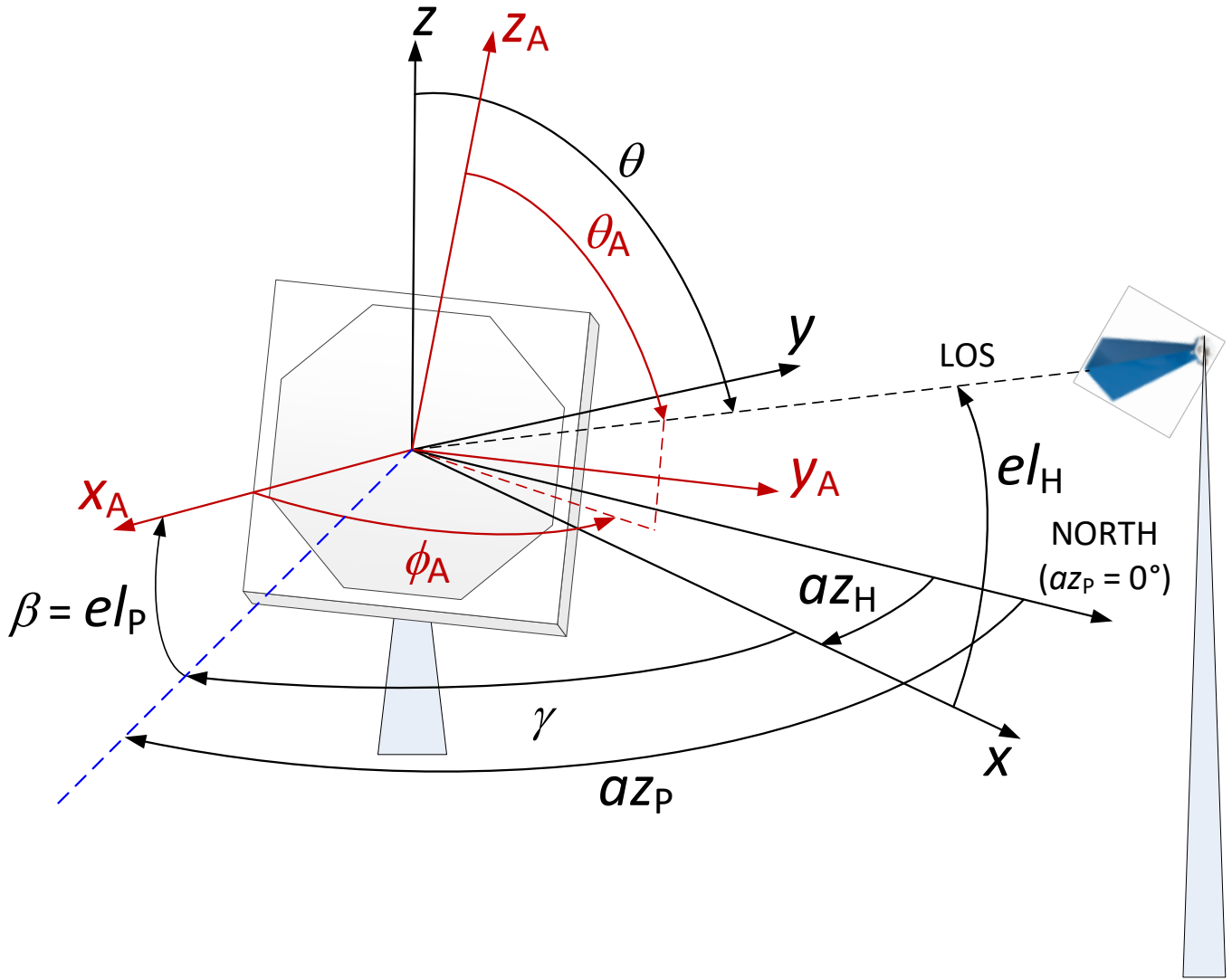
*Figure 4.11. Depiction of coordinate systems used to correct the beam measurements.*

In the case of the ATD antenna transmit beam measurements, the model that describes these at each antenna mechanical position and the associated electronic beam positions ($\phi_A$, $\theta_A$) is as follows

$$V_H^p(\alpha_n, \phi_A, \theta_A) = C_{Ht}(\boldsymbol{RPY_H} \times \boldsymbol{F_H})^t \times \boldsymbol{PY_{ATD}} \times \boldsymbol{T_{ATD}} \times \boldsymbol{E_{ATD}}. \tag{4.2}$$

In (4.2), the matrix $\mathbf{T_{ATD}}$ describes the ATD antenna beams in the spherical system $\phi\theta_A$ bound to the $xyz_A$ Cartesian coordinate system (shown in red in Figure 4.2) tied to the ATD antenna plane. These are the beams that are being measured. The $\mathbf{PY_{ATD}}$ is the 2×2 matrix that describes the effects of the ATD antenna pitch and yaw on $\mathbf{T_{ATD}}$ (i.e., it converts values in $\mathbf{T_{ATD}}$ that represent beams in $\phi\theta_A$ to their representation in spherical coordinates $\phi\theta$ tied to $xyz$ axes). This matrix is a function of $az_p$ and $el_p$ as well as the Line Of

Sight (LOS) position in the $\phi_A \theta_A$ and the $\phi\theta$ spherical coordinate systems. In the latter, the LOS is the line that connects the center of the ATD antenna to the FF probe center. Similarly, the 2×2 matrix $\mathbf{RPY_H}$ converts the FF probe pattern in a horizontal polarization from the coordinate system tied to the FF probe plane to $\phi\theta$ coordinates. This matrix can account for the FF probe tilt (incurred to aim the probe towards the ATD antenna location), a potential offset in the FF probe azimuth position (i.e., if the probe is not positioned in azimuth to point perfectly at the ATD antenna), as well as the FF probe rotation imposed to set the FF probe to a desired polarization. The vector $\mathbf{F_H}$ denotes the FF probe pattern values at the point that coincides with the LOS. It is

$$\boldsymbol{F_H} = \begin{bmatrix} H_h^{co} \\ H_h^{x} \end{bmatrix}, \tag{4.3}$$

where $H_h^{co}$, and $H_h^{x}$ denote the copolar and cross-polar FF probe pattern values at the LOS coordinates.

The measured complex value is $V_H^p(\alpha_n, \phi_A, \theta_A)$, where the superscript $p$ denotes the ATD antenna excited h or v port, and $\alpha_n$ (subscript $n$ denotes the measurement number) stands for the commanded rotation of the FF probe (it is either 0° or 90° in the case of these measurements).

Further simplification may be introduced as

$$\boldsymbol{F_H^t} \times \boldsymbol{RPY_H^t} \times \boldsymbol{PY_{ATD}} = [H_h^{co} \quad H_h^{x}] \times \begin{bmatrix} HM_{11}(\alpha_n) & HM_{12}(\alpha_n) \\ HM_{21}(\alpha_n) & HM_{22}(\alpha_n) \end{bmatrix}, \tag{4.4}$$

where the right-most matrix compresses the effects of the ATD antenna and the FF probe roll, pitch and yaw. It is computed using the knowledge of ATD antenna mechanical position in azimuth and elevation as well as the FF probe tilt towards the ground. Next, the following relations

$$HM_{11}(\alpha_n) = HM_{22}(\alpha_n),$$

$$HM_{12}(\alpha_n) = -HM_{21}(\alpha_n), \tag{4.5}$$

are used for further simplification as

$$\boldsymbol{F_H^t} \times \boldsymbol{RPY_H^t} \times \boldsymbol{PY_{ATD}} = [H_h^{co} \quad H_h^{x}] \times \begin{bmatrix} HM_{11}(\alpha_n) & HM_{12}(\alpha_n) \\ -HM_{12}(\alpha_n) & HM_{11}(\alpha_n) \end{bmatrix},$$

$$= [HM_{11}(\alpha_n) \quad HM_{12}(\alpha_n)] \begin{bmatrix} H_h^{co} & H_h^{x} \\ -H_h^{x} & H_h^{co} \end{bmatrix}. \tag{4.6}$$

If the FF probe polarization is set to V and then H, and the h port is excited in both cases, the following two measurements are made (note that commanding the FF probe to 0° and 90° sets its polarization to nearly vertical and horizontal, respectively)

$$V_H^h(0°) = C_{Ht}[HM_{11}(0°) \quad HM_{12}(0°)]\begin{bmatrix} H_h^{co} & H_h^x \\ -H_h^x & H_h^{co} \end{bmatrix}\begin{bmatrix} T_h^{co} \\ T_h^x \end{bmatrix},$$

$$V_H^h(90°) = C_{Ht}[HM_{11}(90°) \quad HM_{12}(90°)]\begin{bmatrix} H_h^{co} & H_h^x \\ -H_h^x & H_h^{co} \end{bmatrix}\begin{bmatrix} T_h^{co} \\ T_h^x \end{bmatrix}. \tag{4.7}$$

where dependencies on ($\phi_A$, $\theta_A$) are dropped from the notation for simplicity. The two measurements may be combined as

$$\begin{bmatrix} V_H^h(0°) \\ V_H^h(90°) \end{bmatrix} = C_{Ht}\begin{bmatrix} HM_{11}(0°) & HM_{12}(0°) \\ HM_{11}(90°) & HM_{12}(90°) \end{bmatrix}\begin{bmatrix} H_h^{co} & H_h^x \\ -H_h^x & H_h^{co} \end{bmatrix}\begin{bmatrix} T_h^{co} \\ T_h^x \end{bmatrix}. \tag{4.8}$$

Examination of (4.8) indicates that if values in the second 2×2 matrix (i.e., FF probe pattern values at LOS coordinates) were known, the ATD beams could be obtained as

$$C_{Ht}\begin{bmatrix} T_h^{co} \\ T_h^x \end{bmatrix} = \left\{\begin{bmatrix} HM_{11}(0°) & HM_{12}(0°) \\ HM_{11}(90°) & HM_{12}(90°) \end{bmatrix}\begin{bmatrix} H_h^{co} & H_h^x \\ -H_h^x & H_h^{co} \end{bmatrix}\right\}^{-1}\begin{bmatrix} V_H^h(0°) \\ V_H^h(90°) \end{bmatrix}. \tag{4.9}$$

This, however, is not the case so what the corrected measurements produce is

$$\begin{bmatrix} \tilde{T}_h^{co} \\ \tilde{T}_h^x \end{bmatrix} = C_{Ht}\begin{bmatrix} H_h^{co}T_h^{co} + H_h^x T_h^x \\ H_h^{co}T_h^x - H_h^x T_h^{co} \end{bmatrix} = \begin{bmatrix} HM_{11}(0°) & HM_{12}(0°) \\ HM_{11}(90°) & HM_{12}(90°) \end{bmatrix}^{-1}\begin{bmatrix} V_H^h(0°) \\ V_H^h(90°) \end{bmatrix}. \tag{4.10}$$

Because $H_h^{co}T_h^{co} \gg H_h^x T_h^x$, the copolar beam measurements produce approximately the value of $\sim H_h^{co}T_h^{co}$ (i.e., the product the ATD antenna and FF probe of copolar beams). The measurements of cross-polar beams result in $\sim H_h^{co}T_h^x$ if $H_h^{co}T_h^x \gg H_h^x T_h^{co}$. The latter condition is met if $T_h^x \gg H_h^x$, which suggests that the cross-polar beam measurements become increasingly more precise for electronic beamsteering angles that are farther away from the principal planes. This is because the power of ATD antenna cross-polar beams increase as the beam is electronically steered away from principal planes while their boresight always points at and around the broadside of the FF probe (where the cross-polar pattern of the FF probe exhibits the lowest levels). Analogously, the corrected measurements of V beams result in

$$\begin{bmatrix} \tilde{T}_v^x \\ \tilde{T}_v^{co} \end{bmatrix} = C_{Ht}\begin{bmatrix} H_h^{co}T_v^x + H_h^x T_v^{co} \\ H_h^{co}T_v^{co} - H_h^x T_v^x \end{bmatrix} = \begin{bmatrix} HM_{11}(0°) & HM_{12}(0°) \\ HM_{11}(90°) & HM_{12}(90°) \end{bmatrix}^{-1}\begin{bmatrix} V_H^v(0°) \\ V_H^v(90°) \end{bmatrix}. \tag{4.11}$$

Alternately, all measurements can be combined as

35

$$\begin{bmatrix} \tilde{T}_h^{co} & \tilde{T}_v^x \\ \tilde{T}_h^x & \tilde{T}_v^{co} \end{bmatrix} = C_{Ht} \begin{bmatrix} H_h^{co}T_h^{co} + H_h^x T_h^x & H_h^{co}T_v^x + H_h^x T_v^{co} \\ H_h^{co}T_h^x - H_h^x T_h^{co} & H_h^{co}T_v^{co} - H_h^x T_v^x \end{bmatrix}$$

$$= \begin{bmatrix} HM_{11}(0°) & HM_{12}(0°) \\ HM_{11}(90°) & HM_{12}(90°) \end{bmatrix}^{-1} \begin{bmatrix} V_H^h(0°) & V_H^v(0°) \\ V_H^h(90°) & V_H^v(90°) \end{bmatrix}. \tag{4.12}$$

to produce the corrected results in a 2×2 matrix form.

If the ATD antenna receive beams are measured, the model is

$$\begin{bmatrix} V_h(\alpha_n) \\ V_v(\alpha_n) \end{bmatrix} = C_{Hr}(PY_{ATD} \times R_{ATD})^t \times RPY_H \times F_H, \tag{4.13}$$

Then, because

$$PY_{ATD}^t \times RPY_H = (RPY_H^t \times PY_{ATD})^t = \begin{bmatrix} HM_{11}(\alpha_n) & HM_{21}(\alpha_n) \\ HM_{12}(\alpha_n) & HM_{22}(\alpha_n) \end{bmatrix}, \tag{4.14}$$

and using (4.5), results in

$$\begin{bmatrix} V_h(\alpha_n) \\ V_v(\alpha_n) \end{bmatrix} = C_{Hr} \begin{bmatrix} R_h^{co} & R_h^x \\ R_v^x & R_v^{co} \end{bmatrix} \begin{bmatrix} HM_{11}(\alpha_n) & -HM_{12}(\alpha_n) \\ HM_{12}(\alpha_n) & HM_{11}(\alpha_n) \end{bmatrix} \begin{bmatrix} H_h^{co} \\ H_h^x \end{bmatrix},$$

$$= C_{Hr} \begin{bmatrix} R_h^{co} & R_h^x \\ R_v^x & R_v^{co} \end{bmatrix} \begin{bmatrix} HM_{11}(\alpha_n)H_h^{co} - H_h^x HM_{12}(\alpha_n) \\ HM_{12}(\alpha_n)H_h^{co} + HM_{11}(\alpha_n)H_h^x \end{bmatrix},$$

$$= C_{Hr} \begin{bmatrix} R_h^{co} & R_h^x \\ R_v^x & R_v^{co} \end{bmatrix} \begin{bmatrix} H_h^{co} & -H_h^x \\ H_h^x & H_h^{co} \end{bmatrix} \begin{bmatrix} HM_{11}(\alpha_n) \\ HM_{12}(\alpha_n) \end{bmatrix}. \tag{4.15}$$

Combining the measurements at the FF probe commanded positions of 0° and 90° yields

$$\begin{bmatrix} V_h(0°) & V_h(90°) \\ V_v(0°) & V_v(90°) \end{bmatrix} = C_{Hr} \begin{bmatrix} R_h^{co} & R_h^x \\ R_v^x & R_v^{co} \end{bmatrix} \begin{bmatrix} H_h^{co} & -H_h^x \\ H_h^x & H_h^{co} \end{bmatrix} \begin{bmatrix} HM_{11}(0°) & HM_{11}(90°) \\ HM_{12}(0°) & HM_{12}(90°) \end{bmatrix} \tag{4.16}$$

Given, that the FF probe antenna patterns are not known, the corrected receive beam measurements yield

$$\begin{bmatrix} \tilde{R}_h^{co} & \tilde{R}_h^x \\ \tilde{R}_v^x & \tilde{R}_v^{co} \end{bmatrix} = C_{Hr} \begin{bmatrix} R_h^{co}H_h^{co} + R_h^x H_h^x & -R_h^{co}H_h^x + R_h^x H_h^{co} \\ R_v^x H_h^{co} + R_v^{co}H_h^x & -R_v^x H_h^x + R_v^{co}H_h^{co} \end{bmatrix}$$

$$= \begin{bmatrix} HM_{11}(0°) & HM_{11}(90°) \\ HM_{12}(0°) & HM_{12}(90°) \end{bmatrix}^{-1} \begin{bmatrix} V_h(0°) & V_h(90°) \\ V_v(0°) & V_v(90°) \end{bmatrix}. \tag{4.17}$$

On a typical weather scan, the ATD electronically scans a sector that spans ±45° in azimuth and 0°-20° in elevation while the antenna is stationary. This poses a requirement that beams be characterized for electronic steering angles in this domain. Accordingly, the calibration procedure currently performs beam

measurements at electronic beamsteering angles that span azimuths of ±45° in 3° steps and elevations -4° - 20° in 2° steps for beam measurements at a total of 31×13 = 403 mechanical positions. At each mechanical position, the magnitude and phase measurements of copolar (as exemplified in Figure 4.12) and cross-polar quasi-patterns are collected. Note that because the ATD antenna has a hard stop at -1° elevation, all measurements are conducted with the ATD antenna in the inverted (flipped) position (e.g., if the measurements are carried at broadside, the antenna is commanded to the elevation of 180° − $el_\mathrm{H}$, where $el_\mathrm{H}$ is the elevation at which the ATD antenna points directly towards the FF probe location when not inverted). The measurements take ~2.5 hours to complete.

An example of the measured copolar beam powers is presented in Figure 4.12 for a beam electronically steered at an azimuth of 45° and an elevation of 10°. The actual beam peak locations and the correction data are derived from such scans. An example of measured copolar beam peaks on transmit and receive are presented in Figure 4.14 (upper panels). Additionally, the offsets between the measured beam peaks and the FF probe location are shown in Figure 4.14 (lower panels). At each mechanical position, these offsets are measured as the differences between the calibrated beamsteering angle and the measured beam peak location. The systematic differences are caused by the antenna arm effects, which are not accounted by the mathematical model used to compute the antenna mechanical positions.

Because weather returns produce random signals, the polarimetric information about the observed weather is derived from second-order estimates that are the powers in H and V, as well as the cross-correlation between the H and V signals. The powers and phases for each calibrated beamsteering angle are computed as

$$\left|FB_p^c(\theta_A, \phi_A)\right|^2 = \frac{1}{\sum_{\theta_n}\sum_{\phi_n} I(\theta_n, \phi_n)} \sum_{\theta_n}\sum_{\phi_n} \left|\tilde{F}_p^c(\theta_n, \phi_n)\right|^2 I(\theta_n, \phi_n)$$

$$arg\{FB_p^c(\theta_A, \phi_A)\} = arg\left\{\frac{1}{\sum_{\theta_n}\sum_{\phi_n} I(\theta_n, \phi_n)} \sum_{\theta_n}\sum_{\phi_n} \tilde{F}_p^c(\theta_n, \phi_n)[\tilde{F}_h^{co}(\theta_n, \phi_n)]^* I(\theta_n, \phi_n)\right\} \qquad (4.18)$$

where $F$ is '$T$' or '$R$', $p$ is 'h' or 'v', and $c$ is 'co' or 'x'. In (4.18), $I(\theta_n, \phi_n)$ is used to determine which particular quasi-pattern measurements at ($\phi_n$, $\theta_n$) coordinates are used for power and phase computation. To obtain it, a peak power value is determined for each copolar quasi-pattern and the power values that are within the -6 dB of the peak power (for all four copolar quasi-patterns) are tagged with 1 and others with 0.

An example of raw transmit copolar beam power measurements is shown in the top panels of Figure 4.15. The measurements are very noisy, so they are smoothed via polynomial fitting (presented in the second row from the top in Figure 4.15). The same is performed for the receive copolar beams as exhibited in the third and fourth row panels in Figure 4.15. An example of raw uncorrected measurements of transmit and receive cross-polar beams is given in the top and third row panels of Figure 4.16. These indicate low cross-polar levels along the vertical principal plain that rapidly increase at beamsteering angles away from the vertical principal plane. Contrary to this, the cross-polar beams are expected to have the lowest levels at and around the horizontal and vertical principal planes. This indicates that the corrections of raw measurements (using the knowledge of the antenna and FF probe roll, pitch and yaw) are required to obtain more accurate measurements. Hence, the corresponding corrected cross-polar beams are presented in the second and the bottom row in Figure 4.7. These exhibit the cross-polar beam behavior that is much closer to the expected one. Nonetheless, the corrected cross-polar beams still exhibit uncharacteristic asymmetries relative to the vertical principal planes that are a consequence of imperfect polarizations of the FF probe. Namely, when the FF probe is commanded to 0°/90° it does not achieve perfect vertical/horizontal polarization due to an imperfect alignment during the FF probe assembly installation. Consequently, this increases a portion of the ATD antenna copolar signal that couples into the measurements of the cross-polar signal and vice versa. Because the cross-polar signals are much smaller than the copolar ones, they are affected more significantly by the imperfections incurred during the FF probe assembly installation. To mitigate the effects of polarization offsets, the corrected copolar and cross-polar embedded patterns are rotated numerically to achieve an optimal symmetry relative to 0° azimuth. The results are presented in Figure 4.17.
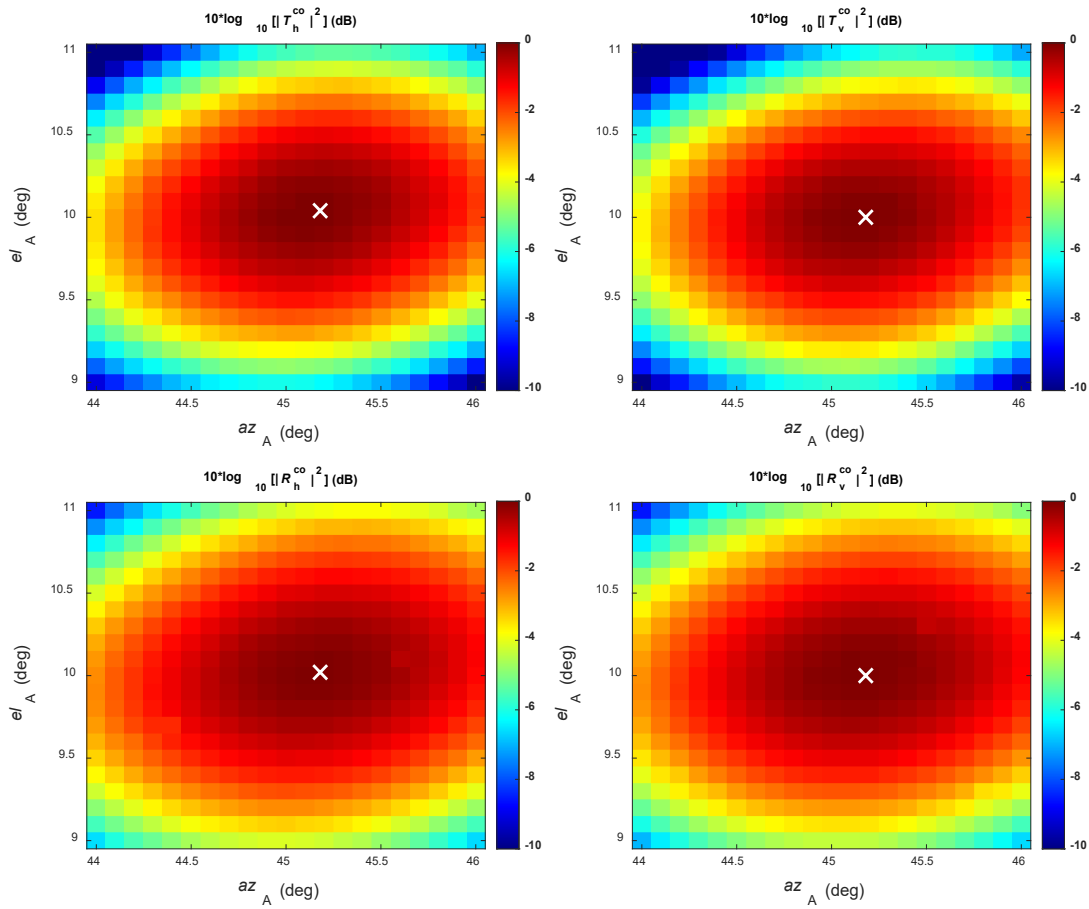
*Figure 4.12. An example of copolar beam quasi-patterns powers for transmit H (top left panel) and V (top right panel), as well as receive H (bottom left panel) and V (bottom right panel). The location of the beam peak is marked with a white 'x'.*
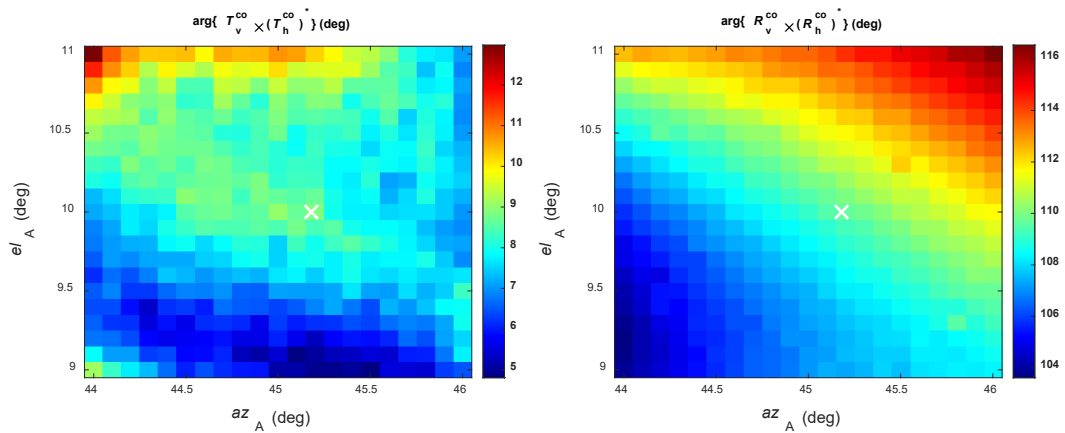


*Figure 4.13. An example of copolar beam quasi-patterns phases relative to H for transmit V (left panel) and receive V (right panel).*
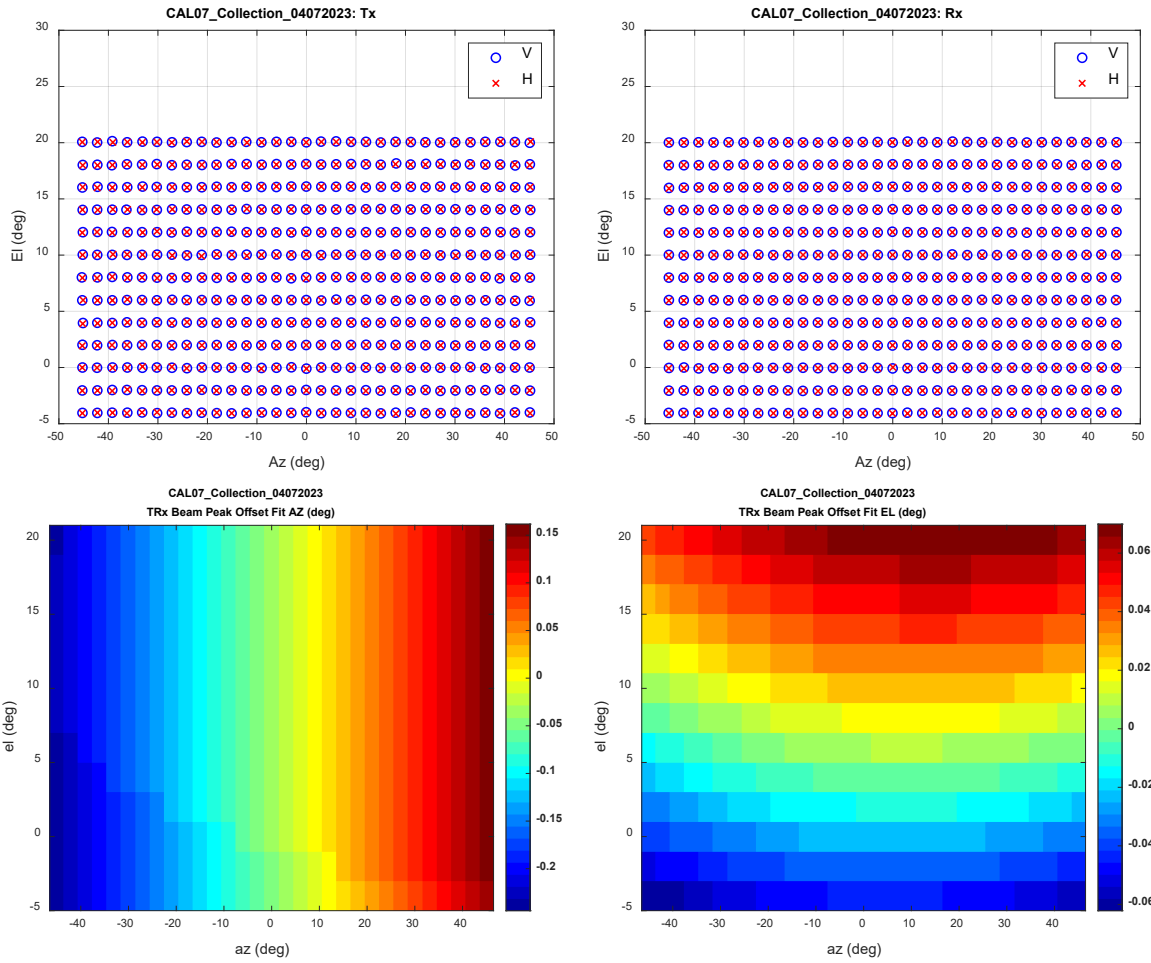
*Figure 4.14. Measured beam peak locations on transmit (top left panel) and receive (top right panel). Averaged transmit and receive offsets between the boresights and measured beam peaks.*
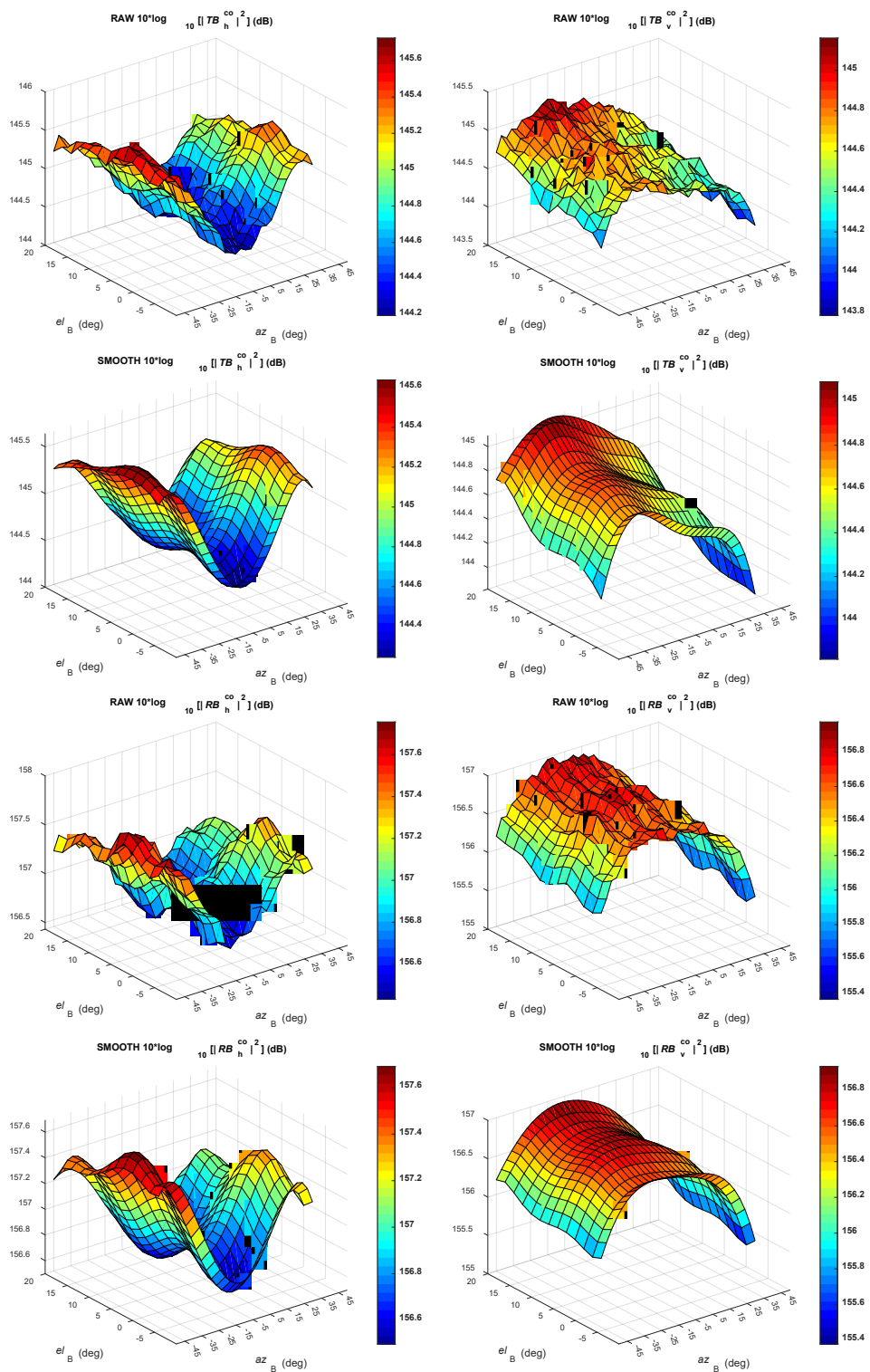
*Figure 4.15. An example of raw transmit (top panels)/receive (3rd row panels) and smoothed transmit (2nd row panels)/receive (bottom panels) copolar beam power measurements.*
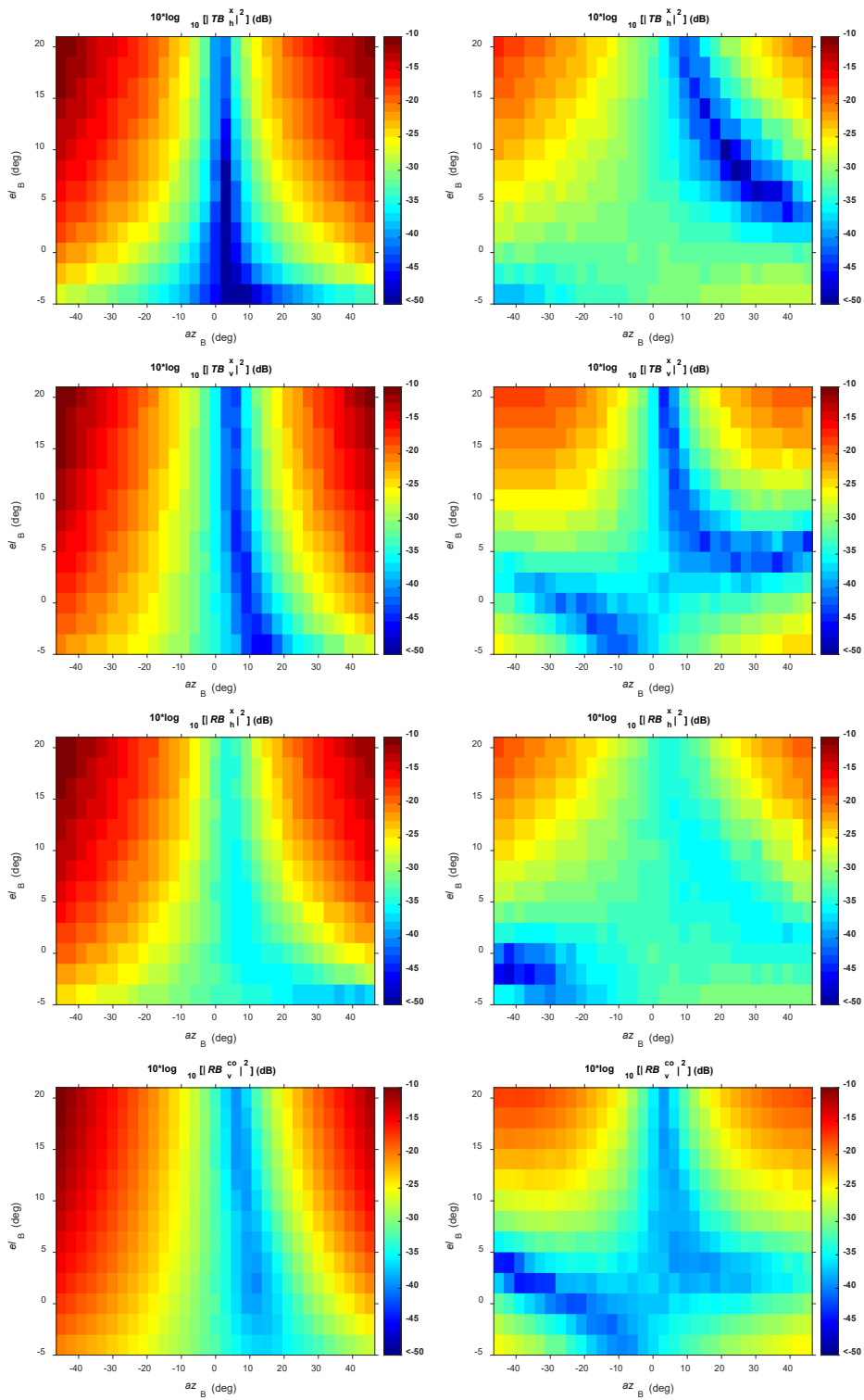
*Figure 4.16. Uncorrected (left column) and corrected (right column) cross-polar beam measurements on transmit (top two panels) and receive (bottom two panels)*
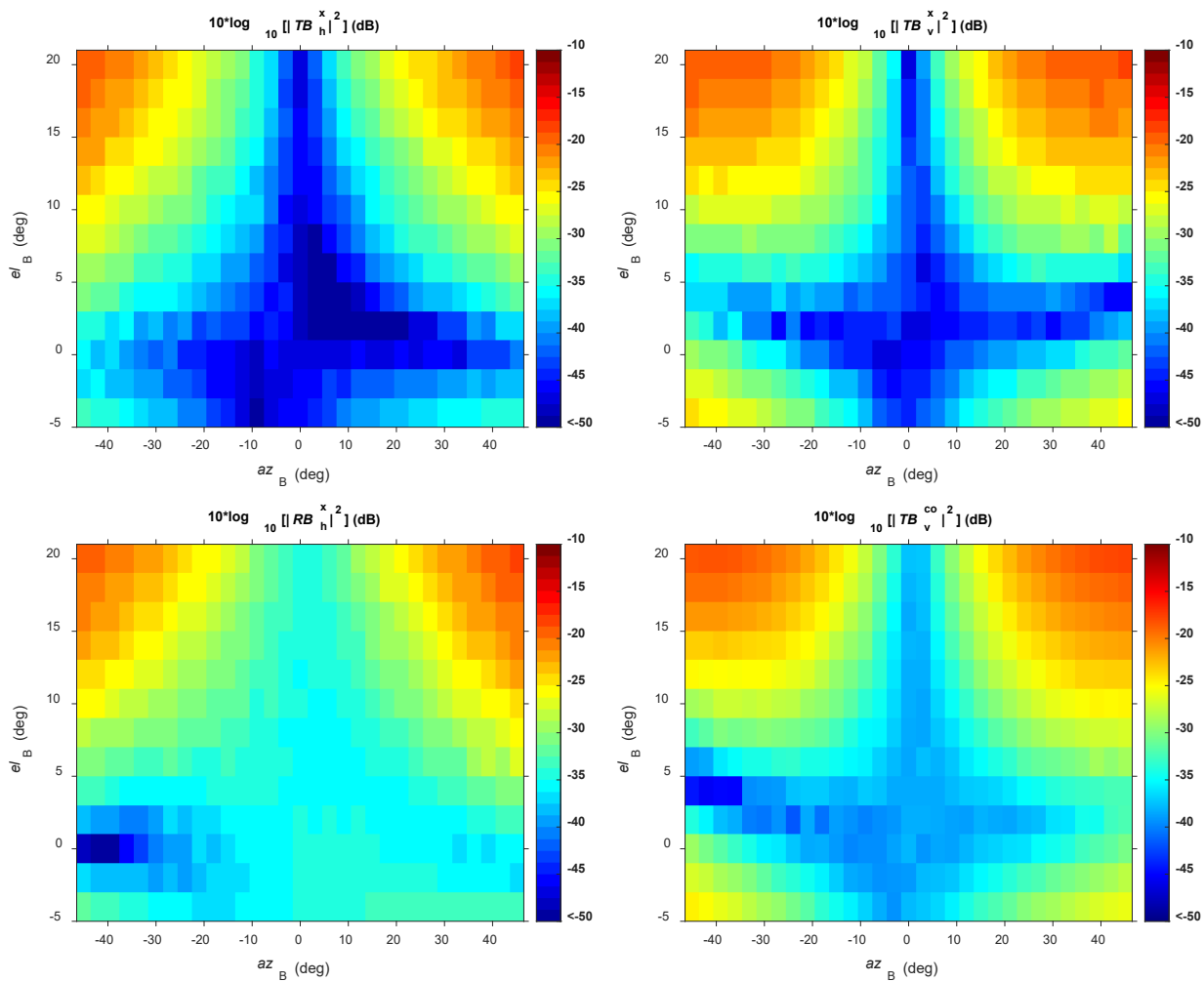
*Figure 4.17. Corrected and equalized by rotation via computation cross-polar transmit and receive patterns in H (left column) and V (right column).*

The values of partial correction matrices computed from a single data collection run are presented in Figure 4.10. These are the beamsteering corrections for reflectivity in H and V (even though the latter is not used in the signal processor), as well as differential reflectivity and phase. The total of 13 data sets were collected after the last ATD antenna-panel refurbishment completed in December of 2022. Two of those collections exhibited apparent data outliers at a few beamsteering angles that, if not accounted for, adversely affected the correction matrix computations. Because of this, we devised a mechanism to detect and correct faulty data. We were not able to determine the cause of these faulty data collections and we conjectured that these may be attributed to environmental effects such as wind loading and/or multipath.

Once the regular weather data collections were started, they revealed an intermittent range-sidelobe issue, which negatively affected the ATD data fields. The problem was tracked to a noisy receiver subarray channel. The engineers attributed the increased phase noise (that negatively impacted the pulse compression algorithm) to a faulty connector on one of the Analog-to-Digital Converter (ADC) boards. The temporary solution was to turn off the noisy subarray channel; consequently, the last four beamsteering and cross-coupling bias data collections were performed with the noisy subarray deactivated.
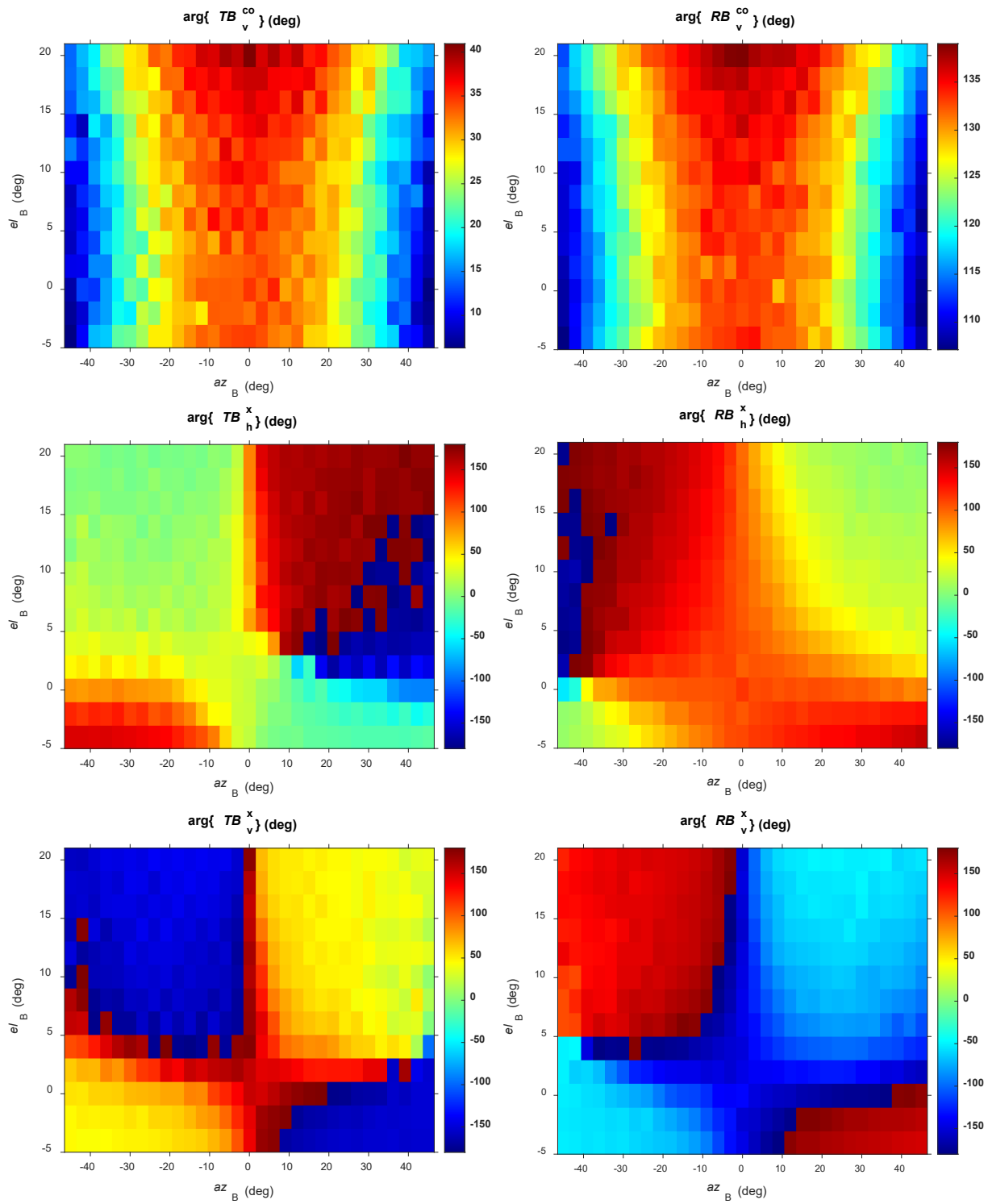
*Figure 4.18. Beam phases on transmit (left column), and receive (right column).*
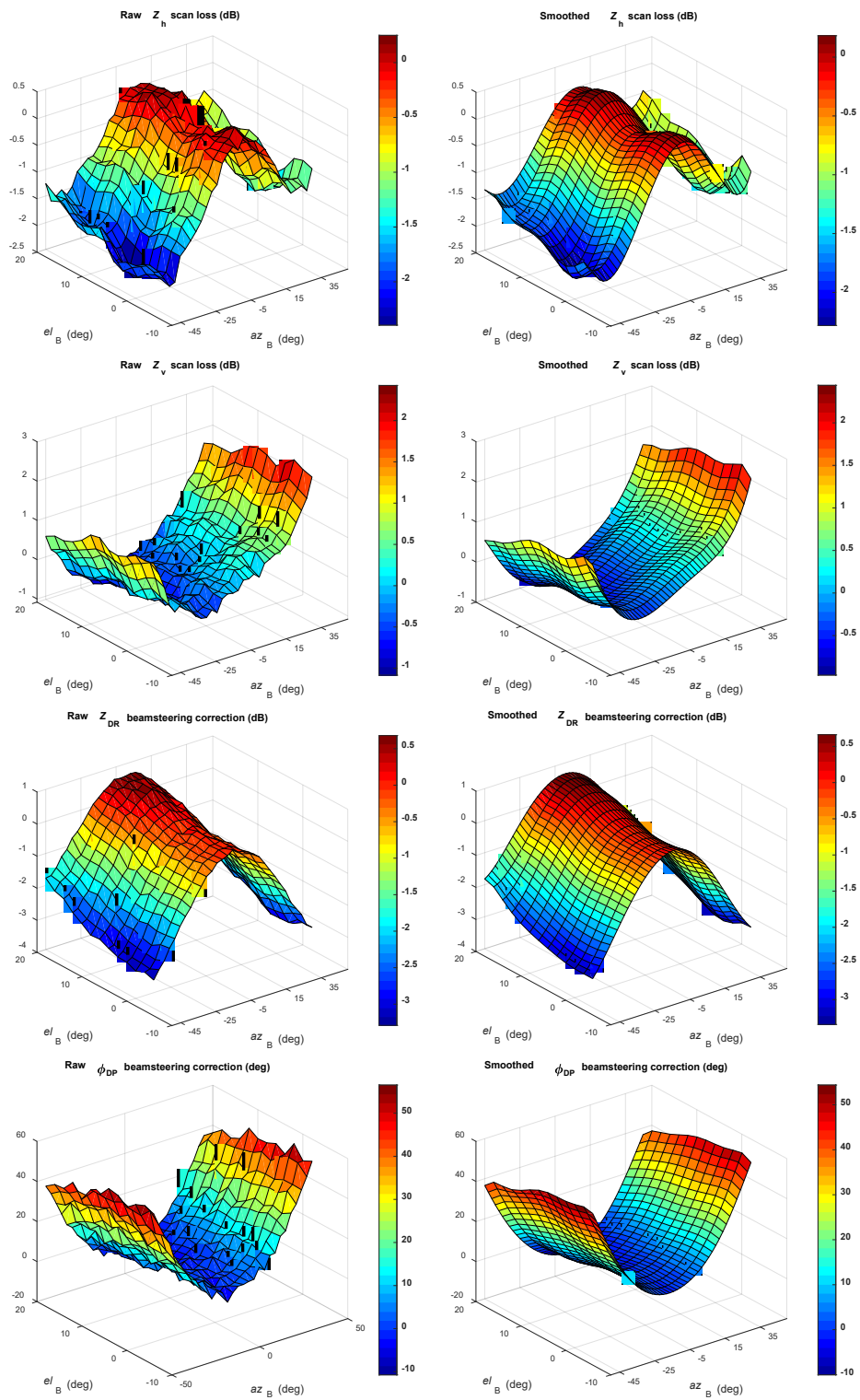
*Figure 4.19. An example of raw (left column) and smoothed (right column) copolar beamsteering corrections derived from a single calibration execution.*

The averaged correction values derived from the raw data of all 13 measurements are displayed in Figure 4.20. Figure 4.21 and Figure 4.22 present important statistics related to the measurements. In Figure 4.21, the maximum difference between any combination of two measurements (out of 13) is shown for all beamsteering angles. Figure 4.22 illustrates the maximum difference between any measurement and a fit. For Figure 4.23 and Figure 4.24, the same statistics are provided, but only for the last four measurements when the noisy subarray was deactivated. A visual comparison reveals smaller variations among these measurements, indicating that the increased noise had a negative impact on measurement stability. It is crucial to assess the variations in beamsteering correction measurements as they offer insights into the stability of beamsteering bias over time and with temperature changes. Since the execution time for beamsteering bias calibration measurements is quite lengthy, ensuring the stability of these measurements becomes particularly significant, considering that they are unlikely to be performed on a daily basis. The statistics presented in Figure 4.21 to Figure 4.24 suggest that the beamsteering biases are highly stable, and much of the observed variations (especially in Figure 4.21 and Figure 4.22) can be attributed to measurement errors.

Next, estimates of the worst case cross-coupling biases were computed, using correction matrices obtained from measurements, by first computing the second-order estimates contaminated by beamsteering and cross-coupling biases for a range of $\phi_{DP}$ values (because cross-coupling biases are particularly sensitive to $\phi_{DP}$ variations) as

$$
\begin{bmatrix}
\langle \hat{S}_h(az_B, el_B) \rangle \\
\langle \hat{S}_v(az_B, el_B) \rangle \\
\langle \hat{R}_{hv}(az_B, el_B, 0) \rangle \\
\langle \hat{R}_{hv}^*(az_B, el_B, 0) \rangle
\end{bmatrix}
= CM_{FULL}^{-1}
\begin{bmatrix}
S_h \\
S_v \\
\sqrt{S_h S_v}|\rho_{hv}|e^{j\phi_{DP}} \\
\sqrt{S_h S_v}|\rho_{hv}|e^{-j\phi_{DP}}
\end{bmatrix},
\tag{4.19}
$$

and then computing the second-order estimates contaminated only by the beamsteering biases as

$$
\begin{bmatrix}
\langle \hat{S}_h'(az_B, el_B) \rangle \\
\langle \hat{S}_v'(az_B, el_B) \rangle \\
\langle \hat{R}_{hv}'(az_B, el_B, 0) \rangle \\
\langle \hat{R}_{hv}'^*(az_B, el_B, 0) \rangle
\end{bmatrix}
= CM_{PART}^{-1}
\begin{bmatrix}
S_h \\
S_v \\
\sqrt{S_h S_v}|\rho_{hv}|e^{j\phi_{DP}} \\
\sqrt{S_h S_v}|\rho_{hv}|e^{-j\phi_{DP}}
\end{bmatrix}.
\tag{4.20}
$$

The cross-coupling biases are then produced at each beamsteering angle as

$$
\text{MAX. BIAS}_X \, Z(az_B, el_B) = MAX\{10 \log_{10}[\langle \hat{S}_h(az_B, el_B) \rangle] - 10 \log_{10}[\langle \hat{S}_h'(az_B, el_B) \rangle]\},
$$

$$\text{MAX. BIAS}_X \, Z_{\text{DR}}(az_B, el_B) = MAX\left\{10\, log_{10}\left[\frac{\langle \hat{S}_h(az_B, el_B)\rangle}{\langle \hat{S}_v(az_B, el_B)\rangle}\right] - 10\, log_{10}\left[\frac{\langle \hat{S}_h'(az_B, el_B)\rangle}{\langle \hat{S}_v'(az_B, el_B)\rangle}\right]\right\},$$

$$\text{MAX. BIAS}_X \, |\rho_{\text{hv}}(az_B, el_B)| = MAX\left\{\frac{|\langle \hat{R}_{\text{hv}}(az_B, el_B, 0)\rangle|}{\sqrt{\langle \hat{S}_h(az_B, el_B)\rangle\langle \hat{S}_v(az_B, el_B)\rangle}}\right\} - |\rho_{\text{hv}}|,$$

$$\text{MAX. BIAS}_X \, \phi_{\text{DP}}(az_B, el_B) = MAX\{arg\{\langle \hat{R}_{\text{hv}}(az_B, el_B, 0)\rangle\} - arg\{\langle \hat{R}_{\text{hv}}'(az_B, el_B, 0)\rangle\}\}, \quad (4.21)$$

where the *MAX* function operates on the vector of computed biases for $\phi_{\text{DP}}$ values that range from 0° to 360°. It should be noted though, that the cross-coupling bias assessment was conducted assuming that the ATD perfectly realizes the commanded phases on transmit. Unfortunately, this is not the case as the ATD hardware employs 6-bit phase shifting circuits resulting in the transmit phases that do not perfectly match the commanded ones. This reduces the efficacy of the pulse-to-pulse phase coding, but we have not yet determined to what extent. The results computed for $Z_{\text{DR}} = 0$ dB and $|\rho_{\text{hv}}| = 0.99$ as well as without and with pulse-to-pulse phase coding are presented in Figure 4.25. These indicate substantial reduction of cross-coupling biases for *Z*, $Z_{\text{DR}}$ and $\phi_{\text{DP}}$ measurements when phase coding is used. In the case of reflectivity, the results indicate that the cross-coupling had the potential to induce appreciable biases in the STSR (i.e., without the phase coding) mode but these biases are efficiently mitigated in the PCSTSR (i.e., with phase coding) mode. The assessment of the $Z_{\text{DR}}$ and $\phi_{\text{DP}}$ cross-coupling effects shows that significant worst-case cross-coupling biases in the STSR mode are sufficiently suppressed in the PCSTSR mode. In the case of $|\rho_{\text{hv}}|$, the assessment implies that the pulse-to-phase phase coding as currently implemented in the ATD (i.e., simple 0° and 180° shifts arranged in a block manner as suggested in Ivić 2018a) can potentially exacerbate the cross-coupling biases in $|\rho_{\text{hv}}|$ estimates. Nonetheless, research conducted so far suggests that the cross-coupling effects can be further mitigated by filtering in the spectral domain (Ivić 2018a, Ivić 2022), and/or by tilting the antenna (Ivić 2023). The former approach is very effective in reducing the cross-coupling bias in $|\rho_{\text{hv}}|$ estimates, particularly at upper elevations where the contamination from ground clutter is not common.
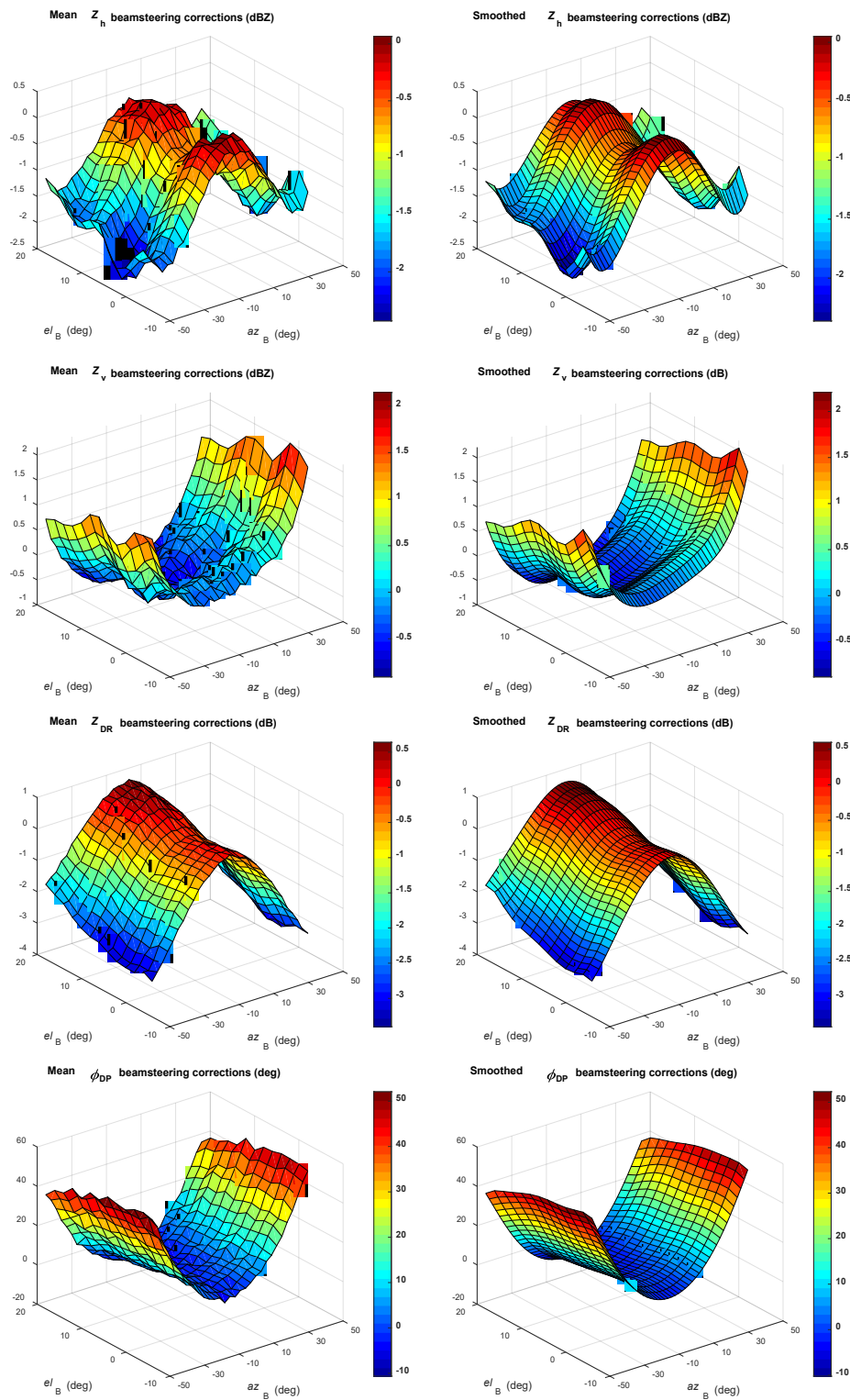
*Figure 4.20. An example of raw (left column) and smoothed (right column) copolar beamsteering corrections derived from 13 calibration executions.*
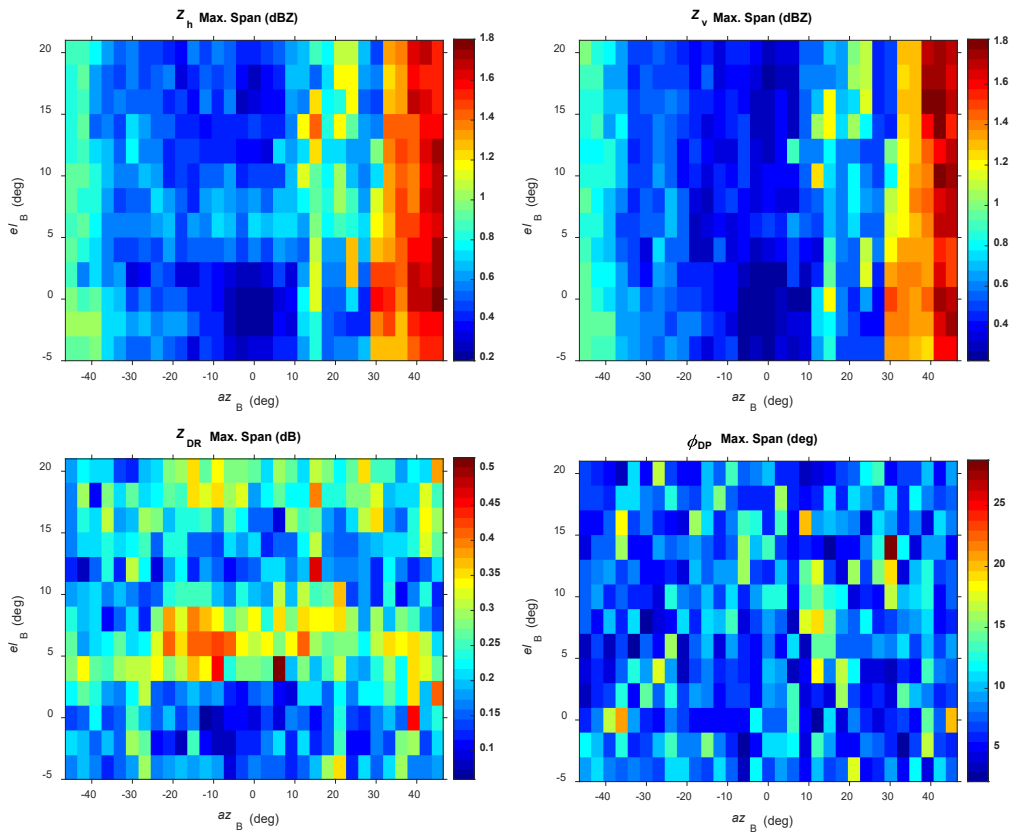
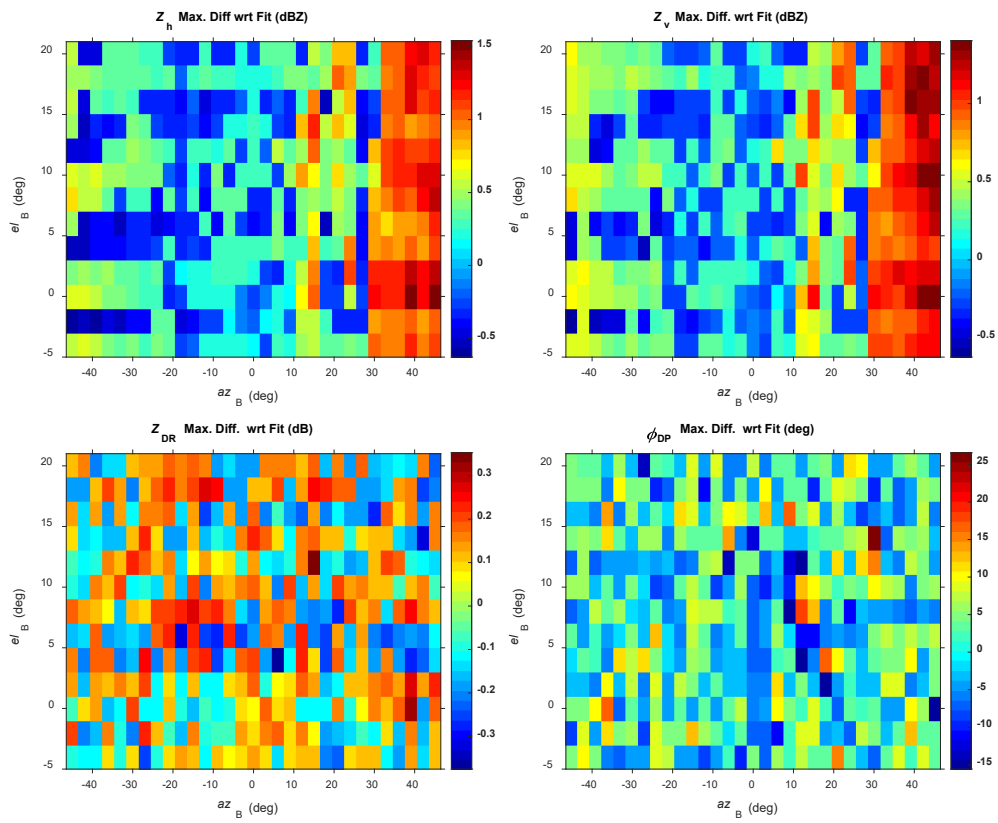*Figure 4.21. Maximum difference between any two measurements.*

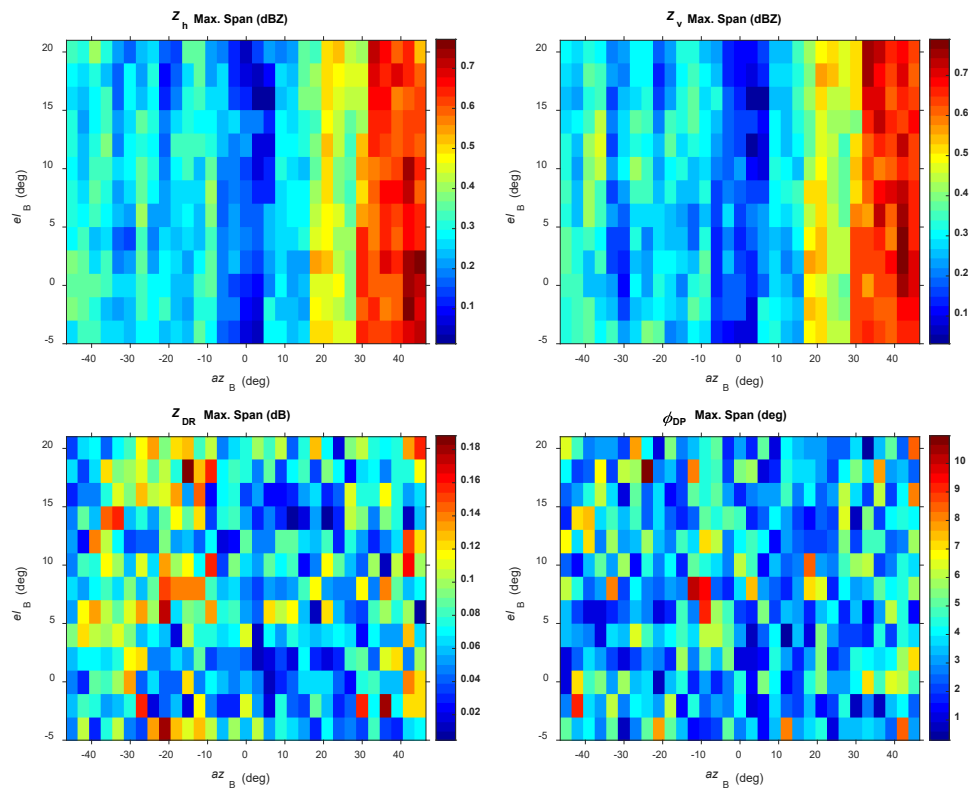*Figure 4.22. Maximum difference between any measurements and fit.*

*Figure 4.23. Maximum difference between any two measurements for collections with the noisy subarray deactivated.*
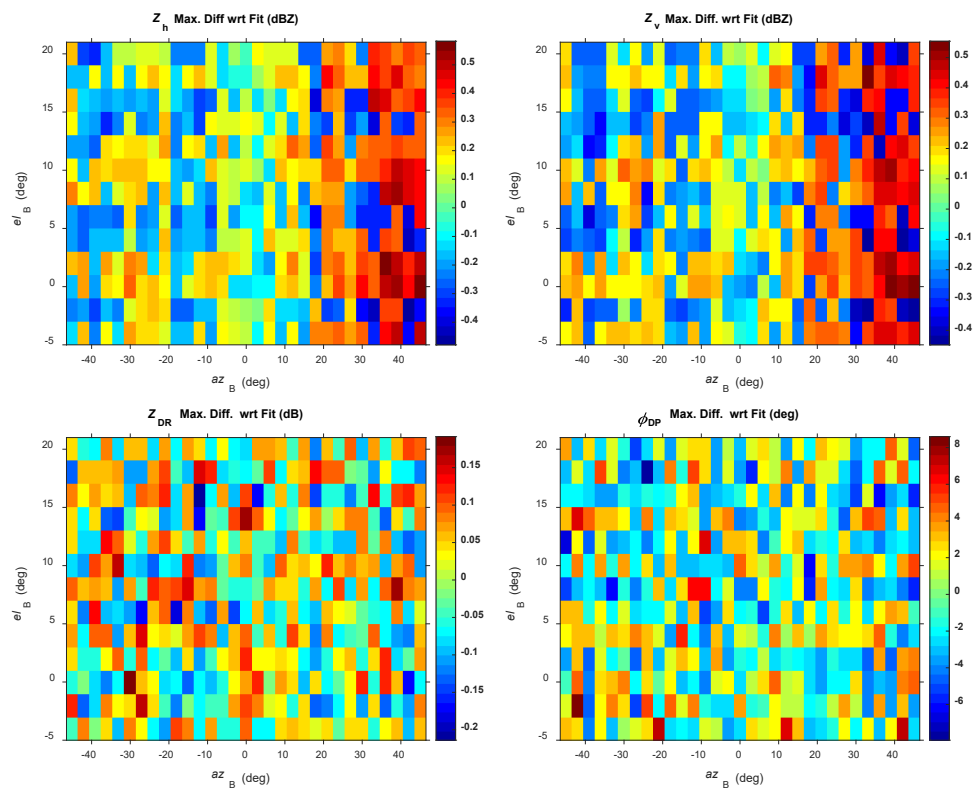
*Figure 4.24. Maximum difference between measurements and fit for collections with the noisy subarray deactivated.*
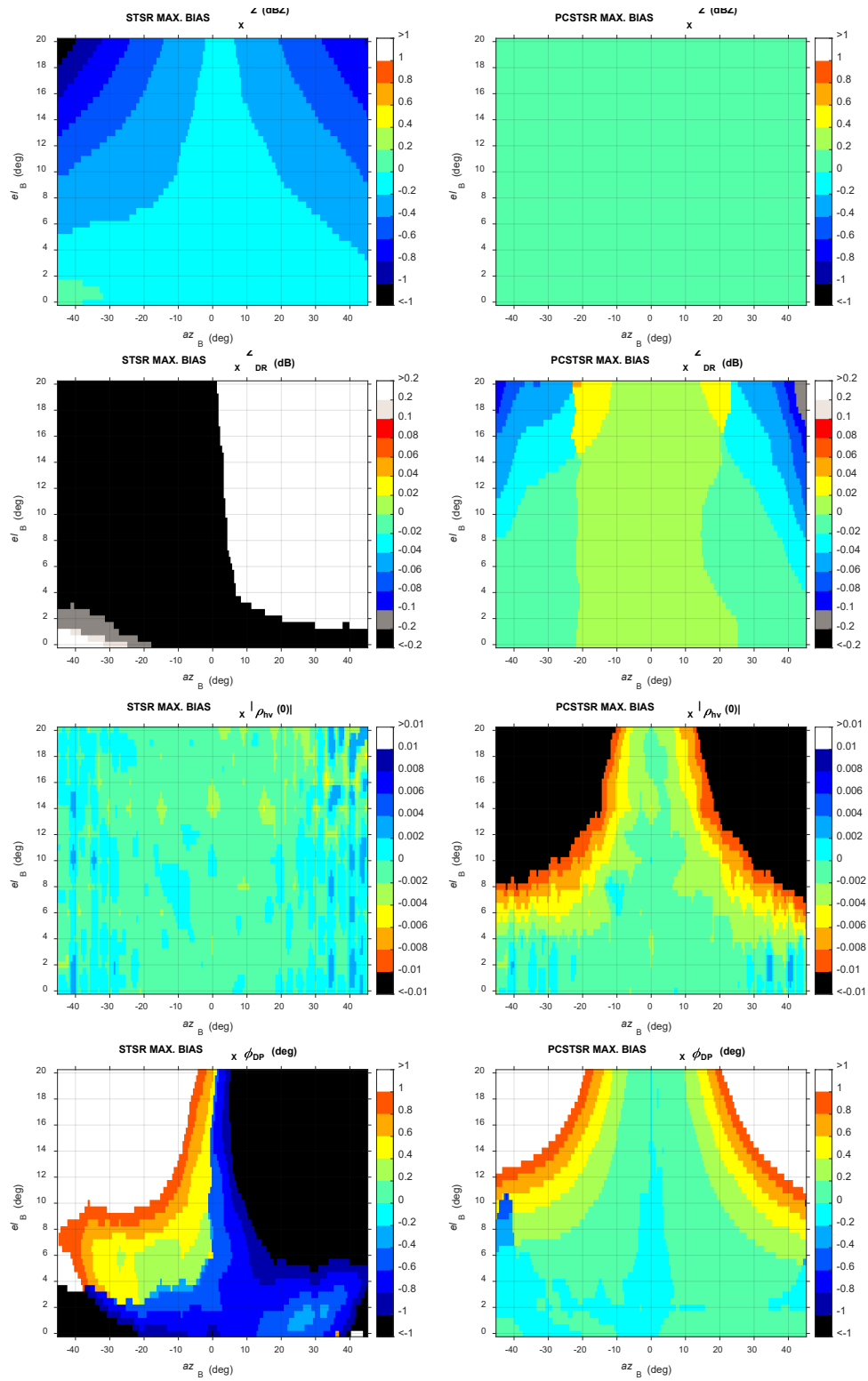
*Figure 4.25. The worst case cross-coupling biases derived from beam measurements without (left column) and with (right column) phase coding.*

## 4.3    Broadside Polarimetric Calibration (Cal 06)

The purpose of the broadside bias calibration is to produce the waveform-dependent $Z_{DR}$ bias correction (i.e., *SYS_ZDR*) and initial system $\phi_{DP}$ (i.e., *SYS_PHIDP*) bias correction values when the beam is electronically steered at a face-relative azimuth and elevation of 0°. To achieve this, the ATD antenna is mechanically aimed at the assumed FF probe location. Further, the broadside bias calibration measurements are conducted whereby the ATD transmits and the signal received by the FF probe goes through a delay line and is re-transmitted back to the ATD antenna. The signal is then processed as it would be during operations. The use of the delay line is employed to bypass the receiver protection circuits that prevent signal reception during the transmit cycle. Each measurement is derived from signals obtained by electronically scanning an area around the assumed FF probe location to capture the shapes of main H and V beams.

A model that describes this measurement is

$$
\begin{bmatrix} V_h(\alpha_n + \Delta\alpha) \\ V_v(\alpha_n + \Delta\alpha) \end{bmatrix} = C(\boldsymbol{PY}_{ATD} \times \boldsymbol{R}_{ATD})^t \times \boldsymbol{RPY}_H \times \boldsymbol{F}_H \times (\boldsymbol{RPY}_H \times \boldsymbol{F}_H)^t \times \boldsymbol{PY}_{ATD} \times \boldsymbol{T}_{ATD} \times \boldsymbol{E}_{ATD}
$$

$$
= \begin{bmatrix} R_h^{co} & R_h^x \\ R_v^x & R_v^{co} \end{bmatrix} \begin{bmatrix} H_h^{co} & -H_h^x \\ H_h^x & H_h^{co} \end{bmatrix} \begin{bmatrix} HM_{11}(\alpha_n) \\ HM_{12}(\alpha_n) \end{bmatrix} [HM_{11}(\alpha_n) \quad HM_{12}(\alpha_n)] \begin{bmatrix} H_h^{co} & H_h^x \\ -H_h^x & H_h^{co} \end{bmatrix} \begin{bmatrix} T_h^{co} & T_v^x \\ T_h^x & T_v^{co} \end{bmatrix}
$$

$$
\times \boldsymbol{E}_{ATD}
$$

$$
= \begin{bmatrix} R_h^{co} & R_h^x \\ R_v^x & R_v^{co} \end{bmatrix} \begin{bmatrix} H_h^{co} & -H_h^x \\ H_h^x & H_h^{co} \end{bmatrix} \begin{bmatrix} HM_{11}^2(\alpha_n) & HM_{11}(\alpha_n)HM_{12}(\alpha_n) \\ HM_{11}(\alpha_n)HM_{12}(\alpha_n) & HM_{12}^2(\alpha_n) \end{bmatrix} \begin{bmatrix} H_h^{co} & H_h^x \\ -H_h^x & H_h^{co} \end{bmatrix} \begin{bmatrix} T_h^{co} & T_v^x \\ T_h^x & T_v^{co} \end{bmatrix}
$$

$$
\times \boldsymbol{E}_{ATD}
$$

$$
= \begin{bmatrix} H_h^{co}R_h^{co} + H_h^x R_h^x & -H_h^x R_h^{co} + H_h^{co}R_h^x \\ H_h^x R_v^{co} + H_h^{co}R_v^x & H_h^{co}R_v^{co} - H_h^x R_v^x \end{bmatrix} \begin{bmatrix} HM_{11}^2(\alpha_n) & HM_{11}(\alpha_n)HM_{12}(\alpha_n) \\ HM_{11}(\alpha_n)HM_{12}(\alpha_n) & HM_{12}^2(\alpha_n) \end{bmatrix}
$$

$$
\begin{bmatrix} H_h^{co}T_h^{co} + H_h^x T_h^x & H_h^x T_v^{co} + H_h^{co}T_v^x \\ -H_h^x T_h^{co} + H_h^{co}T_h^x & H_h^{co}T_v^{co} - H_h^x T_v^x \end{bmatrix} \times \boldsymbol{E}_{ATD} \qquad (4.22)
$$

where $\alpha_n$ is the commanded FF probe rotation position and $\Delta\alpha$ is the unknown position offset (i.e., the difference between $\alpha_n$ and the true FF probe rotation position). If the H port is excited (i.e., $\boldsymbol{E_{ATD}} = [1\ 0]^t$), the received signal in the H/V channel is

$$
\begin{bmatrix} V_h(\alpha_n + \Delta\alpha) \\ V_v(\alpha_n + \Delta\alpha) \end{bmatrix} =
$$

$$\left[\begin{matrix}\left\{\begin{matrix}HM_{11}^2(H_h^{co}R_h^{co}+H_h^xR_h^x)(H_h^{co}T_h^{co}+H_h^xT_h^x)+HM_{12}^2(H_h^{co}R_h^x-H_h^xR_h^{co})(H_h^{co}T_h^x-H_h^xT_h^{co})+\\ HM_{11}HM_{12}[(H_h^{co}R_h^{co}+H_h^xR_h^x)(H_h^{co}T_h^x-H_h^xT_h^{co})+(H_h^{co}R_h^x-H_h^xR_h^{co})(H_h^{co}T_h^{co}+H_h^xT_h^x)]\end{matrix}\right\}\\ \left\{\begin{matrix}HM_{11}^2(H_h^xR_v^{co}+H_h^{co}R_v^x)(H_h^{co}T_h^{co}+H_h^xT_h^x)+HM_{12}^2(H_h^{co}R_v^x-H_h^xR_v^{co})(H_h^{co}T_h^x-H_h^xT_h^{co})+\\ HM_{11}HM_{12}[(H_h^xR_v^{co}+H_h^{co}R_v^x)(H_h^{co}T_h^x-H_h^xT_h^{co})+(H_h^{co}R_v^{co}-H_h^xR_v^x)(H_h^{co}T_h^{co}+H_h^xT_h^x)]\end{matrix}\right\}\end{matrix}\right] \quad (4.23)$$

If the V port is excited (i.e., $\mathbf{E_{ATD}} = [0\ 1]^t$), the received signal in the H/V channel is

$$\begin{bmatrix}V_h(\alpha_n+\Delta\alpha)\\ V_v(\alpha_n+\Delta\alpha)\end{bmatrix}=$$

$$\left[\begin{matrix}\left\{\begin{matrix}HM_{11}^2(H_h^{co}R_h^{co}+H_h^xR_h^x)(H_h^xT_v^{co}+H_h^{co}T_v^x)+HM_{12}^2(-H_h^xR_h^{co}+H_h^{co}R_h^x)(H_h^{co}T_v^{co}-H_h^xT_v^x)+\\ HM_{11}HM_{12}[(-H_h^xR_h^{co}+H_h^{co}R_h^x)(H_h^xT_v^{co}+H_h^{co}T_v^x)+(H_h^{co}R_h^{co}+H_h^xR_h^x)(H_h^{co}T_v^{co}-H_h^xT_v^x)]\end{matrix}\right\}\\ \left\{\begin{matrix}HM_{12}^2(H_h^{co}R_v^{co}-H_h^xR_v^x)(H_h^{co}T_v^{co}-H_h^xT_v^x)+HM_{11}^2(H_h^xR_v^{co}+H_h^{co}R_v^x)(H_h^xT_v^{co}+H_h^{co}T_v^x)+\\ HM_{11}HM_{12}[(H_h^{co}R_v^{co}-H_h^xR_v^x)(H_h^xT_v^{co}+H_h^{co}T_v^x)+(H_h^xR_v^{co}+H_h^{co}R_v^x)(H_h^{co}T_v^{co}-H_h^xT_v^x)]\end{matrix}\right\}\end{matrix}\right] \quad (4.24)$$

For this measurement, the ATD antenna is positioned so that the broadside points directly towards the FF probe. In such a case, we can assume the following

$$\mathbf{RPY_H^t} \times \mathbf{PY_{ATD}} \approx \begin{bmatrix}HM_{11}(\alpha_n) & HM_{12}(\alpha_n)\\ -HM_{12}(\alpha_n) & HM_{11}(\alpha_n)\end{bmatrix},$$

$$\approx \begin{bmatrix}cos\,\alpha & -sin\,\alpha\\ sin\,\alpha & cos\,\alpha\end{bmatrix}, \quad (4.25)$$

In which case expression (4.23) becomes

$$\begin{bmatrix}V_h(\alpha_n+\Delta\alpha)\\ V_v(\alpha_n+\Delta\alpha)\end{bmatrix}\approx\left[\begin{matrix}\left\{\begin{matrix}cos^2(\alpha_n+\Delta\alpha)\,(H_h^{co}R_h^{co}+H_h^xR_h^x)(H_h^{co}T_h^{co}+H_h^xT_h^x)+\\ +sin^2(\alpha_n+\Delta\alpha)(H_h^{co}R_h^x-H_h^xR_h^{co})(H_h^{co}T_h^x-H_h^xT_h^{co})\\ cos(\alpha_n+\Delta\alpha)\,sin(\alpha_n+\Delta\alpha)\begin{bmatrix}(H_h^{co}R_h^{co}+H_h^xR_h^x)(H_h^{co}T_h^x-H_h^xT_h^{co})+\\ (H_h^{co}R_h^x-H_h^xR_h^{co})(H_h^{co}T_h^{co}+H_h^xT_h^x)\end{bmatrix}\end{matrix}\right\}\\ \left\{\begin{matrix}cos^2(\alpha_n+\Delta\alpha)\,(H_h^xR_v^{co}+H_h^{co}R_v^x)(H_h^{co}T_h^{co}+H_h^xT_h^x)+\\ +sin^2(\alpha_n+\Delta\alpha)(H_h^{co}R_v^{co}-H_h^xR_v^x)(H_h^{co}T_h^x-H_h^xT_h^{co})\\ cos(\alpha_n+\Delta\alpha)\,sin(\alpha_n+\Delta\alpha)\begin{bmatrix}(H_h^xR_v^{co}+H_h^{co}R_v^x)(H_h^{co}T_h^x-H_h^xT_h^{co})+\\ (H_h^{co}R_v^{co}-H_h^xR_v^x)(H_h^{co}T_h^{co}+H_h^xT_h^x)\end{bmatrix}\end{matrix}\right\}\end{matrix}\right] \quad (4.26)$$

Note that the rotation mechanism that the FF probe is attached to is very precise in the sense that, if the probe is commanded to two rotation positions, it is capable of precisely realizing the difference between those positions (i.e., if the offset at the first position is $\Delta\alpha$ it remains the same at the second position). Similarly, the expression (4.24) is

$$\begin{bmatrix} V_h(\alpha_n + \Delta\alpha) \\ V_v(\alpha_n + \Delta\alpha) \end{bmatrix} = \left[ \begin{matrix} \left\{ \begin{matrix} \cos^2(\alpha_n + \Delta\alpha)\,(H_h^{co}R_h^{co} + H_h^x R_h^x)(H_h^x T_v^{co} + H_h^{co}T_v^x) + \\ +\sin^2(\alpha_n + \Delta\alpha)(H_h^{co}R_h^x - H_h^x R_h^{co})(H_h^{co}T_v^{co} - H_h^x T_v^x) \\ \cos(\alpha_n + \Delta\alpha)\sin(\alpha_n + \Delta\alpha) \begin{bmatrix} (H_h^{co}R_h^x - H_h^x R_h^{co})(H_h^x T_v^{co} + H_h^{co}T_v^x) + \\ (H_h^{co}R_h^{co} + H_h^x R_h^x)(H_h^{co}T_v^{co} - H_h^x T_v^x) \end{bmatrix} \end{matrix} \right\} \\ +\left\{ \begin{matrix} \sin^2(\alpha_n + \Delta\alpha)(H_h^{co}R_v^{co} - H_h^x R_v^x)(H_h^{co}T_v^{co} - H_h^x T_v^x) + \\ \cos^2(\alpha_n + \Delta\alpha)\,(H_h^x R_v^{co} + H_h^{co}R_v^x)(H_h^x T_v^{co} + H_h^{co}T_v^x) \\ \cos(\alpha_n + \Delta\alpha)\sin(\alpha_n + \Delta\alpha) \begin{bmatrix} (H_h^{co}R_v^{co} - H_h^x R_v^x)(H_h^x T_v^{co} + H_h^{co}T_v^x) + \\ (H_h^x R_v^{co} + H_h^{co}R_v^x)(H_h^{co}T_v^{co} - H_h^x T_v^x) \end{bmatrix} \end{matrix} \right\} \end{matrix} \right] \quad (4.27)$$

Neglecting the effects of cross-polar patterns, the received signal in the H channel (as the H transmit port is excited) is approximately

$$V_h(\alpha_n + \Delta\alpha) \approx (H_h^{co})^2 R_h^{co} T_h^{co} \cos^2(\alpha_n + \Delta\alpha),$$

$$\approx (H_h^{co})^2 R_h^{co} T_h^{co} \frac{1 + \cos(2\alpha_n + 2\Delta\alpha)}{2},$$

$$\approx (H_h^{co})^2 R_h^{co} T_h^{co} \frac{1 + \cos(2\alpha_n) - 2\Delta\alpha \sin(2\alpha_n)}{2}, \quad (4.28)$$

where the last result is obtained via expansion in Taylor series. Similarly, the received signal in the V channel (as the V transmit port is excited) is approximately

$$V_v(\alpha_n + \Delta\alpha) \approx (H_h^{co})^2 R_v^{co} T_v^{co} \sin^2(\alpha_n + \Delta\alpha),$$

$$\approx (H_h^{co})^2 R_v^{co} T_v^{co} \frac{1 - \cos(2\alpha_n + 2\Delta\alpha)}{2},$$

$$\approx (H_h^{co})^2 R_v^{co} T_v^{co} \frac{1 - \cos(2\alpha_n) + 2\Delta\alpha \sin(2\alpha_n)}{2}. \quad (4.29)$$

Next, we shall analyze measurements for two horn positions of $\alpha_1 = 45°$ and $\alpha_2 = -45°$. These yield

$$V_h(45° + \Delta\alpha) \approx (H_h^{co})^2 R_h^{co} T_h^{co} \left( \frac{1}{2} - \Delta\alpha \right),$$

$$V_h(-45° + \Delta\alpha) \approx (H_h^{co})^2 R_h^{co} T_h^{co} \left( \frac{1}{2} + \Delta\alpha \right),$$

$$V_v(45° + \Delta\alpha) \approx (H_h^{co})^2 R_v^{co} T_v^{co} \left( \frac{1}{2} + \Delta\alpha \right),$$

$$V_v(-45° + \Delta\alpha) \approx (H_h^{co})^2 R_v^{co} T_v^{co} \left( \frac{1}{2} - \Delta\alpha \right). \quad (4.30)$$

By summing the two measurements in the H and V channels as

$$V_h(45° + \Delta\alpha) + V_h(-45° + \Delta\alpha) \approx (H_h^{co})^2 R_h^{co} T_h^{co},$$

$$V_v(45° + \Delta\alpha) + V_v(-45° + \Delta\alpha) \approx (H_h^{co})^2 R_v^{co} T_v^{co}. \tag{4.31}$$

the $\Delta\alpha$ effects on measurements can be cancelled (if the effects of cross-polar patterns are sufficiently small). Then, given that the signals are collected at multiple electronic steering angles [denoted as $(\theta_n, \phi_n)$] the corrections are computed as

$$SYS\_ZDR = 10 \log_{10}\left(\frac{\left|\sum_{\theta_n}\sum_{\phi_n}[V_h(45° + \Delta\alpha, \theta_n, \phi_n) + V_h(-45° + \Delta\alpha, \theta_n, \phi_n)]I(\theta_n, \phi_n)\right|^2}{\left|\sum_{\theta_n}\sum_{\phi_n}[V_v(45° + \Delta\alpha, \theta_n, \phi_n) + V_v(-45° + \Delta\alpha, \theta_n, \phi_n)]I(\theta_n, \phi_n)\right|^2}\right),$$

$$SYS\_PHIDP = arg\begin{Bmatrix}\{\sum_{\theta_n}\sum_{\phi_n}[V_h(45° + \Delta\alpha, \theta_n, \phi_n) + V_h(-45° + \Delta\alpha, \theta_n, \phi_n)]I(\theta_n, \phi_n)\}^* \times \\ \{\sum_{\theta_n}\sum_{\phi_n}[V_v(45° + \Delta\alpha, \theta_n, \phi_n) + V_v(-45° + \Delta\alpha, \theta_n, \phi_n)]I(\theta_n, \phi_n)\}\end{Bmatrix}. \tag{4.32}$$

where $I(\theta_n, \phi_n)$ serves the same purpose as in (4.18).

An example of signals measured for pulse lengths from 30 μs to 79 μs as part of the broadside polarimetric calibration is presented in Figure 4.26. Note that the measurements are set 3 μs apart to shorten the execution. The middle left panel in Figure 4.26 shows that, in the case of a long pulse, the magnitudes of the measured signals increase in a linear fashion proportional to the pulse length. In the case of the short pulse (middle left panel), the magnitudes appear to exhibit slight linear decrease as the length of the long pulse increases. Further, due to measurement errors that are exacerbated by wind loading (i.e., the wind introduces FF probe motion during measurements), the raw correction values exhibit erratic patterns as demonstrated in Figure 4.27. To mitigate the effects of measurement errors, the magnitudes and phases are fitted with polynomials of first and third degree. This is also convenient because the fit provides correction values for pulse lengths with 1 μs resolution. An example of results for a single data collection are shown in Figure 4.27.

Application of *SYS_PHIDP* produces visually satisfactory data as verified by meteorologists during multiple data collections. Differential reflectivity fields, however, appear to exhibit a consistent bias of about -0.5 dB after correction using *SYS_ZDR*. We are still investigating the cause of this bias.
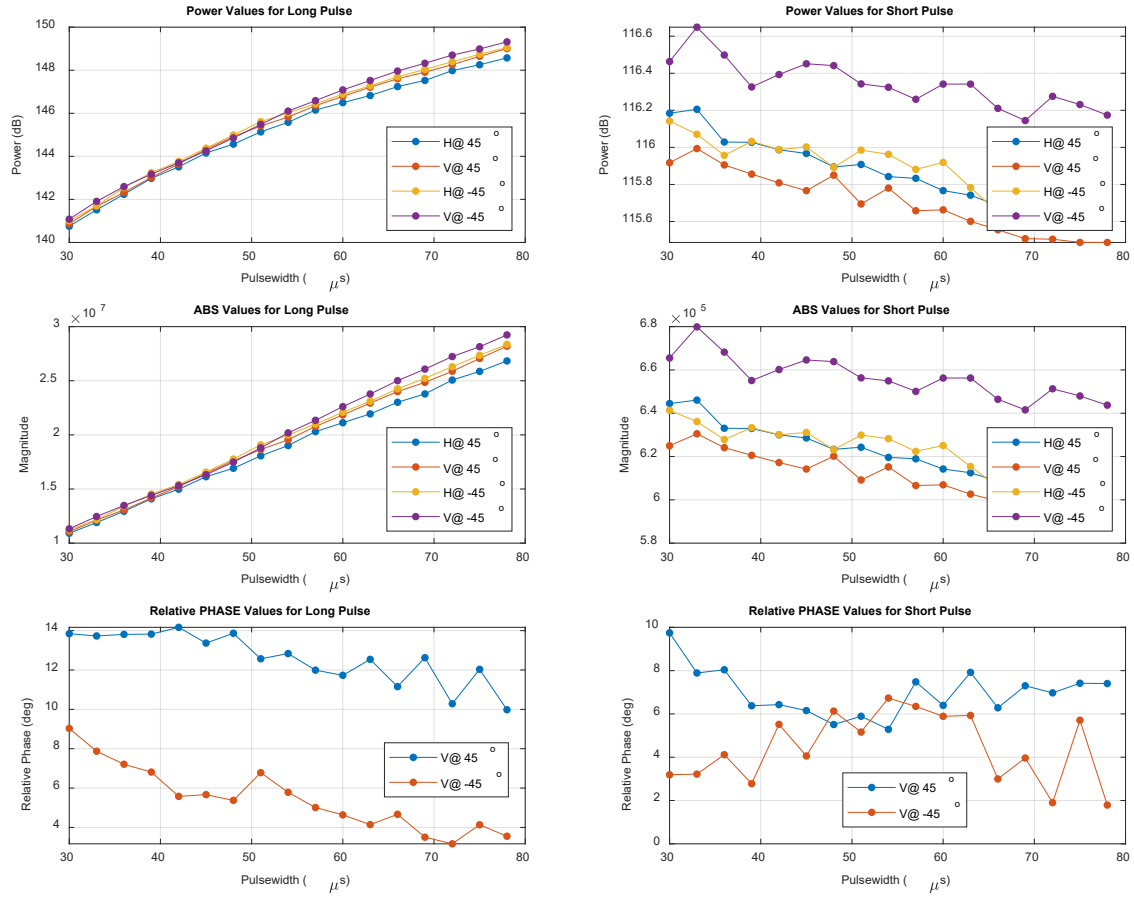
*Figure 4.26. An example of long pulse (left column) and short pulse (right column) signal products.*
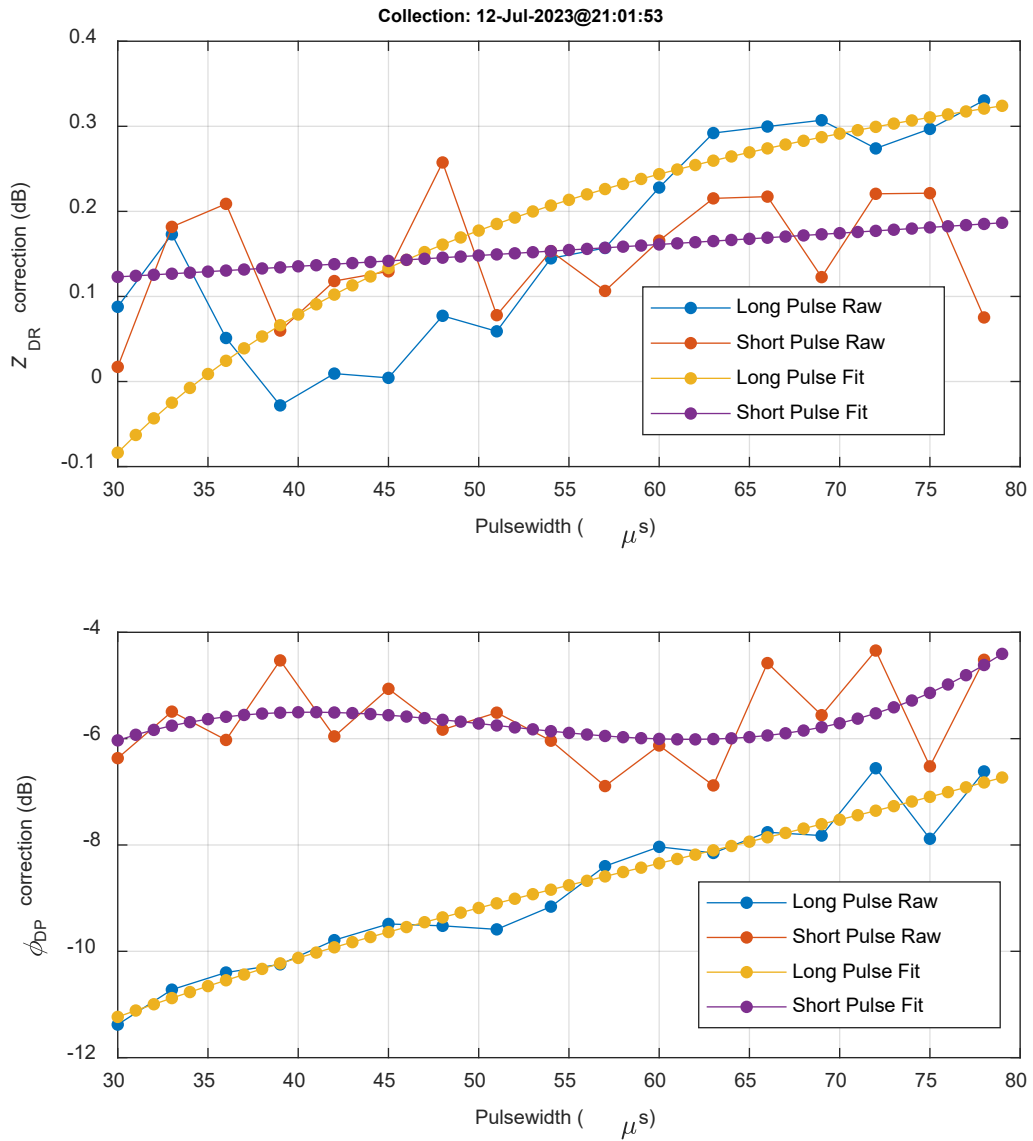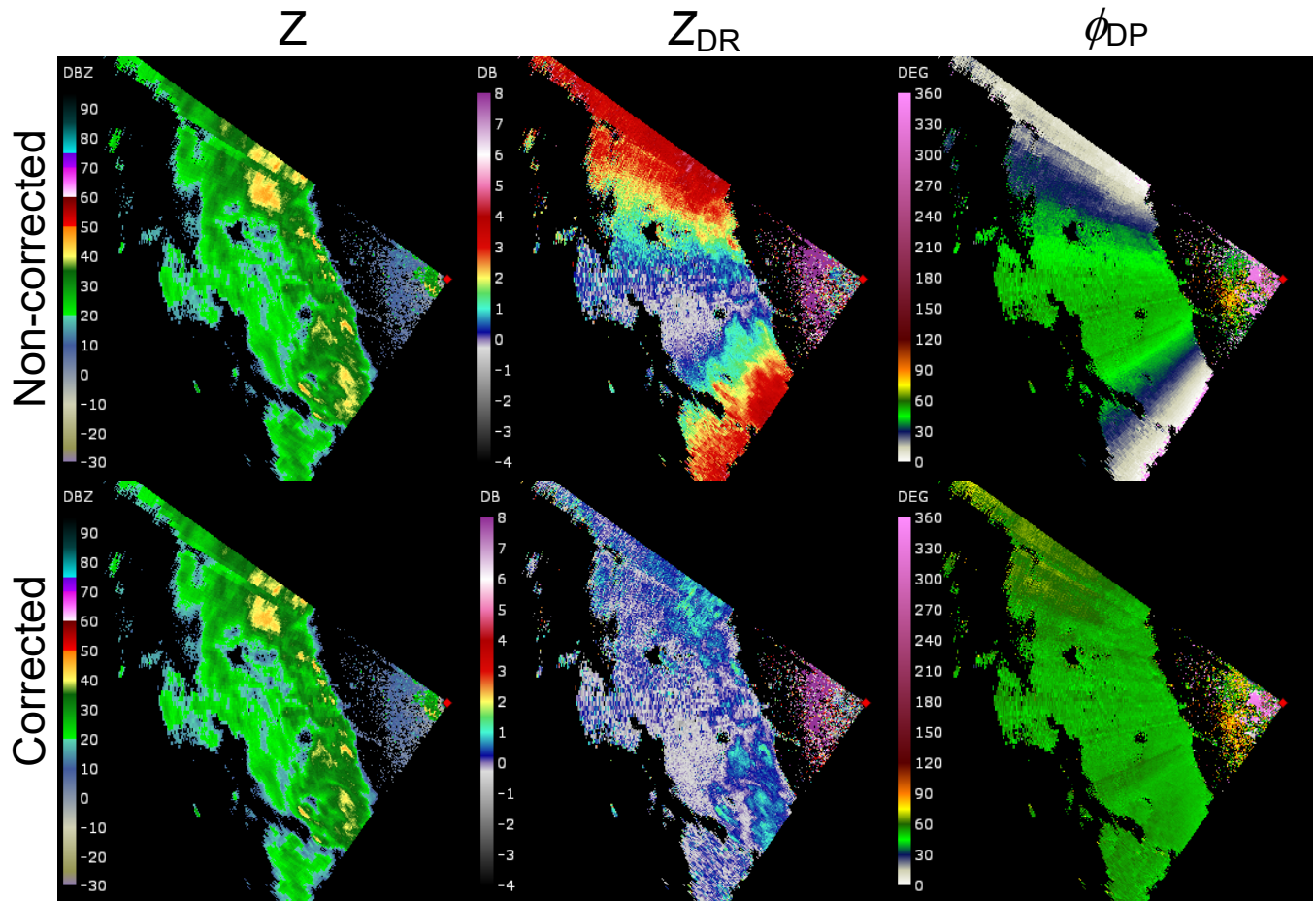
*Figure 4.27. Differential reflectivity (upper panel), and differential phase (bottom panel) correction values.*

# 5. Performance of Polarimetric Calibration

In this section, an analysis of the performance of the beamsteering bias calibration is presented. An example of the non-corrected vs. corrected data (i.e., before and after beamsteering bias correction application) is presented in Figure 5.1. In the non-corrected data, the system-induced bias effects are the most visible towards the edges of each scan sector.



*Figure 5.1. Non-corrected (top panels) and corrected (bottom panels) fields of reflectivity, differential reflectivity and differential phase.*

The effectiveness of the beamsteering corrections can be quantified via the so-called self-consistency test. The self-consistency test utilizes data derived from a sequence of sector scans acquired for different mechanical positions of the antenna so that polarimetric-variable estimates from the common sector between consecutive scans are generated for the same hydrometeors but with varying electronic beamsteering angles. Consequently, agreement in the data between consecutive scans confirms the

effectiveness of the beamsteering polarimetric calibration. The test is designed to collect 90° azimuthal sectors for pedestal azimuthal positions $\Delta az_{ant}$ apart. For instance, if three consecutive scans are to be collected with pedestal at azimuths $az_{ant}+\Delta az_{ant}$, $az_{ant}$, $az_{ant}-\Delta az_{ant}$, and weather echoes span azimuths $az_{ant}\pm(45°+30°)$, then the self-consistency data sets can be collected with $\Delta az_{ant}$ set to $\pm10°$, $\pm20°$, and $\pm30°$. Data in the overlapping sectors from the three scans is then used to compute the differences between the reflectivity, differential reflectivity and differential phase estimates associated with collocated volumes illuminated using different electronic steering. Ideally, if the beamsteering correction is accurate, these differences should be very small since storms should not change significantly within the time needed to collect the self-consistency test data, and the estimate errors are significantly reduced by using relatively long dwell times and range-oversampling processing.

Multiple self-consistency data sets were collected on May 25, 2023 for the weather system shown in Figure 5.1 and for $\Delta az_{ant}$ values of 10°, 20°, and 30° at electronic elevations of 0.5°, 0.8°, and 1.3°. To minimize the estimation errors, a large amount of data was acquired (a total of ~500 GB). The estimated differences for the reflectivity, differential reflectivity, and phase for 0.5° elevation are presented in Figure 5.2 ($\Delta az_{ant}$ = 10°), Figure 5.3 ($\Delta az_{ant}$ = 20°), and Figure 5.4 ($\Delta az_{ant}$ = 30°). The same is presented in Figure 5.5 ($\Delta az_{ant}$ = 10°), Figure 5.6 ($\Delta az_{ant}$ = 20°), and Figure 5.7 ($\Delta az_{ant}$ = 30°) for elevation of 1.3°. Note that the results for 0.8° are omitted for brevity. The results indicate that the majority of the estimated differences are within the Radar Functional Requirements (RFR) limits but exhibit systematic fluctuations (note that the random fluctuations are expected due to stochastic nature of data from which the differences are produced). Short of the errors in the beamsteering bias corrections, we conjecture that the systematic fluctuations might be caused by non-negligible evolution of storms and/or sidelobe contamination. To verify whether the systematic fluctuations in data differences are caused by the errors in the beamsteering bias corrections, another self-consistency data set would need to be collected. If the self-consistency test results from such data exhibited similar behavior as shown in Figs. 5.2 – 5.7, that would suggest imperfect beamsteering bias corrections. For completeness, the estimated differences between the correlation coefficient estimates are presented in Figure 5.8 even though the beamsteering bias corrections are not applied to this product (as it is not affected by the copolar biases). These are "uneventful" and confirm that the correlation coefficient estimates are not affected by electronic beamsteering at investigated elevations.
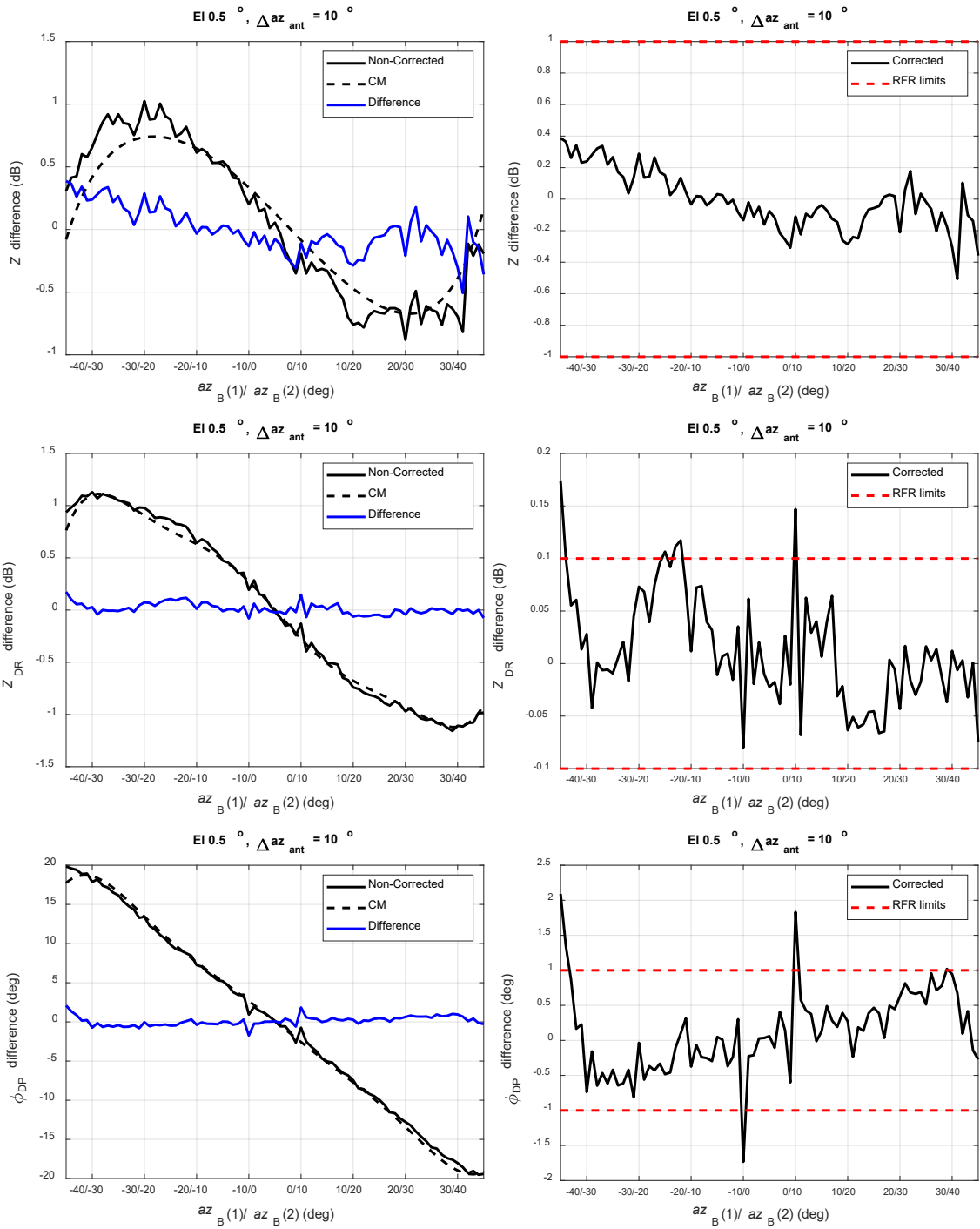
*Figure 5.2. Range-averaged differences between non-corrected returns using different electronic beamsteering (solid lines) for $\Delta az_{ant} = 10°$ at $0.5°$ elevation (left panels). The differences predicted by the calibration matrix (CM) are shown in dashed lines for reference. Differences between the two are given in solid blue lines. Estimated differences between corrected returns are presented in the right column.*
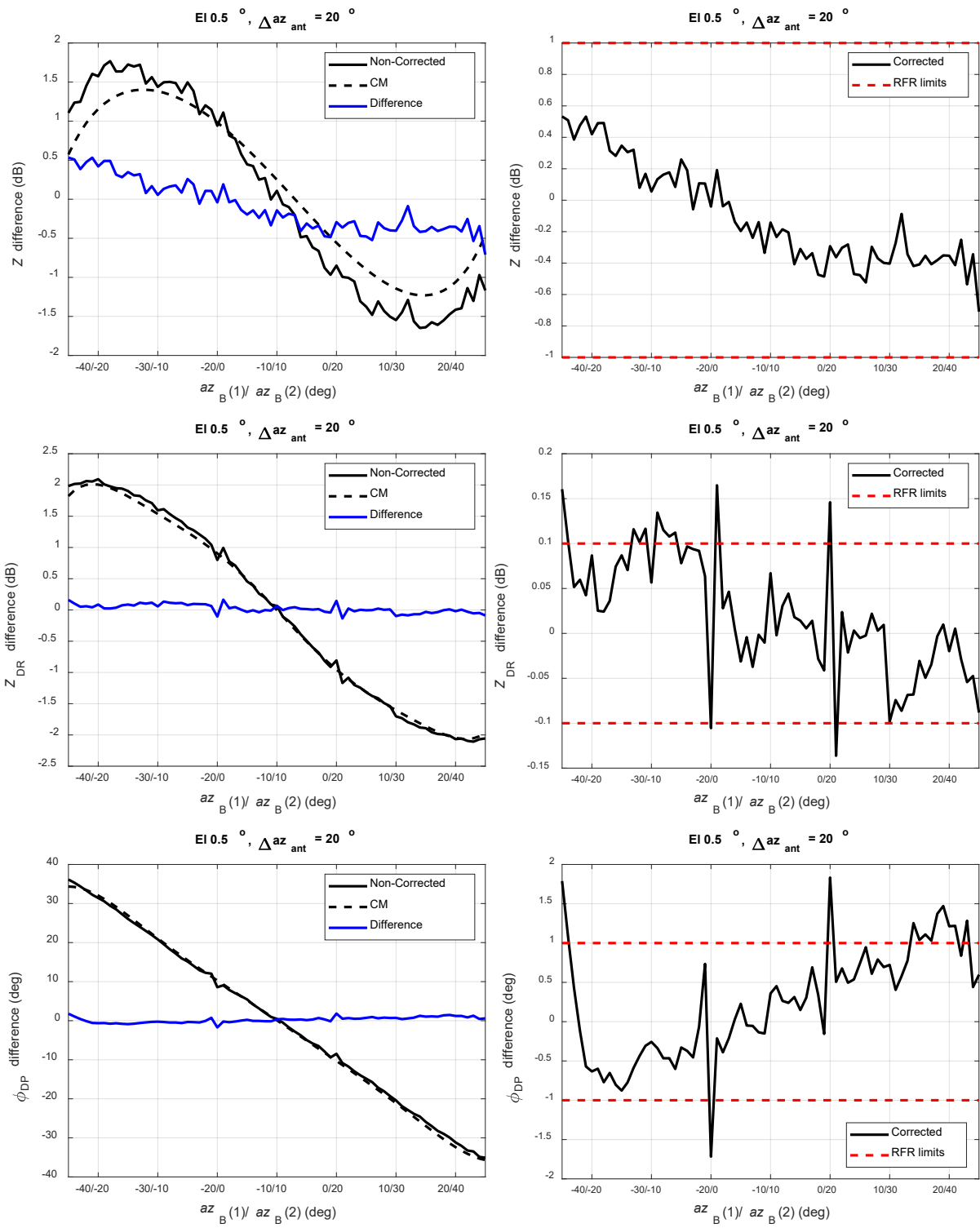
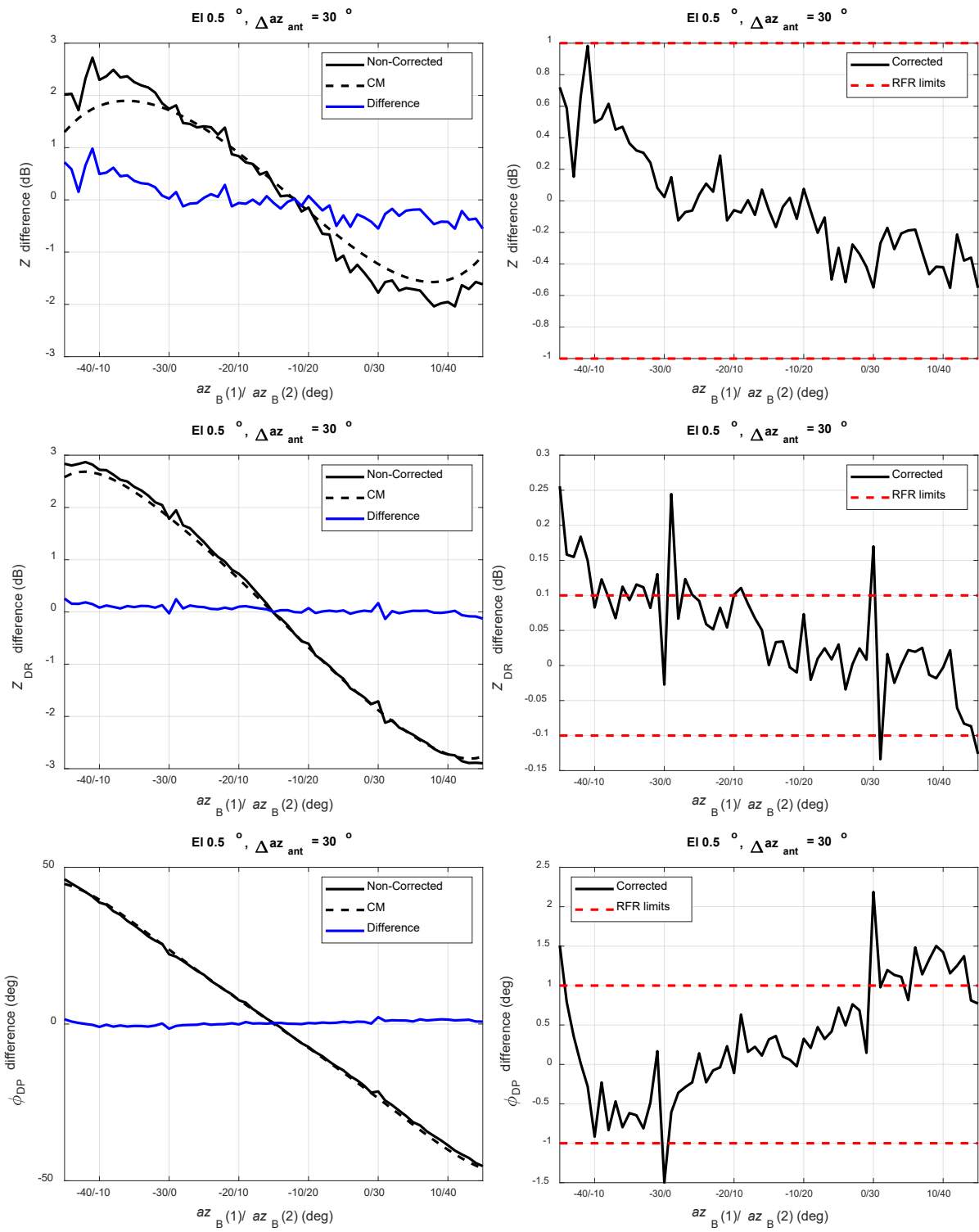63

*Figure 5.3. Same as Figure 5.2 but for Δaz_ant = 20°.*

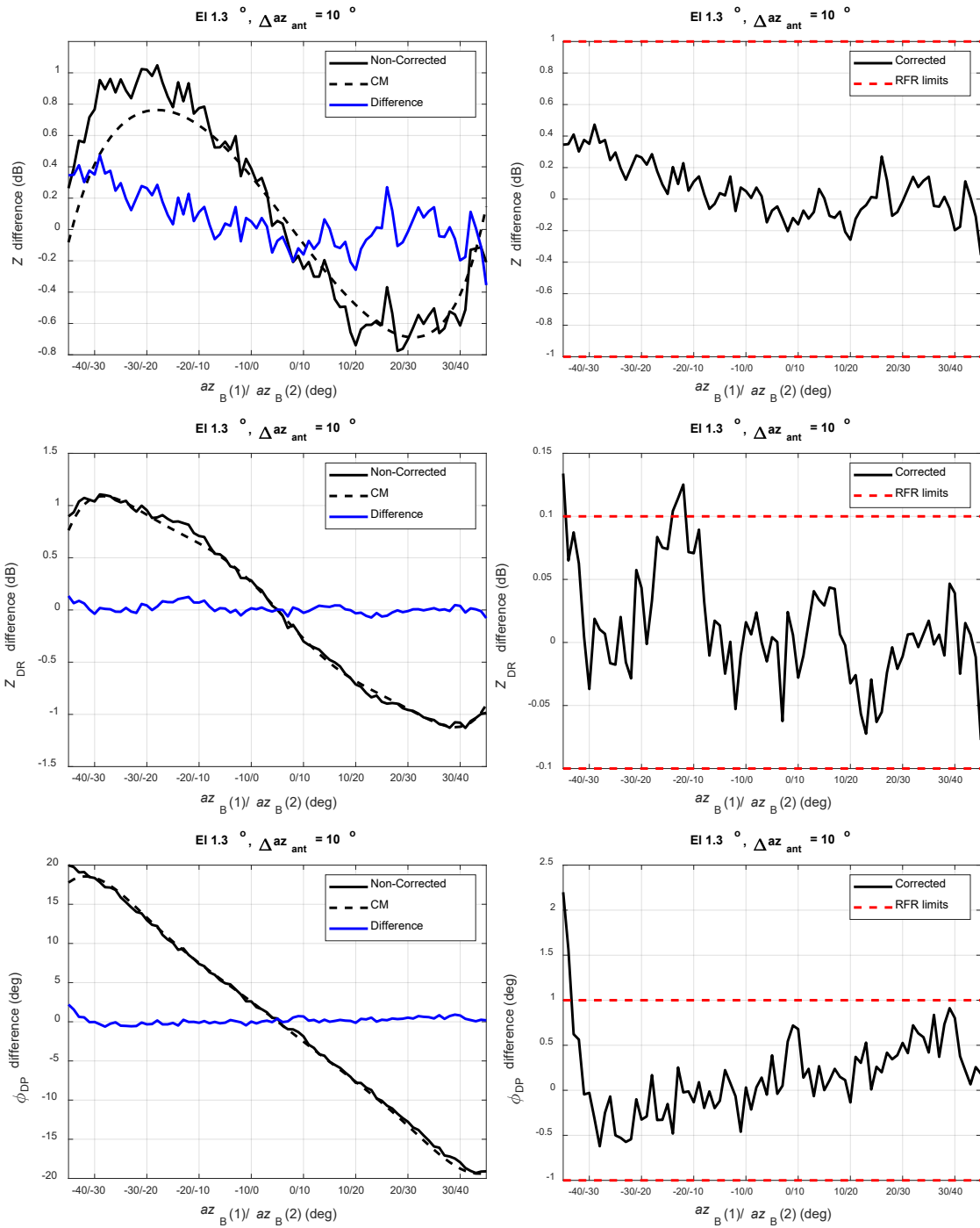*Figure 5.4. Same as Figure 5.2 but for $\Delta az_{ant} = 30°$.*

*Figure 5.5. Range-averaged differences between non-corrected returns using different electronic beamsteering (solid lines) for Δaz$_{ant}$ = 10° at 1.3° elevation (left panels). The differences predicted by the calibration matrix (CM) are shown in dashed lines for reference. Differences between the two are given in solid blue lines. Estimated differences between corrected returns are presented in the right column.*
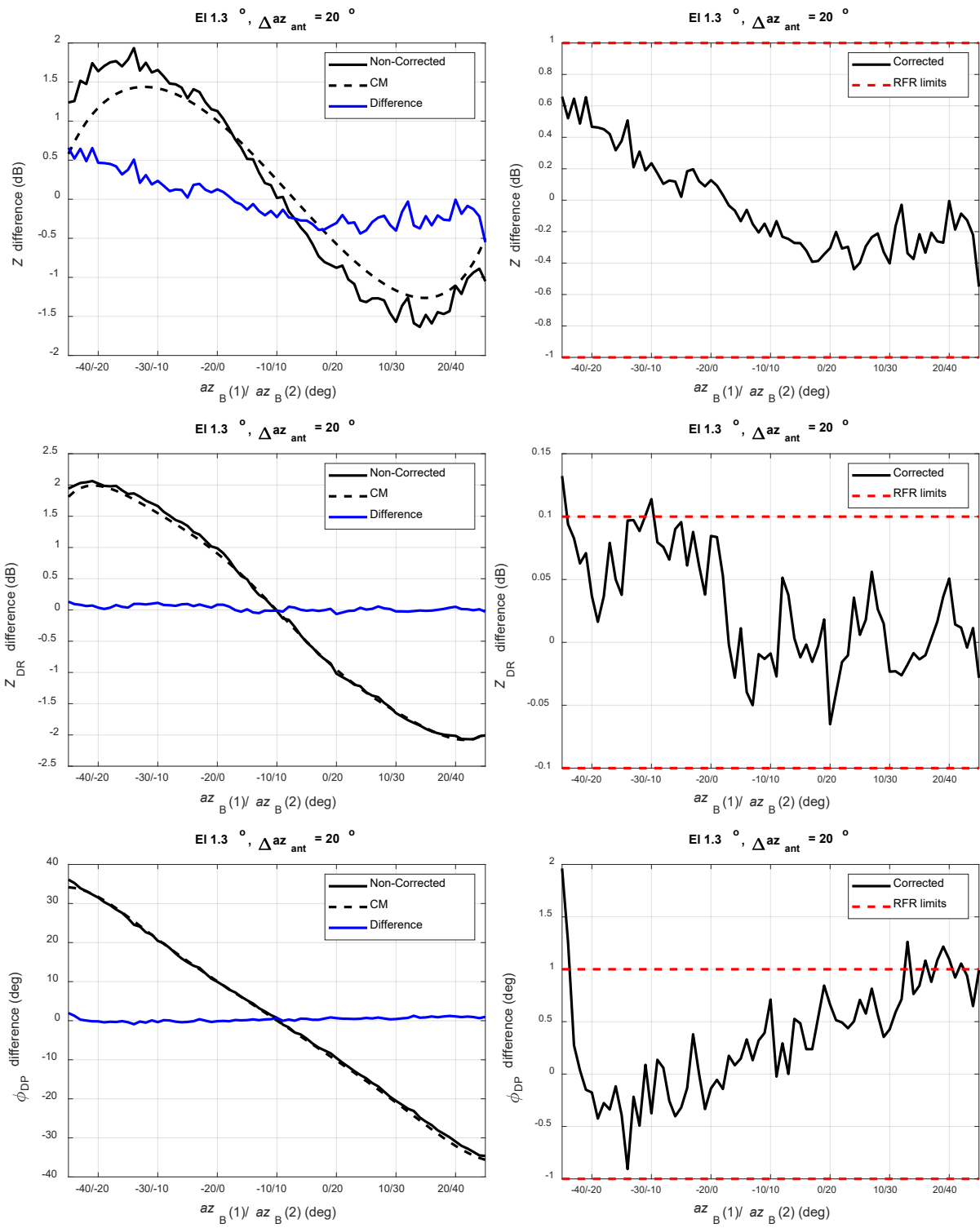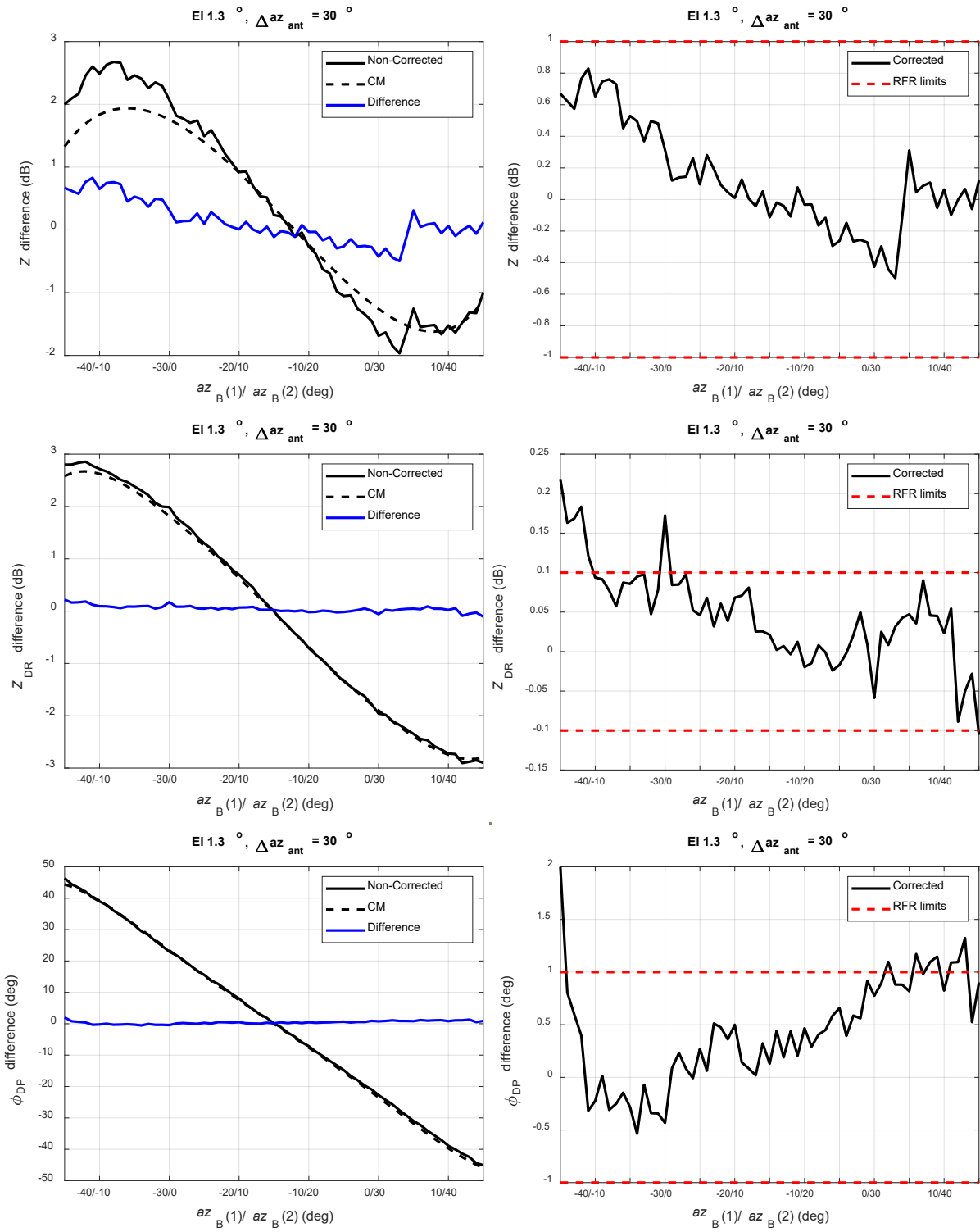
*Figure 5.6. Same as Figure 5.5 but for Δaz_ant = 20°.*

*Figure 5.7. Same as Figure 5.5 but for Δaz$_{ant}$ = 30°.*

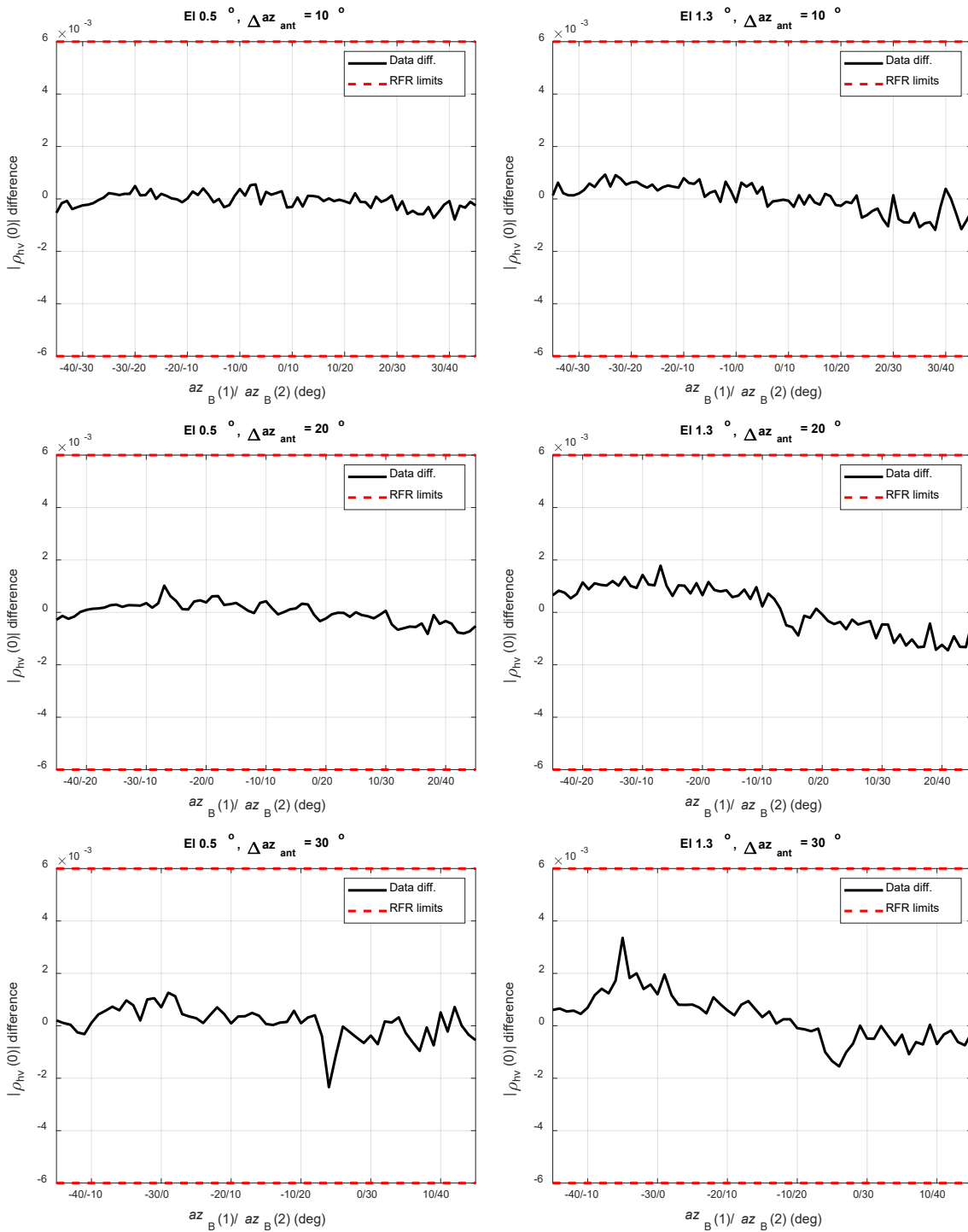*Figure 5.8. Estimated differences between correlation coefficient estimates from weather volumes at 0.5°
(left column) and 1.3° (right column) elevations illuminated by beams generated using distinct electronic
beamsteering angles for $\Delta az_{ant}$ values of 10°, 20°, and 30°.*

# 6. Outlook and Future Work

In this report, we provided an update on the ATD calibration procedures, the stability of the measurements, and their performance in terms of producing calibrated polarimetric data. Range calibration constants and SYSCALs produced by *Cal05* are stable, and the calibration procedure only takes about 90 seconds to complete. Although the results from the Spring indicate it is not necessary to run this procedure before each weather collection, its short duration allows for execution before weather collections to more closely monitor these calibration constants. Polarimetric calibration results indicate that the copolar beamsteering biases (*Cal07*) are relatively stable, which is a significant finding. They also suggest that the beamsteering bias measurement procedure, which currently takes approximately 2.5 hours, does not need to be conducted on a daily basis. Instead, it can be performed on a weekly or longer basis, reducing the frequency of this time-consuming process. However, the report highlights the importance of regularly measuring broadside corrections (*Cal06*) to keep up with any system changes. Thus, the broadside correction measurement procedure should be conducted more frequently compared to the beamsteering bias measurement.

Moving forward, we will continue to work on improving and upgrading the existing calibration procedures. This will include the upgrade to the beamsteering and cross-coupling bias calibration (*Cal07*) which currently produces corrections only up to elevations of 20°. This upgrade will involve generating corrections when the beams are steered above 20° to support scan strategies that include those elevations. Another upgrade will expand the measurements to include transmit beams with different "spoiling" factors. We also plan on conducting further research on the broadside bias calibration (*Cal06*) as it does not currently produce bias corrections with sufficient accuracy. For range and absolute RCS calibration, there will be no changes to the calibration recipe (*Cal05*), but we will continue to compare data between the ATD and a near calibrated radar to monitor for calibration stability and potential adjustments to the fixed constants used in the calibration process.

Further research will also be aimed at improving the mitigation of cross-polar coupling using pulse-to-pulse phase coding and signal-processing techniques to address existing issues such as deficient performance of ground clutter filtering. Improvements could be realized by using a different pulse-to-pulse phase coding sequence and also by understanding the source(s) of the discrepancies between the commanded phases and the phases realized by the ATD antenna hardware. Investigations will be conducted to further improve the mitigation of the cross-coupling biases by other mechanisms. This will include (but is not limited to) collecting data with a slightly tilted antenna.

To assess the accuracy of the beamsteering bias corrections, a self-consistency test was performed at lower elevations. The results indicate solid accuracy, with beamsteering biases mostly falling within desired limits. It is important to note, though, that the self-consistency test does not measure the absolute biases directly. Instead, it examines the differences in biases that arise from scanning the same weather phenomena using different beamsteering angles. Thus, the estimated differences provide the relative bias between each pair of beamsteering angles used to scan the same volumes of weather, rather than the biases relative to broadside. Therefore, the self-consistency test provides a limited assessment of polarimetric calibration performance. Nevertheless, we will continue using self-consistency tests for further evaluations of beamsteering bias corrections. Particularly, at elevations that are higher than those used for evaluations in this report (i.e., 1.3°). It is worth noting, though, that this will be a lengthy process as weather systems that are conducive to self-consistency tests are rare (e.g., widespread precipitation that fills space across a 120° azimuthal sector). Also, the self-consistency test is likely to encounter elevation limitations because the weather returns have a smaller footprint as elevation increases.

Future work in the area of polarimetric PAR calibration will involve developing more precise bias measurement procedures and continued monitoring of the stability of calibration results with the ATD. One potential approach is to utilize Bragg scattering to determine the absolute accuracies of differential reflectivity measurements. This approach could help establish a more comprehensive and precise measurement of the biases, enhancing the overall accuracy of weather observations obtained from the ATD. Additionally, we plan to include more comparisons between the data collected by the ATD and WRS-88D radars in its vicinity. The collaborative research with the Advance Radar Research Center (ARRC) on using the Unmanned Aerial Systems (UAS) to conduct polarimetric calibrations is also expected to continue as well as the development of alternative approaches that may be more suitable for a future operational implementation.

# 7.    References

Doviak, R. J., and D. S. Zrnić, 1993: Doppler radar and weather observations. San Diego: Academic Press, pp. 562.

Ivić, I.R., and R. J. Doviak, 2016: Evaluation of phase coding to mitigate differential reflectivity bias in polarimetric PAR. *IEEE Trans. Geosci. Remote Sens.*, *54*, 431–451, Available at doi:10.1109/TGRS.2015.2459047.

Ivić, I. R., 2017: Phase Code to Mitigate the Copolar Correlation Coefficient Bias in PPAR Weather Radar. *IEEE Trans. Geosci. Remote Sensing*, *GE-55(4)*, 2144-2166. Available at doi: https://doi.org/10.1109/TGRS.2016.2637720

Ivić, I. R., 2017a: An experimental evaluation of phase coding to mitigate the cross-coupling biases in PPAR. *38th International Conference on Radar Meteorology,* Chicago, IL. Available at: 10.13140/RG.2.2.28686.87362

Ivić, I. R., 2018: Options for Polarimetric Variable Measurements on the MPAR Advanced Technology Demonstrator, *IEEE Radar Conference (RadarConf18)*. Available at doi: https://doi.org/10.1109/RADAR.2018.8378544

Ivić, I. R., 2018a: Effects of Phase Coding on Doppler Spectra in PPAR Weather Radar. *IEEE Trans. Geosci. Remote Sensing*, *GE-56(4)*, 2043 – 2065. Available at: https://doi.org/10.1109/TGRS.2017.2772962

Ivić, I.R., 2018b: On the Use of Horn Antenna to Calibrate the MPAR Advanced Technology Demonstrator. *10th European Conference on Radar in Meteorology and Hydrology*, Wageningen, Netherlands. Available at: https://www.researchgate.net/publication/326258272_On_the_Use_of_Horn_Antenna_to_Calibrate_the_MPAR_Advanced_Technology_Demonstrator

Ivić, I. R., 2019: Facets of Planar Polarimetric Phased Array Radar Use for Weather Observations. AMS 99th Annual Meeting, Phoenix, AZ. Available at: https://ams.confex.com/ams/2019Annual/webprogram/Paper350901.html

Ivić, I. R., and D. Schvartzman 2019: A first look at the ATD data corrections. Preprints, *39th International Conference on Radar Meteorology*, Nara, Japan. Amer. Meteor. Soc., Paper 2-06. Available at: https://cscenter.co.jp/icrm2019/program/data/abstracts/Poster2-06_2.pdf

Ivić, I. R., and D. Schvartzman 2020: Weather Calibration Efforts on the Advanced Technology Demonstrator, *American Meteorological Society 100th Annual Meeting*, Boston, 2020, Paper 8B.4. Available at: https://ams.confex.com/ams/2020Annual/meetingapp.cgi/Paper/363084

Ivić, I. R., 2022: Quantification of Polarimetric PAR Effects on Weather Observables in the Phase Coded STSR Mode. *IEEE Trans. Geosci. Remote Sensing*, *60*. Available at: 10.1109/TGRS.2022.3146358

Ivić, I. R., 2023: Cross-Coupling Mitigation in Polarimetric PAR via Antenna Tilt, *Journal of Atmospheric and Oceanic Technology*, **40**, 587–604, https://doi.org/10.1175/JTECH-D-22-0059.1

T. Oguchi. (1983, Sep.). Electromagnetic wave propagation and scattering in rain and other hydrometeors, *Proc. IEEE*, *71(9)*, pp. 1029–1078.

Ryzhkov, A. V., and D. S. Zrnić, 2007: Depolarization in Ice Crystals and Its Effect on Radar Polarimetric Measurements. *J. Atmos. Oceanic Technol., 24(7)*, pp. 1256–1267. doi: http://dx.doi.org/10.1175/JTECH2034.1

Illingworth, A., and R. J. Thompson, 2011: Radar bright band correction using the linear depolarization ratio. *8th International Symposium on Weather Radar and Hydrology,* Apr. 18-21, 2011, Exeter, UK, p. 5. http://www.met.reading.ac.uk/radar/publications/LDR.pdf

Zrnić, D. S., J. F. Kimpel, D. E. Forsyth, A. Shapiro, G. Crain, R. Ferek, J. Heimmer, W. Benner, T. J. McNellis, and R. J. Vogt, 2007: Agile beam phased array radar for weather observations, *Bull. Amer. Meteorol. Soc.*, *88(11),* 1753-1766. Available at: https://doi.org/10.1175/BAMS-88-11-1753

Zrnić, D. S., V. M. Melnikov, and R. J. Doviak, 2012: Issues and challenges for polarimetric measurement of weather with an agile beam phased array radar. NOAA/NSSL Rep., 119 pp. Available at: http://www.nssl.noaa.gov/publications/mpar_reports/

Zrnić, D.S., R.J. Doviak, V.M. Melnikov, and I.R. Ivić, 2014: Signal Design to Suppress Coupling in the Polarimetric Phased Array Radar. *J. Atmos. Oceanic Technol., 31*, 1063–1077. Available at: https://doi.org/10.1175/JTECH-D-13-00037.1.

Weber, M. E., 2019: Meteorological Phased Array Radar Research at NOAA's National Severe Storms Laboratory. *2019 IEEE International Conference on Microwaves, Antennas, Communications and*

*Electronic systems (COMCAS)*. Tel Aviv, Israel. Available at: doi: [10.1109/COMCAS44984.2019.8958067](10.1109/COMCAS44984.2019.8958067)